Compensation of Atmospheric Phase Fluctuations in Radio Interferometry

Yoshiharu Asaki

Doctor of Philosophy

Department of Astronomical Science
School of Mathematical and Physical Science
The Graduate University for Advanced Studies

1996

Abstract

Compensation of interferometer phase fluctuations due mainly to the atmospheric water vapor is one of the most important subjects for future millimeter- and submillimeter-wave radio synthesis arrays and future millimeter-wave very long baseline arrays because the fluctuations are the most serious limiting factor for their spatial resolutions and sensitivities.

In the present thesis, a method for the atmospheric phase compensation called 'Paired Antennas Method (PAM)' is examined in detail. The PAM uses pairs of closely located antennas in order to simultaneously observe a target radio source and an adjacent reference calibrator with nearly parallel baselines and correct the interferometer phase of the target source using that of the reference source.

The effectiveness of the PAM was studied by means of interferometer phase compensation experiments using the Nobeyama Millimeter Array and the Nobeyama Radio Seeing Monitor at Nobeyama Radio Observatory of National Astronomical Observatory, Japan. In the experiments, a celestial radio source 3C 279 and a geostationary satellite (Japanese Communication Satellite called 'CS') were simultaneously observed and the angular-separation dependence of the effectiveness of the phase compensation was investigated.

It was always clearly seen in the experiments that the phase compensation with the PAM was very successful when the separation angle was smaller than a few degrees, even in the case that the millimeter-wave interferometer phase of the target source was compensated using the centimeter-wave phase of the reference source. The degree of phase compensation already achieved the level of less than 0.1 mm rms in excess path length, which is the goal of the planned new arrays for the future submillimeter-wave radio interferometry, when the atmospheric condition at Nobeyama was good enough. This demonstrates that the high resolution and high quality radio images are readily obtainable in the future large submillimeter-wave arrays at least if one uses the PAM or similar method of equivalent performance in order to eliminate the atmospheric phase fluctuations.

A model of the atmospheric structure was constructed to account for the experimental results on the basis of the Kolmogorov turbulence, frozen flow, and phase screen. A statistical calculation of the residual rms phase of the corrected phase in the PAM, based on the above atmospheric structure model, led to the numerical results in excellent agreement with a number of features of the experimental results. This implies that the underlying model, though simple, is a fairly good approximation of the reality. The computer simulations for the phase compensation in terms of the PAM at the potential sites of the future submillimeter-wave arrays revealed impressive results promising that the necessary

level of the phase compensation for the future arrays is achieved, provided that suitable reference sources are available within a few degrees around a target source.

The antenna-switching method is also a promising phase compensation technique similar to the PAM. Although the switching observation itself was not carried out in the phase compensation experiments with the Nobeyama Millimeter Array and Nobeyama Radio Seeing Monitor, I studied this method using the demonstrated data series produced from the PAM-experimental data and investigated the separation-angle dependence. Using the statistical model developed in the present thesis, the feasibility of the antenna-switching method was compared with that of the PAM and investigated in terms of the specific parameters such as the switching cycle time or the ON source time to a target source within one switching cycle. The computer simulations based on the model showed the potential of the antenna-switching method, which is equally effective in the phase compensation ability as the PAM if radio telescope antennas are able to slew fast enough. It was thus confirmed that the fast antenna-switching method is an effective way to realize the precise phase compensation with the simpler system than the PAM's. It is also noted that the PAM has an important merit in the long time integration to obtain the higher signal-to-noise ratio while observing weak radio sources.

Table of Contents

Chapter 1
Introduction 4

Chapter 2
Basic Concepts 14

Chapter 3
Phase Compensation Experiments with the PAM 22

Chapter 4
Estimation of Residual RMS Phase of Corrected
Fringe Phase with the PAM 54

Chapter 5
Phase Compensation with the Antenna-Switching Method 61

Chapter 6
Conclusions 81

1 Introduction

1.1 Radio Interferometry

Interferometer phase compensation, which is the main subject of the present thesis, is one of the most important subjects for present and future radio interferometry, especially for millimeter- or submillimeter-wave connected radio interferometry arrays and millimeter-wave Very Long Baseline Interferometry (VLBI). Here, we briefly overview the principles, basic systems, and scientific objectives of radio interferometry, in order to clarify the meanings of the further discussion.

1.1.1 Principles of Radio Interferometer Observations

A simple radio interferometer is basically composed of two radio telescope antennas receiving electromagnetic signals from celestial sources, and a correlator which measures the strength of the cross correlation and the phase difference between the simultaneously received signals at each antenna. The geometric vector spanning two antennas is referred to as the *baseline* or *antenna spacing* vector. The baseline length ranges from less than a meter to tens of killometers for connected-element interferometry, and from tens to thousands of killometers for VLBI. The observing electromagnetic wave is from decameter to submillimeter in wavelength, which ranges in frequency from tens of megahertz (MHz) to hundreds of gigahertz (GHz). The received signals with a finite frequency band are usually converted to intermediate frequency preserving the phase at the observing radio frequency for the convenience of the transmission and processing. Usually, the signals are transformed from the analog to the digital data before the cross correlation because the signal processing of the digital data is easier and more reliable than that of the analog data. The digitized signals are then cross-correlated by the correlator, which mainly consists of a multiplier and a time-averager. In the correlator, a time delay is inserted into the signal whose wave front has arrived faster than the other and the Doppler shift difference between the incoming signals due to the earth's rotation is corrected based on the a priori model. For connected-element radio interferometers, where the local oscillator signals for the frequency conversion of the received signals are distributed from a common frequency standard, the correlation is immediately carried out at the interferometry site. For VLBI, where each antenna site has an independent frequency standard for generating the local oscillator signals, the digitized signal at each antenna site is once recorded, with time codes, on magnetic tape, which is subsequently played-back for the correlation work. The configuration of a simple radio interferometer is shown in Figure 1.1.

The correlated data reveals a time series of a complex quantity called *fringe*, which is composed of amplitude and phase and includes information on source structures as well as various effects of the instruments and propagation medium. A complex quantity of the interferometer observables after calibration of the instrumental and environmental effects

is referred to as *complex visibility*, whose phase represents a time delay in arrival times of the same wave front at element antennas (hereafter, a time delay determined by the combination of a baseline and a source direction is referred to as the *geometric delay*) and the source structure. The phase also includes the 'cycle ambiguity', i.e., the offset that is a multiple of 2π. Source brightness distribution of a celestial object is obtained by inverse Fourier transformation of the complex visibility data obtained with a variety of baseline configuration which correspond to various spatial Fourier components of the brightness distribution [*Thompson, Moran, and Swenson*, 1986]. Modern radio interferometers have often been constructed in the form of the multi-element radio synthesis arrays to obtain a lot of spatial Fourier components simultaneously. The earth rotation is also very useful in the synthesis imaging, since the baselines projected onto a plane normal to the direction of the source vary in time as the earth rotates, thus providing new and new spatial Fourier components of the source distribution. One of the strong advantages of the radio interferometry is the high spatial resolution, which is expressed as λ/B in radian, where λ is observing wavelength and B is projected baseline length to the celestial sphere at the source. For example, if the observing wavelength is 2 mm and the projected baseline is 400 m, the resultant spatial resolution is 1 second of arc. In VLBI observations at $\lambda = 1.3$ cm and $B = 2000$ km, the spatial resolution reaches 1.3×10^{-3} arcsec or 1.3 milli-arcsecond (mas). On the other hand, the complex visibilities of relatively short baselines are also needed in order to investigate extended source structures and to obtain a wide dynamic range of the synthesis maps.

1.1.2 Scientific Studies with Radio Interferometry

Radio interferometry is one of the most powerful tools for astronomy to reveal detailed structure of celestial objects in high resolution. Radio interferometer arrays at centimeter or millimeter wavelength have brought to us impressive images of the fine structure of the molecular clouds, supernova remnants, and a vast variety of the normal and interacting galaxies. VLBI at centimeter or shorter wavelength with a baseline longer than a thousand kilometers has reached the resolution of a few mas or higher and has shown the superluminal jets in the active galactic nuclei and the great crowds of astronomical maser spots in the star forming regions and the circumstellar shells around the late type stars. On the other hand, VLBI measurements of the positions of strong celestial radio sources have yielded the accuracy well higher than one mas, and an aggregate of VLBI measurements have enabled to detect minute changes in Earth orientation in space and motions of the tectonic plates very precisely [*Dickey*, 1993; *Stein*, 1993].

Several new interferometer systems are proposed to take advantage of their high potential for astrophysics and astrometry. Millimeter- and submillimeter-wave radio observations with interferometry will be a frontier of astrophysics because there are various molecular emission lines which can be used as tracers of the high density gas regions with

high resolution.

For example, the luminous infrared galaxies in the local universe ($z < 0.1$) are expected to give us important information on the evolution of galaxies and quasars. In these galaxies, the dense molecular gas plays an essential role and the activity is strongly related to the amount of the dense gas condensed to the nuclei. Interferometer observations of the luminous infrared galaxies with millimeter or submillimeter molecular emission lines will be a unique way to investigate the spatial distribution, the physical environment, and the kinematics of the gas with the spatial resolution of 0.1 to 0.01 arcsec. It is very interesting in this respect that the protogalaxies are likely to be very bright at the submillimeter-wave. In fact, the strong infrared radiation emitted in the starburst activity, which is believed to be the origin of the energy of the luminous infrared galaxies, must be received in the submillimeter range due to the high red-shift of the galaxies. Therefore, we will be able to trace the process of the primordial massive star formation which must be an essential step in the early evolution of galaxies by virtue of the submillimeter-wave interferometry. The submillimeter-wave interferometry will be very useful also in the studies of the formation of stars and planets.

VLBI observations of the visibility phase measurements of the compact sources have potential ability of measuring the source position with the accuracy much higher than 1 mas. The relative visibility phase measurement of a pair of sources closely angular-separated in the celestial sphere yields the position accuracy of the order of 10^{-5} arcsec. Measuring positions of the galactic objects with respect to the closely separated extra-galactic sources with the accuracy of the above order, we can obtain the distances to the galactic sources by means of the annual trigonometric parallax without any physical assumption [*Sasao and Morimoto*, 1991]. In the Galaxy, there are a lot of objects such as the star forming regions or the evolved stars ejecting gas, which often radiate intense water and/or silicon monoxide maser emission [e.g., *Imai* et al, 1997]. The relative position measurement applied to these maser sources will enable us to estimate not only the distances but also the complete three-dimensional velocities of the objects. This will let us advance studies about the mass distribution and the kinematics of the Galaxy and then help us to understand the nature and the distribution of the dark matter probably governing the dynamics of the Galaxy.

1.1.3 Errors of the Observables in Radio Interferometry

The interferometer observable, the complex fringe, is subject to various errors which are traditionally classified into the amplitude errors and phase errors. The fringe amplitude errors are mainly caused by the absorption of the atmosphere and the gain fluctuations of the receivers. The errors are easily calibrated by observing nearby flux-density calibrators and skydip procedures or by hot/cold load calibrations.

On the other hand, the fringe phase errors which appear as the offsets and the fluctua-

tions are caused by the following reasons: a priori geometric delay model error, difference between the time delays in the propagation media along line of sight at each antenna, and the sum of instrumental phase errors at the two antennas, which includes thermal noise, cable delays, local oscillator phase, as well as instability of the independent frequency standards and time mis-synchronization in VLBI [*Thompson, Moran, and Swenson*, 1986; *Beasley and Conway*, 1995]. The geometric delay error is mainly caused by the uncertainties of the antenna positions, Earth rotation parameters, and the source positions. They cause the phase offset and the slow systematic drifts in the fringe phase and can be calibrated by using pre- and post-observations of calibrators with well-known positions.

The instrumental phase errors other than the thermal noise can also be corrected with the calibrator observations, since the instrumental phase variations occurring in well designed interferometric systems usually have time scales long enough to be effectively eliminated in those observations.

The tropospheric and ionospheric phase fluctuations are the most troublesome because they are randomly variable and much larger than the others. The phase fluctuations due to the ionosphere are inversely proportional to a square of the observing frequency and have large characteristic scale in space. Therefore, they do not seriously affect on the high frequency observations with connected-element interferometer arrays and can be well removed by dual frequency observations or direct measurements of Total Electron Content in VLBI. Note, however, that VLBI observations at single frequency less than a few GHz is often largely affected by the ionosphere.

The phase variations due to the dry air in the neutral atmosphere are well correlated with the surface pressure and can be compensated using the ground-based meteorological data [*Thompson, Moran, and Swenson*, 1986]. Thus the only problem left is the effect of the wet air, i.e., the water vapor component in the troposphere.

The water vapor in the troposphere is neither well mixed nor regularly distributed in the atmosphere and therefore is not well correlated with the ground-based meteorological parameters. Hence, the water vapor in the troposphere is highly unpredictable and causes fringe phase fluctuations with a time scale from less than a millisecond to several days. The magnitude of the effects, if not corrected at all, reaches from a few to several tens of centimeters in the excess path length [*Thompson, Moran, and Swenson*, 1986], which is too large compared with the requirement in the modern interferometry.

The phase fluctuations cause blurring of the synthesized images and wandering of the estimated source positions. Also the fluctuations make the sensitivity of the interferometric system lower due to the coherence loss. Consequently, the phase fluctuations give limits on the spatial resolution of the interferometer arrays (the limit, that is *radio seeing*, is of about $1'' - 2''$ in the millimeter arrays). It is well known that the radio seeing is worse in the millimeter- and submillimeter-wave than in the centimeter-wave because the seeing depends on the wavelength λ roughly as $\lambda^{(1-2/\alpha)}$ [*Thompson, Moran and Swenson*, 1986],

where α is an exponent in the excess path *structure function* ($D(\rho) \propto \rho^{\alpha}$ with ρ, being a spatial interval; see §2.1.3) and is always less than 2. Even if we go to the top of Mauna Kea, one of the best observing sites in the world, the radio seeing at submillimeter-wave is about 1″ in median [*Masson*, 1994].

The excess path delay due to the water vapor is almost constant from decameter to submillimeter wavelength range. Since this implies that the phase fluctuations are proportional to the observing frequency, the degrading effects are the more severe the higher the observing frequency is. Therefore, it is utterly unavoidable to develop a suitable way to compensate the phase fluctuations due to the water vapor component for successful realization of the future radio interferometry.

1.1.4 Interferometer Phase Compensation Technuques

For taking advantage of phase information of the fringe to obtain the synthesis maps (brightness maps), closure relation has been widely used in VLBI because direct calibration of the fluctuation in fringe phases is impractical or difficult [*Rogers* et al., 1974]. So-called closure phase is the sum of fringe phases of at least three baselines forming a closed polygon. The closure phase is free from the antenna based phase errors including the atmospheric phase fluctuations and instrumental phase drifts. However, this method inevitably leads to the information-loss because the number of obtained closure relations is less than that of attainable fringes. In particular, the closure phase is useless for the astrometric purposes, since there is no information on the absolute source position is left in the closure phase. Therefore, it is more advantageous to use the fringe phase itself.

Several kinds of techniques have been proposed for effective correction of the tropospheric phase fluctuations. For example, various astrometric observations in VLBI field have undergone with the conventional antenna-switching differential VLBI method [*Shapiro* et al., 1979; *Bartel* et al., 1986; *Gwinn* et al., 1986; *Lestrade* et al., 1990; *Treuhaft and Lowe*, 1991; *Beasley and Conway*, 1995; *Guirado* et al., 1995; *Lara* et al., 1996]. These results have yielded the position accuracy of the order of 10^{-4} arcsec. For future millimeter-wave radio arrays, *Holdaway and Owen* [1995] have proposed switching observations between a target and an adjacent reference calibrator with the fast slew speed using newly designed antennas. The phase compensation techniques where the calibrator sources are used as the phase reference are referred to as *phase-referencing*.

The "Paired Antennas Method" which I will examine in detail in the present thesis is a kind of the phase-referencing technique and uses pairs of closely located antennas in order to simultaneously observe a target source and an adjacent reference calibrator with nearly parallel baselines and correct fringe phase of the target source using that of the reference source. This technique has been proposed in the field of VLBI [*Counselman* et al., 1976] and probed its power for measuring relative positions between closely spaced radio sources, since the effects of the ionosphere and the troposphere as well as the fluctuations in the

frequency standards are largely cancelled in the difference of the fringe phases of the target and reference sources. The phase-referencing technique has been especially successful when the target and reference sources are so close that both of them are observed in the same beam of each element antenna. In such very fortuitous cases, the formal errors of the relative position measurements were as low as several micro-arcsec [e.g., *Marcaide and Shapiro*, 1983; *Marcaide and Shapiro*, 1984; *Marcaide* et al., 1985; *Marcaide, Elósegui, and Shapiro*, 1994].

Another method called radiometric phase correction method attempts to measure the intensity of the thermal line emission of the atmospheric water vapor in the direction of the target source to estimate the excess path delay. This technique has been examined rather intensively in geodetic VLBI observations, but the achievements have not been very impressive. *Linfield* et al. [1996] reported encouraging results from recent experiments which used water vapor radiometers with two frequency channels (20.7 and 31.4 GHz). However, they could succeed in improving the accuracy of the group delay measurements by 16 % only because uncalibrated instrumental effects in the VLBI delay variations were larger than the atmospheric effects, which could not completely prove the validity of the radiometric method. This work achieved the compensation to the rms level of 2–3 mm in excess path length. The improvement of the precision was limited by the stability of the receivers of the radiometers and is not fully enough for the future VLBI.

Much higher level of the phase compensation is challenged in recent radiometric phase correction experiments which attempt to develop a realistic phase compensation technology for the future millimeter- and submillimeter-wave arrays. They use the water vapor emission in 220 GHz and try to measure the brightness temperature of the emission with the accuracy of 0.25 K or higher to predict the variation of the excess path length at 0.1 mm level. Beautiful correlations have been reported between the measured brightness temperature difference and the fringe phase obtained in the actual interferometer array observations under clear sky conditions [*Welch*, 1994; *Bremer* et al., 1995; *Bremer*, 1995]. The radiometric phase correction method suffers from a difficulty when the atmosphere contains water droplets (clouds) along with the water vapor. The water droplets cause substantial absorption thus strongly affecting the brightness temperature but small change in the index of refraction and hence in the excess path delay. The attempt to eliminate the cloud effect by combining measurements at two frequencies has not been very successful so far. The phase compensation methods introduced here are illustrated in Figure 1.2.

The phase-referencing may have difficulty when applied to the observations at wavelength shorter than a few millimeters because the flux density of the quasars, the candidate reference sources, generally decreases with increasing frequency. If we cannot find a suitable reference source within a few degrees from a target source, the effectiveness of the phase compensation is lowered.

A promising solution to this problem is to observe the calibrators at lower, for example centimeter, wavelength where many bright compact sources are available. The refractivity of water vapor is dominated by contributions from strong lines in the far infrared part of the spectrum. The refractivity is therefore almost constant (non-dispersive) from decameter to submillimeter wavelengths. Hence, it is very interesting to examine whether the effective phase correction can be performed using different frequencies for the target and reference source.

In the present thesis, I studied the Paired Antennas Method (PAM) in detail analyzing the data obtained in the series of phase compensation experiments carried out at Nobeyama Radio Observatory (NRO) of National Astronomical Observatory, Japan, using the Nobeyama Millimeter Array (NMA) and the Nobeyama Radio Seeing Monitor (NRSM). The observatory is at Nobeyama Heights, Japan, where has the good radio seeing and is suitable for the observations at millimeter wavelength in the winter.

In the phase compensation experiments at NRO, a strong quasar 3C 279 as a target source and a geostationary satellite, Japanese Communication Satellite (CS), as a reference source were simultaneously observed. The primary purposes of the experiments were to confirm the effectiveness of the phase compensation, to investigate the angular-separation dependence of the compensation performance, and to examine the applicability of the compensation of the millimeter-wave interferometer phase using the reference phase of longer wavelengths. The experiments were mainly composed of two observation series. The first series was conducted on October 5, 1994, under bad weather condition, using the NMA solely constructing only 520-m baseline. The second series was conducted on 28 and 29 January, 1995, under very good weather condition, using the NMA and the NRSM simultaneously, with which multi baselines ranging 60–300 m were available.

It can be expected that several interesting points in the phase-referencing will be appeared through analyses of the results obtained in the experiments. First, the angular-separation dependence of the degree of phase compensation in the PAM will directly be clarified. In the analysis we can estimate a critical separation angle beyond which the PAM does not effectively works in each observation series. Second, effective baseline length beyond which the PAM is needed can be investigated using the multi-baseline data in the second observation series. Third, since the weather conditions were so different between the observation series, we can quantitatively investigate the relation between the degree of phase compensation and the weather condition, that is, the radio seeing. Forth, it is possible to demonstrate the phase compensation at millimeter-wave using the centimeter-wave phase in the phase-referencing technique, since we observed 3C 279 at 2-mm wave while observing CS at 1.5-cm wave in the second observation series.

Understanding the experimental results, I will construct a statistical model for numerical calculation of the residual atmospheric effects in the compensated interferometer phase in the phase-referencing. The validity of this model can be easily demonstrated by

the the computer simulations of the results obtained in the phase compensation experiments. Using the simulations, we can discuss the feasibility of the PAM with which future radio arrays will be built at the potential sights.

Although the phase compensation experiments adopting the antenna-switching method have not been carried out in the present thesis, it is possible to study this method using the demonstrated data series produced from the present data. We can also compare the feasibility of the antenna-switching method with that of the PAM using the statistical model developed in the present thesis. It is important in the antenna-switching method to consider specific observing parameters such as the switching cycle time or the ON source time because they may have serious influences on the residual phase errors in the observations. We can discuss the parameters in terms of the residual atmospheric effects by means of the simulations based on the statistical model. This comparing discussion is very important to determine which technique will be adopted for a science goal or array configurations.

The basic ideas of the phase compensation in terms of the PAM are described in Chapter 2. The setups of the experiments and performance parameters of the radio telescopes are explained, and the results of the experiments are shown in Chapter 3. In Chapter 4, the results are analyzed and compared with the predictions derived from the atmospheric structure model. A statistical model is then developed for estimating the residual rms phase errors due to the atmosphere for the PAM. In Chapter 5, the antenna-switching phase compensation technique other than the PAM is discussed on the basis of the results obtained in the above experiments and the problems to be solved for further development of the phase compensation technology are clarified. The conclusions are summarized in Chapter 6.

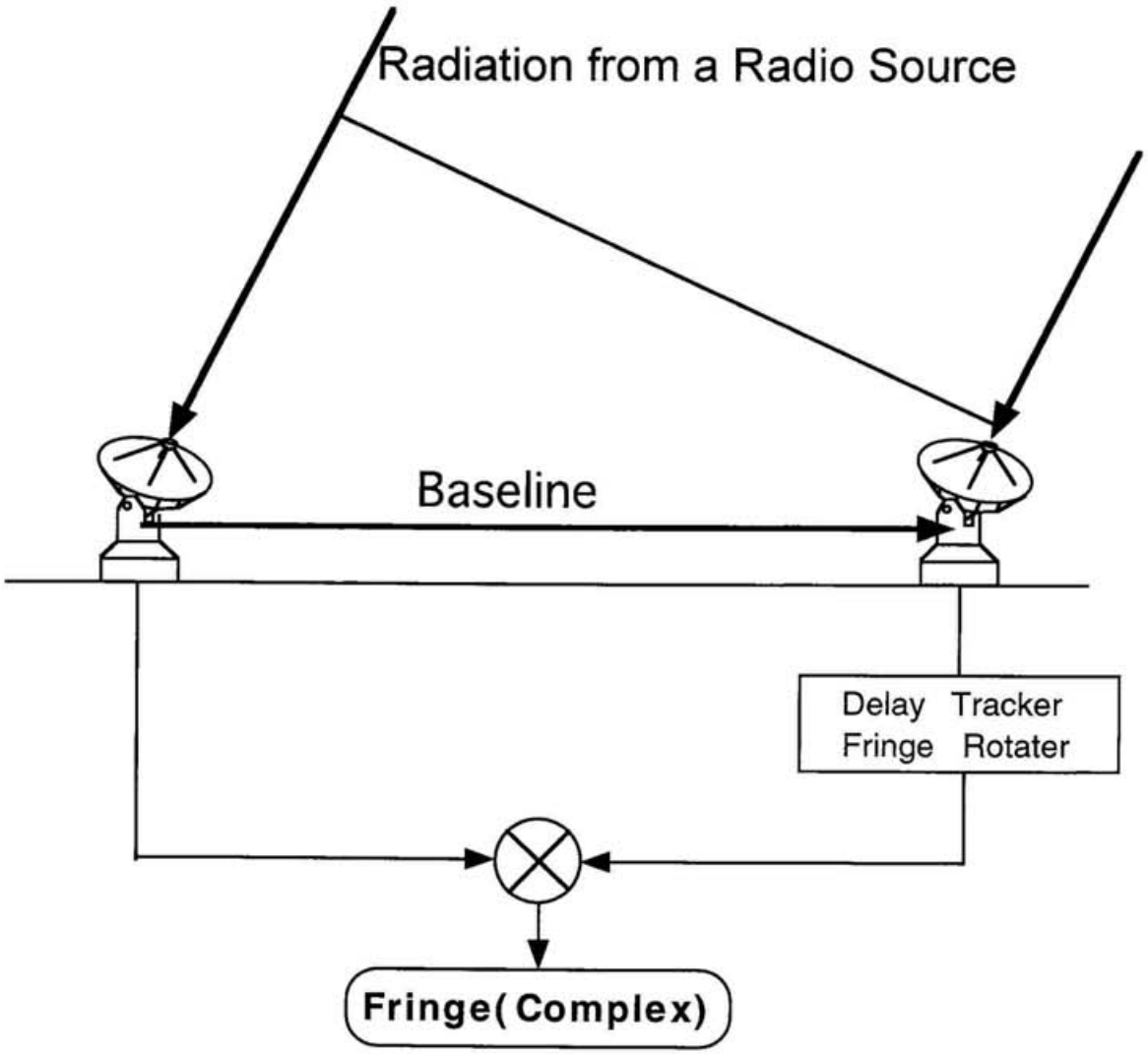

Figure 1.1: Basic configuration of a simple radio interferometer.

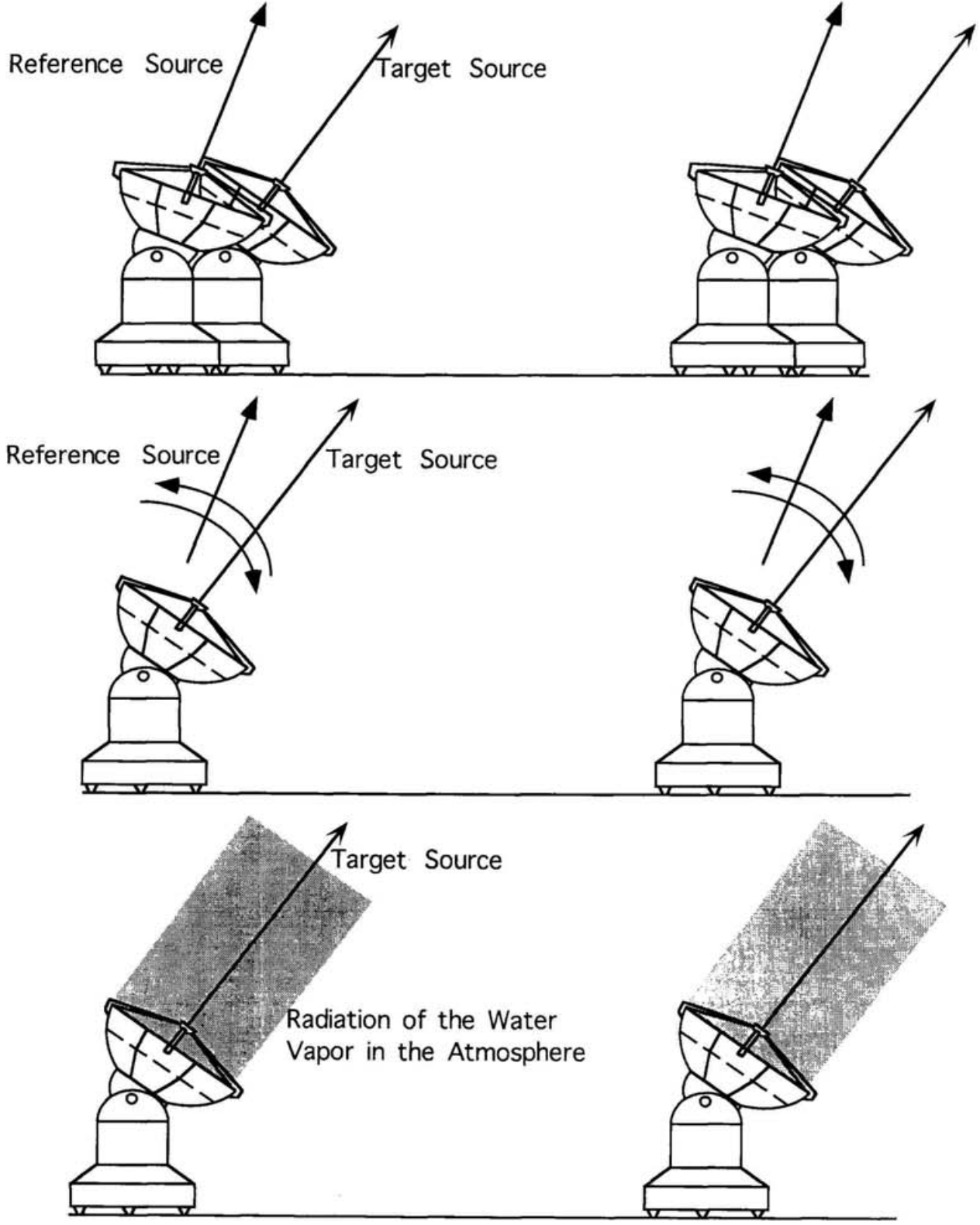

Figure 1.2: Phase compensation techniques of radio interferometry of the paired antennas method (top), the antenna-switching method (middle), and the radiometric phase correction method (bottom).

2 Basic Concepts

2.1 Tropospheric Phase Fluctuations

2.1.1 Excess Path Length in the Troposphere

Excess path delay τ_{air} for radio wave to traverse along r through the atmosphere filled by a uniform diellectric medium with a refractive index n is given by

$$\tau_{air} = \frac{1}{c}\int (n-1)dr = \frac{1}{c}10^{-6}\int N(r)dr, \tag{1}$$

where N is the refractivity defined by $N = 10^6(n-1)$. The refractivity of moist air in the radio range is given by the empirical formula

$$N = 0.2228\rho_T + 1763\frac{\rho_D}{T} = N_D + N_V, \tag{2}$$

where T is the temperature in Kelvins, ρ_T and ρ_D are the densities of the sum of all constituents and the water vapor in the atmosphere, respectively, in gm^{-3}, and N_D and N_V are the refractivities of the dry air and the water vapor, respectively [*Thompson, Moran and Swenson*, 1986]. The excess path delay due to the water vapor of plane wave from a celestial source through the atmosphere is obtained by integrating N_V along line of sight

$$\tau_{air} = \frac{1}{c}10^{-6}\int_0^\infty N_V(r)dr. \tag{3}$$

In the very wet case with $T = 303$K and relative humidity of 80 %, the excess path length is as large as 28 cm. The water vapor density ρ_V roughly varies exponentially with a scale height of $\sim$2 km.

2.1.2 Assumptions on the Atmospheric Structure

Many astronomers have studied the phase fluctuations of the radiation due to the atmosphere. In the course of these studies, it has been recognized that the spatial frequency spectrum of the index of refraction of the atmosphere is more or less well approximated by Kolmogorov turbulence theory. The concepts of the *phase screen* and the *frozen flow* have also been accepted as useful means to approximate the temporal and spatial variations of the refractivity index. The phase screen hypothesis assumes that the turbulent water vapor component is confined within an infinitely thin horizontal layer roughly at the scale height h above the surface of the Earth. The frozen flow assumes that the spatial

patterns of the fluctuations are moved horizontally by the wind of constant velocity v. It was *Tatarski* [1961] who placed mathematical foundations for the statistical theory of the atmospheric structure model based on the above hypotheses. The theory was further developed and applied to the various observable quantities of the radio interferometry by *Dravskikh and Finkelstein* [1979] and *Treuhaft and Lanyi* [1987]. The turbulent structure of the tropospheric phase fluctuations has been confirmed in a number of experiments using radio interferometer arrays [e.g., *Armstrong and Sramek*, 1982].

We adopt hypotheses of the Kolmogorov turbulence, frozen flow, and phase screen in addition to Tatarski's theoretical formulation as the basis for our mathematical developments of the statistical model of the turbulent atmosphere in the interpretation of the results of the phase compensation experiments.

2.1.3 Structure Function of Excess Path Fluctuation

The structure function [*Tatarskii*, 1961] is a quantity which is useful for describing the universal characteristics of the tropospheric fluctuations. Here, we introduce a spatial structure function (SSF) of the excess path fluctuations in the phase of an incident radio wave due to the troposphere. The SSF $D(\rho)$ is defined as the mean square difference in the phase fluctuations at two sites separated by a displacement vector $\boldsymbol{\rho}$:

$$D(\rho) = 4\pi^2\nu^2\langle\{\tau_{air}(\boldsymbol{r}+\boldsymbol{\rho}) - \tau_{air}(\boldsymbol{r})\}^2\rangle, \tag{4}$$

where angle brackets mean an ensemble average, τ_{air} is the excess path delay due to the water vapor, ν is the observing radio frequency, and $\boldsymbol{r}$ is a position vector. Following Tatarskii, we assume here that the fluctuation field is homogeneous and isotropic so that the structure function D depends only on $\rho = \mid \boldsymbol{\rho} \mid$.

According to Kolmogorov theory of isotropic turbulence, the excess path SSF is well approximated by a simple power law:

$$D(\rho) = \left(\frac{2\pi}{\lambda}\right)^2 C_l^2 \rho^{\alpha}, \tag{5}$$

where C_l is the structure coefficient and λ is wavelength. Kolmogorov theory predicts that the structure exponent α tends to $5/3$ when ρ is smaller than the scale height h, whereas it tends to $2/3$ when ρ is much larger than h [*Dravskikh and Finkelstein*, 1979; *Treuhaft and Lanyi*, 1987].

According to the frozen-flow hypothesis, a temporal structure function (TSF) $\bar{D}(T)$ for a time interval T at a single site is equivalent to the SSF $D(\rho)$ between two sites

separated by a distance $\rho = vT$:

$$\bar{D}(T) = D(\rho) \mid_{\rho=vT} . \tag{6}$$

2.1.4 Estimation of the Spatial Structure Function

If the thermal noise contribution is well subtracted from the fringe phase data for a basic radio interferometer with two antennas as illustrated in Figure 2.1, the estimated dispersion must closely approximate the SSF $D(B)$, as expected from the ergodicity, on the following ground.

The dispersion σ_f^2 of a stationary random function of time $f(t)$ over an integration time T is always described in terms of the TSF $\bar{D}_f(\tau) = \langle \{f(t+\tau) - f(t)\}^2 \rangle$ [*Treuhaft and Lanyi*, 1987]:

$$\sigma_f^2 = \left\langle \frac{1}{T} \int_0^T \left\{ f(t) - \frac{1}{T} \int_0^T f(t')dt' \right\}^2 dt \right\rangle = \frac{1}{T^2} \int_0^T (T-t)\bar{D}_f(t)dt, \tag{7}$$

Therefore, we can estimate σ_Φ^2 in terms of the SSF $D_\Phi(B, \rho)$ of the fluctuations in the fringe phase for the baseline of length B due to the troposphere. According to the simple statistical model introduced above, $D_\Phi(B, \rho)$ can be expressed through the SSF $D(\rho)$ of the excess path phase fluctuation. In fact,

$$\begin{aligned} D_\Phi(B,\rho) &= \langle 4\pi^2\nu^2 \{\tau_{air}(\boldsymbol{r}+\boldsymbol{B}+\boldsymbol{\rho}) - \tau_{air}(\boldsymbol{r}+\boldsymbol{\rho}) - \tau_{air}(\boldsymbol{r}+\boldsymbol{B}) + \tau_{air}(\boldsymbol{r})\}^2 \rangle \\ &= 4C(0) - 4C(B) - 4C(\rho) + 2C(\mid \boldsymbol{\rho}+\boldsymbol{B} \mid) + 2C(\mid \boldsymbol{\rho}-\boldsymbol{B} \mid), \end{aligned} \tag{8}$$

where $C(R) = 4\pi^2\nu^2 \langle \tau_{air}(\boldsymbol{r}+\boldsymbol{R})\tau_{air}(\boldsymbol{r}) \rangle$ is the autocorrelation function. Then, equation (8) is reduced to

$$D_\Phi(B,\rho) = 2D(\rho) - D(\mid \boldsymbol{\rho}+\boldsymbol{B} \mid) - D(\mid \boldsymbol{\rho}-\boldsymbol{B} \mid) + 2D(B), \tag{9}$$

because of the well-known relation $D(R) = 2C(0) - 2C(R)$. A similar equation is derived by *Dravskikh and Finkelstein* [1979]. Therefore, the corresponding TSF is equal to

$$\bar{D}_\Phi(B,t) = 2D(vt) - D(\mid \boldsymbol{vt}+\boldsymbol{B} \mid) - D(\mid \boldsymbol{vt}-\boldsymbol{B} \mid) + 2D(B). \tag{10}$$

Substituting this equation into equation (7), we see that first three terms in the right-hand side of equation (10) give only negligible contribution to the integral, provided that $T \gg B/v$ and $\alpha < 2$, where α is the exponent of the excess path SSF. Thus we obtain

$$\sigma_\Phi^2 = \frac{1}{T^2}\int_0^T (T-t)\bar{D}_\Phi(B,t)dt \cong D(B), \tag{11}$$

for large T. This relation is very helpful for the estimation of the SSF.

2.2 Fringe Phase Difference in PAM Observations

Consider fringe phases Φ_A and Φ_B obtained at two nearly parallel baselines one connecting antennas 1 and 2 observing a source A and another connecting antennas 3 and 4 observing another source B, respectively, as illustrated in Figure 2.2. Each fringe phase can be described as follows [*Thompson, Moran, and Swenson*, 1986]:

$$\Phi_A = 2\pi\nu_A(\tau_{gA} + \tau_{air\{12\}}) + \Delta\theta_{\{12\}} \tag{12}$$

$$\Phi_B = 2\pi\nu_B(\tau_{gB} + \tau_{air\{34\}}) + \Delta\theta_{\{34\}}, \tag{13}$$

where ν_A and ν_B are the sky frequencies at the band center, τ_g is the geometric delay including the source structure effect, and $\tau_{air\{nm\}}$ is the randomly varying difference in the tropospheric excess path delay between antennas n and m. $\Delta\theta$ is the difference in the instrumental phase, which can be easily eliminated by observing bright calibrator sources with well-known celestial positions because of its relatively slow time variation. The fringe phase Φ' after subtracting the a priori geometric delay and calibrating the instrumental phase is reduced to

$$\Phi'_A = 2\pi\nu_A(\Delta\tau_{gA} + \tau_{air\{12\}}) \tag{14}$$

$$\Phi'_B = 2\pi\nu_B(\Delta\tau_{gB} + \tau_{air\{34\}}), \tag{15}$$

where $\Delta\tau_g$ is the residual geometric delay which varies slowly.

If $\nu_A \neq \nu_B$, direct comparison between Φ'_A and Φ'_B is impossible. The phase of source B at the frequency ν_B must be converted to the phase at the frequency ν_A in terms of a suitable scaling factor. If we assume that the refractivity of the water vapor is non-dispersive, the scaling factor is simply equal to the frequency ratio ν_A/ν_B and we obtain

the 'frequency–converted' phase of source B:

$$\Phi''_B = \Phi'_B \times \frac{\nu_A}{\nu_B} = 2\pi\nu_A(\Delta\tau_{gB} + \tau_{air\{34\}}). \tag{16}$$

Then, the difference in the fringe phase $\Delta\Phi = \Phi'_A - \Phi''_B$ is expressed by

$$\Delta\Phi = 2\pi\nu_A\{(\Delta\tau_{gA} - \Delta\tau_{gB}) + (\tau_{air\{12\}} - \tau_{air\{34\}})\}. \tag{17}$$

If the water vapor refractivity is indeed almost non-dispersive and if we simultaneously observe a very close pair of sources with closely located antennas, the tropospheric phase fluctuations included in Φ'_A and Φ''_B must be almost the same and should simply disappear in the phase difference. Therefore, we have the phase difference

$$\Delta\Phi' \simeq 2\pi\nu_A(\Delta\tau_{gA} - \Delta\tau_{gB}), \tag{18}$$

which can be used as an observable for extracting the scientifically meaningful information on the radio sources.

Let me introduce a new quantity which we call "coherence factor" [*Asaki* et al., 1996]. The factor is useful for discussing the coherence of the corrected fringe phase with the PAM. This factor η_c for two time series of the fringe phase Φ_A and Φ_B with a time lag τ is defined as follows:

$$\eta_c = \left| \frac{1}{T} \int_0^T exp\{j[\Phi_A(t) - \Phi_B(t+\tau)]\} dt \right|. \tag{19}$$

Where $\tau = 0$ corresponds to the case when the coherence factor is calculated between two time series which are completely time-synchronized. This quantity shows the sign of the coherence of the corrected fringe phase.

2.3 Goal of the Phase Compensation Techniques for Millimeter- and Submillimeter-wave Radio Arrays

It is a widely acceptable idea that amplitude of fluctuations in the fringe phase will not be expected of over 1 rad rms in order to obtain the good synthesis maps or to measure the source positions precisely by means of the long time integration without the serious coherence loss [*Thompson, Moran, and Swenson*, 1986]. According to this idea,

the phase fluctuations due to the tropospheric water vapor must be calibrated under the rms level of 1 rad, which requires the different compensation steps to achieve for different observing wavelengths or frequencies: the required degree of compensation is estimated by $\lambda/2\pi = 0.159\lambda$ in excess path length where λ is the observing wavelength. For example, the required degree of compensation is 1.1, 0.12, and 0.09 mm in excess path length for observing frequency of 43, 230, and 490 GHz, respectively. Some of future radio arrays are planned to install 820-GHz receiver systems, which will require the path-length compensation level of 0.06 mm rms at the potential sites with the best radio seeing in the world. Hence, a goal of the phase compensation techniques is set to the path-length compensation level of 0.06 mm rms under the good atmospheric conditions, in which the radio seeing for 100-m baseline at such sites is expected of 0.1 mm rms or smaller [*Masson*, 1994].

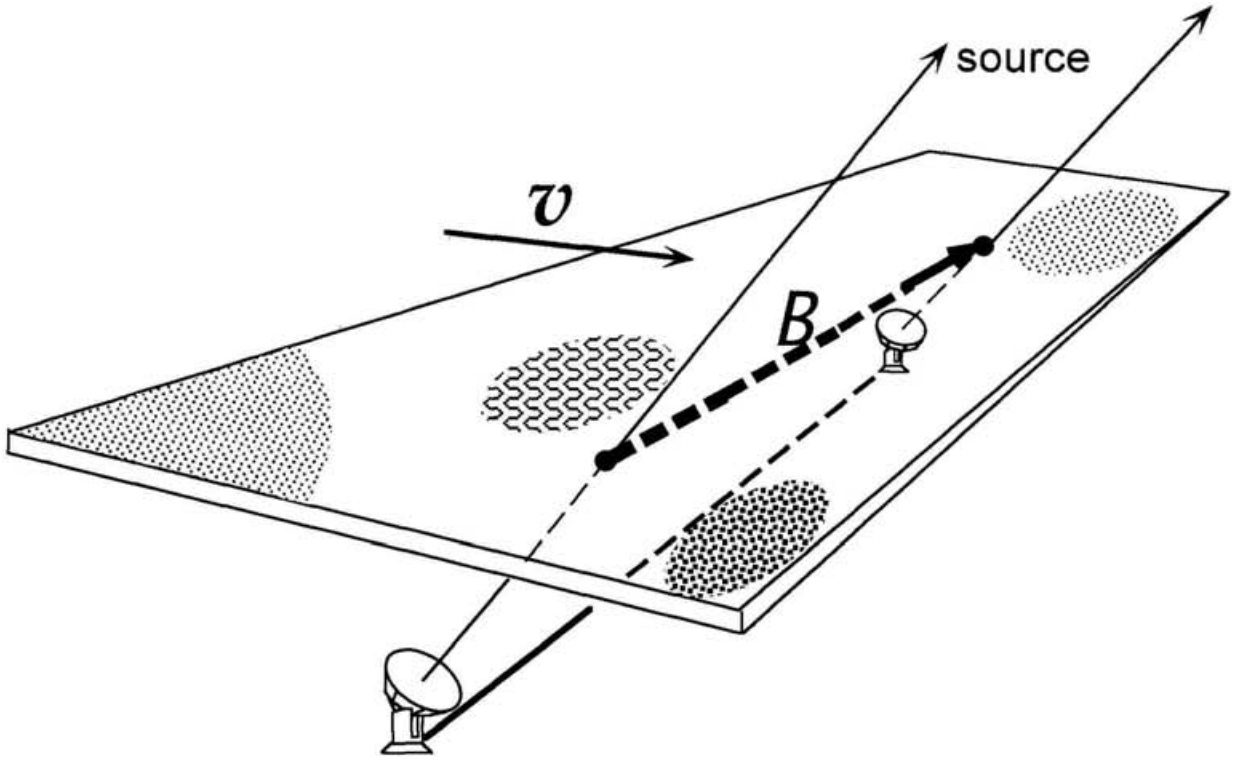

Figure 2.1: Configuration of a basic radio interferometer with two antennas.

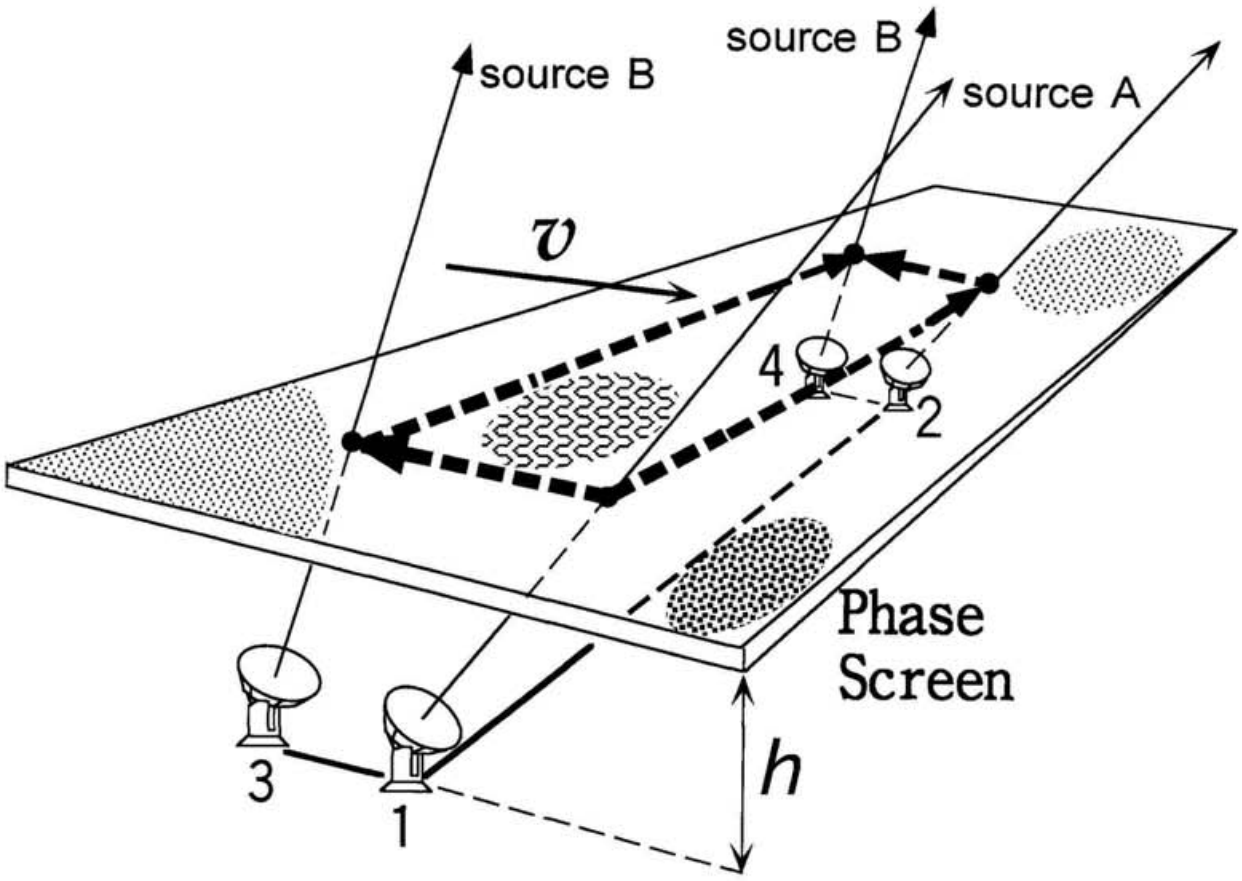

Figure 2.2: Configuration of the paired antennas method (PAM) observations.

3 Phase Compensation Experiments with the PAM

3.1 Overviews of the Experiments

The phase compensation experiments with the PAM were carried out using the Nobeyama Millimeter Array (NMA) [*Morita*, 1994] and the Nobeyama Radio Seeing Monitor (NRSM) [*Ishiguro*, 1990] at Nobeyama Radio Observatory (NRO) of National Astronomical Observatory, Japan. The experiments were mainly composed of two observation series, the first series was conducted on October 5, 1994 using the NMA solely while the second series was conducted on 28 and 29 January, 1995 using the NMA and the NRSM simultaneously. Hereafter, we refer to the experiments as "PAM1" and "PAM2" for the first and second series, respectively.

The NMA is composed of six parabolic reflectors with 10-m diameter and is used for imaging celestial radio sources at millimeter wavelength. All of the antennas are movable between the stations in steps to form the required antenna spacings. In the both of the series of the experiments, the frequency-converted and digitized intermediate frequency signals of the NMA were cross-correlated by the fast Fourier transform spectrocorrelator [*Chikada et al.*, 1987] with the bandwidth of 320 MHz. Frequency channels of 824 out of an available 1024 were used to avoid the band-edge effect. The complex cross-correlation data were averaged for 2 s and 10 s for PAM1 and PAM2, respectively, by the correlator and stored in the NMA database.

The NRSM, which is usually used for monitoring the radio seeing at NRO, consists of five commercially available offset-gregorian reflectors with 1.8-m effective diameter. The NRSM antennas are oriented towards the fixed direction of the sky where the geostationary satellite (Japanese Communication Satellite called 'CS') resides and emits the strong carrier signal at frequency of 19.45 GHz. The received 19.45 GHz signals at each NRSM antenna are amplified and down-converted to 278 MHz. The converted signals are passed through the NMA coaxial cables via underground tunnel to the NMA array operation building.

CS is a geostationary satellite located at 184.2° in azimuth and 48.3° in elevation at NRO. Quasar 3C 279 passes by the CS position with the minimum separation angle between 3C 279 and CS less than 0.1° as shown in Figure 3.1. The time variations of the separation angle are shown in Figure 3.2. The positions of the observed sources are listed in Table 3.1. In the following data analyses, we refer to 3C 279 and CS as the target and reference source, respectively. The time when the separation angle was minimum is referred to as reference time.

3.2 PAM1

3.2.1 Observations

The basic configuration of the PAM1 experiments is illustrated in Figure 3.3. The four antennas were divided into two pairs along an east-west baseline with a length of roughly 520 m. The separation between antennas 1 and 3 was about 53 m, while the separation between antennas 2 and 4 was about 26 m. The antenna code and the system noise temperature are listed for each antenna in Table 3.2. Since we observed the quasar 3C 279 together with CS, we used receivers sensitive to the carrier frequency 19.45 GHz of CS. The complex cross-correlation data were averaged for 2 s by the correlator.

A special observation where all the four antennas observed a strong quasar 3C 454.3 was carried out at nighttime just after the simultaneous 3C 279–CS observation in order to obtain statistical characteristics of the tropospheric phase fluctuation at NRO. The correlated flux densities of 3C 279 and 3C 454.3 were not measured at the PAM1 experiments. Instead, we assumed the flux density as 11×10^{-26} $\mathrm{Wm^{-2}Hz^{-1}}$ for 3C 279 and 18×10^{-26} $\mathrm{Wm^{-2}Hz^{-1}}$ for 3C 454.3 at 19 GHz based on the Very Large Array flux calibrator catalog. In analyzing the rms fluctuation of the fringe phase, the thermal noise contribution mainly caused by the receivers and in the transmission cables must be removed before estimating the atmospheric effects. The atmospheric rms phase σ_{atm} is calculated by eliminating the thermal rms phase σ_{therm} from the measured rms phase σ_m as follows

$$\sigma_{atm} = \sqrt{\sigma_m^2 - \sigma_{therm}^2}. \tag{20}$$

3.2.2 Pre-processing in PAM1

In order to avoid possible spurious effects, we performed the following two steps to produce the secondary data.

1. There were several artificial spikes in the phase of the raw data due to the general purpose interface bus (GP-IB) control error of the NMA fringe rotator. The data points containing the large phase spikes were replaced by the interpolated ones.
2. While the PAM1 experiments had lasted until 16:00 JST, we used the data to 15:00 JST because it was difficult to remove perfectly the 2π spurious phase noises due to larger fluctuations in both of the fringe phase data in the last one hour. The obtained fringe phase of 3C 279 and CS showed slow drift due to the baseline errors or the source position errors. Therefore, we fitted the data to a second-order polynomial for a time interval of a few hours and removed the trend from the data.

The pre-processed time series are further averaged for an accumulation time of 10 s. The rms phase is calculated from the averaged data. The contribution of the thermal noise is estimated and subtracted from the rms phase of 3C 279. The estimated thermal noise is 7.9° for the accumulation time of 10 s under the assumptions that the correlated flux density is 11×10^{-26} $Wm^{-2}Hz^{-1}$, aperture efficiency of each NMA antenna is 0.65 at 19–20 GHz, and an efficiency factor for the quantized correlation process is 1. The signal of CS is so strong that the thermal phase noise (less than 0.1° in rms) is negligible.

3.2.3 The Standard Deviation of the Differential Fringe Phase

The fringe phase difference between 3C 279 and CS (phase of 3C 279 corrected by that of CS) was obtained by subtracting the CS phase from the 3C 279 phase. The fringe phase difference is shown in Figure 3.4 along with the 3C 279 phase and the CS phase with the accumulation time of 10 s. Significant decrease of the fluctuation in fringe phase difference is evident as the separation angle between the radio emitters approaches to the minimum value.

The standard deviation of the phase difference estimated for 500-s time interval is shown in Figure 3.5. The standard deviation is about 10° at the minimum separation angle and gradually increases with increasing separation angle. The standard deviation becomes almost saturated at the 50°–70° level around 13:20 JST with the separation angle of 20° as shown in the figure. This is a critical separation angle for effective compensation of the tropospheric phase fluctuation in the PAM1 experiments.

The critical separation angle is easily explained in terms of the principles of the PAM. There are two kinds of filtering mechanisms operating to the large scale tropospheric irregularities in the PAM. One is the filtering inherent in every connected interferometer, i.e., the filtering of irregularities with sizes larger than the baseline length. Another is the filtering of irregularities with sizes larger than the horizontal scale at the scale height of the troposphere corresponding to the separation angle between the radio sources [*Dravskikh and Finkelstein*, 1979]. The second mechanism is dominating as long as the horizontal scale is smaller than the baseline length. If the source separation is large enough that the horizontal scale exceeds the baseline length, the first mechanism becomes dominant, which is almost independent of the separation angle. Assuming the tropospheric scale height to be 1000 m [*Treuhaft and Lanyi*, 1987], we see that the horizontal scale corresponding to the critical separation angle of 20° at the direction of CS with 48.27° elevation is about 500 m, which is roughly equal to the length of our east-west baseline.

3.2.4 The Coherence Factor of the Differential Fringe Phase

The coherence factor η_c introduced in equation (19) in Chapter 2 was estimated. Figure 3.6 shows η_c obtained from the 3C 279–CS observation with the integration interval $T = 1000$ s and the lag $\tau = 0$ s. In this case, we use the raw 2-s values of the correlated

data in order to see the detailed correlation of the two time series. The result again shows the critical separation angle around 20°. In addition, the figure implies that a phase-referencing long-time integration of the correlator output for a separation angle above 15° will suffer from serious coherence loss in millimeter-wave interferometry.

Figure 3.7 shows the lag τ which maximizes η_c as a function of time. The lag increases almost monotonically until 13:20 JST when the separation angle reaches 20°. This is well explained on the basis of the frozen-flow hypothesis which assumes that the temporal fluctuation is caused by the spatial pattern of the moist air blocks moved over the site by the wind. According to the hypothesis, the same temporal phase variation once observed at the direction of 3C 279 must be repeated at the direction of CS after an interval of time traveled by the wind between the source directions. Therefore, η_c takes its maximum when the time lag τ is equal to the above time interval. From Figure 3.6, we see that the rate of increase of lag τ with angular separation is about 3.3 s/deg. If we assume again the tropospheric scale height of 1000 m, the rate roughly corresponds to the east-west component of the wind velocity $\simeq$ 9 m/s at the direction of CS. Since the western wind is the dominating one in the upper troposphere, the value is in reasonable agreement with those adopted by *Treuhaft and Lanyi* [1987] and *Dravskikh and Finkelstein* [1979] (8 m/s and 10 m/s, respectively).

3.2.5 The Spatial Structure Function Measurements at PAM1

In order to estimate the structure coefficient and the exponent of the SSF at NRO, we observed the strong quasar 3C 454.3 for several hours with all the four antennas just after the 3C279–CS observation. The dispersion σ_Φ^2 of the fringe phase Φ was then estimated for each baseline $\boldsymbol{B}$ with the integration interval of 10,000 s centered on the time when the elevation of 3C 454.3 was 48.2°. It is likely that the effect of the instrumental phase variation is largely eliminated from the estimated dispersion because the instrumental variation is usually small and almost constant over several hours in the NMA. We estimated the thermal noise included within the observations of 3C 454.3 and obtained the rms thermal phase noise value of 5.0° with assumed correlated flux density of 18×10^{-26} $\mathrm{Wm^{-2}Hz^{-1}}$ for 3C 454.3 at 19 GHz.

As mentioned in Chapter 2, the SSF can be investigated from the dispersion of the fringe phase for large T in equation (11). The estimated dispersion of the fringe phase is plotted in Figure 3.8 for five baselines out of an available six integrated for 10,000 s. Data of one baseline (3–4) are not used here because of their low quality due to an unknown baseline-dependent failure.

Since we use 10-s averaged value of the fringe phase in calculating the dispersion in equation (11), the estimated SSF must be affected by averaging. Specifically, the amplitude of the SSF thus estimated should be smaller than that based on the raw (non-averaged) value which is more dispersive than the averaged value. It is also evident from

qualitative considerations that the effect should have significant consequences when the averaging time is shorter than the time required for the wind in the upper troposphere to pass over the baseline for which we measure the fringe phase. Assuming the wind velocity of 9 m/s and averaging time of 10 s, we see that the SSF value estimated on a baseline shorter than 90 m is affected by the averaging. In fact, the SSF values in Figure 3.8 after correction of the thermal noise contributions show rather clear bending down from the straight line at the 26-m baseline between antennas 2 and 4. We do not attempt to consider the averaging effect in any detail in view of the approximate nature of our estimation of the wind velocity and the thermal noise contributions. Instead, we simply remove the SSF value at the 26-m baseline from our least squares fitting in order to avoid possible bias due to the averaging effect.

We obtained the exponent α of 1.564 and C_l of 3.90×10^{-5} $\mathrm{cm}^{1-\alpha/2}$. These values are roughly similar to those adopted in the existing tropospheric models (for example, $\alpha = 1.667$ (Kolmogorov) and $C_l = 1.7 \times 10^{-5}$ $\mathrm{cm}^{1/6}$ in the work by *Dravskikh and Finkelstein* [1979]). However, it is too premature to make any definite conclusion on the parameter values since the obtained values are highly sensitive to the poorly estimated thermal noise contribution to the fringe phase fluctuations.

3.3 PAM2

3.3.1 Observations

The PAM2 experiments were conducted for about three and a half hours on January 28 and 29, 1995. The basic configuration of the PAM2 experiments is illustrated in Figure 3.9. The experiment on the first day is referred to as 'exp0128', and that on the second day as 'exp0129'. In PAM2 six antennas of the NMA observed 3C 279 at frequency of 146.81 GHz. The complex cross-correlation data were averaged for 10 s by the correlator. The five NRSM antennas were installed within several meters from each of the five NMA antennas. We were not able to install a NRSM antenna by sixth NMA antenna ('F' in Figure 3.9) since there are only five NRSM antennas. Phase difference between the signal from each of 'A', 'B', 'C', and 'D' antennas and that from the reference antenna ('E' in Figure 3.9) were measured using four vector volt meters for every one second. The resultant data were recorded in a personal computer controlling the vector volt meters together with the amplitude data of all the signals. The observing time and the baseline lengths are listed in Table 3.3.

3.3.2 Pre-processing

The major steps to produce the fringe phase difference from the millimeter- and centimeter-wave fringe phases are the followings:

1. 2π jumps in the CS fringe phase at 19.45 GHz were firstly corrected. This procedure was carried out almost automatically because the phase changed very smoothly and there was no spurious change greater than a quarter of π. The CS fringe phase measured at 19.45 GHz was effectively converted to that of 146.81 GHz by multipling the scaling factor equal to the ratio (146.81 / 19.45) of the observing frequencies. The corrected CS fringe phase thus obtained showed slow drifts due mainly to the slight movement of the satellite. Therefore, we removed from the phase the drift components which was calculated with a running mean for a time interval of 500 s. Since the personal computer controlling the vector volt meters failed to record the data for 10 s at 2:46:55 and 3:32:20 JST on January 29, the deficiency was interpolated before the running mean process.
2. The fringe-phase time series of CS were obtained for five baselines involving 'E' antenna only because of the data acquisition system. The time series of CS for other baselines were calculated by taking differences of the above time series.
3. The CS fringe-phase time series were further averaged for an accumulation time of the NMA data by taking a running mean for the time interval of 10 s.
4. Spurious 2π changes in the 3C 279 fringe phase had to be removed. This procedure was carried out graphically and the results were confirmed by visual inspection referring to the CS fringe phase measured at much lower frequency. This procedure was repeated until we made sure by the "closure test" [*Marcaide and Shapiro*, 1983] that 2π spurious phase changes were completely removed.
5. There were several antenna-dependent artificial spikes in the 3C 279 fringe phase due to the GP-IB control error of the antenna–based fringe rotator of the NMA. The data points were replaced by the interpolated ones if the spikes commonly appeared in the baselines involving a specific antenna at the same time.
6. Although the 3C 279 fringe phase did not show the large drifts unlike the CS's, we applied the same low-cut filtering procedure using the running mean for 500 s to the NMA fringe phase data in order to suppress the effects of the baseline error, the source position error, the instrumental phase drifts, and the source structure effect.
7. Fringe phase difference was derived by subtracting the CS fringe phase converted to the 146.81 GHz phase from the 3C 279 phase of the same baseline.

The contribution of the thermal noise to the 10-s accumulated 3C 279 fringe phase could not be estimated appropriately because the precise parameters of the system noise temperature and the correlated source flux density could not be obtained. In the season of the PAM2 experiments, each of the system noise temperature of the NMA antennas was 300–500 K. For example, adopting the system noise temperature of 400 K and a typical value of the flux density of 7×10^{-26} $\mathrm{Wm^{-2}Hz^{-1}}$ for 3C 279, which is guessed from a single antenna observations at 150 GHz [*Stevens* et al., 1994], the estimated thermal

noise is 6.4° where the aperture efficiency is 0.25 at 146 GHz, and the efficiency factor for the quantization is 1. Although this value must be roughly estimated, we assume that the contribution of the thermal noise to the 3C 279 fringe phase was 6.4°.

Since the CS signal is strong, the thermal noise contribution to the CS fringe phase must be much smaller than the atmospheric effect. Therefore, we do not attempt to estimate the thermal noise in the CS fringe phase regarding it as negligible. However, the contribution of the thermal noise may be different between the baselines because the more different performance than usual due to the very cold weather between the NRSM antennas whose receiver systems are not thermostatic might happen. In the following analyses, the anomalous phase fluctuations of the especial baselines are seen.

3.3.3 The Spatial Structure Function Measurements at the PAM2

We estimated the structure coefficient and exponent of the SSF at the moment of each experiment by means of the power law fitting of the rms fringe phase of 3C 279 estimated for the time interval of 1000 s. The thermal noise contribution was eliminated from each of the raw dispersion data according to equation (20). The rms phases of CS and 3C 279 with the integration time of 1000 s centered on the reference time are listed in Table 3.3 with the baseline lengths. The results of the power law fittings for 3C 279 centered on the reference time are shown in the top drawing of Figure 3.10.

The SSF derived from the CS data is in general agreement with that from the 3C 279 data through the PAM2 experiments if we disregard the data for the 13-th baseline (D–E: 61 m) showing anomalously large phase fluctuations. It can be noted from Table 3.3 that each of the CS rms phases of three baselines involving 'E' antenna (A–E, B–E, and C–E) is rather smaller than the 3C 279 rms phase of the equivalent baseline, while the rms phases of the other baselines match to each other, so that the dispersion of the CS rms phase from the power law fittings of CS is larger than that of the 3C 279 data through the experiments. It indicates that there might be something wrong in the instrument of 'E' antenna of the NRSM probably because the antenna configuration of the NRSM in the experiments was temporarily set in the use. In addition, since five more baselines of the NMA (totally, 15 baselines) are available in the SSF fittings, we adopt the SSF obtained from the 3C 279 data for further discussion.

The time variations of the structure exponent obtained by the fittings are shown in the bottom drawing of Figure 3.10. They range from 1.2 to 1.9 and from 1.0 to 1.7 for exp0128 and exp0129, respectively. The values are roughly consistent with the theoretical prediction from the Kolmogorov law ($5/3 = 1.667$) for the spatial scale smaller than the scale height of the water vapor in the troposphere. The averaged excess path length for 100-m baseline derived from the SSF is 0.172 mm and 0.148 mm for exp0128 and exp0129, respectively. These values are almost in the level expected at the best observing sites in the world like Mauna Kea, Hawaii or Andes in Chile. Then, from the mean rms

phase for 100-m baseline, the mean structure coefficient is calculated as $C_l = 0.798 \times 10^{-5}$ $cm^{1/6}$ and $C_l = 0.687 \times 10^{-5}$ $cm^{1/6}$ for exp0128 and exp0129, respectively, where the spatial frequency spectrum of the atmospheric fluctuations is assumed to have been the Kolmogorov power law (α =1.667) through the experiments. The structure coefficient values are much smaller than that obtained in PAM1 [*Asaki* et al., 1996] held in October 1994, since the PAM2 experiments were carried out in the extremely good (dry) weather condition at the winter time of Nobeyama.

3.3.4 The Standard Deviation of the Differential Fringe Phase

Time series of the difference between the 3C 279 fringe phase and the effective 146.81 GHz phase of CS are shown in Figure 3.11 along with their original phases. Although we analyzed all data obtained in the experiments, we show here the data for the range of separation angle from –20° to +20° for exp0128 data and from –30° to +10° for exp0129 data, respectively, because the correlation between the fringe phases of 3C 279 and CS was hardly seen when the separation angle was beyond the above ranges. Significant decrease of the fluctuation in the fringe phase difference is evident when the separation angle between the radio emitters approaches to the minimum value. This clearly shows the effectiveness of the PAM even in the case that the millimeter-wave interferometer phase of a target source are compensated using the centimeter-wave phase of a reference source.

The standard deviations of the fringe phase difference estimated for 1000 s are shown in Figure 3.12 with closed circles. Again, it is evident from the results for all the baselines except for the 13-th baseline that the standard deviation is small when the separation angle is near the minimum and increases as the separation angle increases up to a certain critical value. The critical separation angle depends on the baseline length and the scale height of the water vapor layer as discussed in Chapter 4 and in *Asaki* et al. [1996]. Specifically, the longer the baseline length is and/or the lower the phase screen is, the larger the critical separation angle is.

In the drawing of the 13-th baseline of Figure 3.11, it is hardly seen that the phase fluctuations are effectively eliminated from the corrected phases of the baseline because

1. the amplitude of the tropospheric fluctuations were originally small because of the shortness of the baseline;
2. uncalibrated instrumental effects that were larger than the atmospheric effects were included in the CS fringe phase of the baseline.

The standard deviations of the fringe phase difference with the integration time of 1000 s centered on the reference time are listed in Table 3.3 and plotted in Figure 3.13, compared with the SSF shown in Figure 3.10. We note that all the standard deviations except for the 13-th baseline's are smaller than the SSF and that they are separated into two groups:

those which are smaller than 20° level and those which are larger than the level. The later group is mainly constructed of the data whose baseline involves 'E' antenna (baseline ID of 4, 8, 11, and 13 in Figure 3.13) probably because the CS data of those baselines might be contaminated by the instrumental troubles of 'E' antenna as discussed in the previous section. For exp0128, the standard deviations of the third and tenth baseline (A–D and C–D) are higher than the 20° level because there are spiky phase noises in their fringe phase difference around the reference time. These values are greatly improved after extraction of the spiky noises or by phase compensation with explicit account of the time lag discussed in § 3.3.6, so that the rms phase of the fringe phase difference of the third and tenth baselines will originally be below the 20° level. The former group suggests that the degree of phase compensation with the PAM is independent of the baseline length and that the PAM phase calibration is able to compensate the atmospheric phase fluctuations to the level of 20° in the situation of the PAM2 experiments in which the separation angle was within a few degrees. From Figure 3.13, if the achievable calibration level was 20°, the PAM phase compensation meaningfully worked for baseline length longer than 70 m.

It is worth to note that the degree of phase compensation in the PAM2 experiments reached the rms level of 0.1 mm or smaller in terms of the excess path length owing to the good weather condition at Nobeyama during the experiments. This value is almost in the level required for the submillimeter-wave interferometry at the frequency of 500–800 GHz. Therefore, the present experiments show that the future large submillimeter array is well feasible at least when one uses the PAM or other method with equivalent performance for the compensation of the atmospheric phase fluctuations.

3.3.5 The Coherence Factor of the Differential Fringe Phase

Figure 3.14 shows the lag τ which maximizes the coherence factor η_c defined in equation (19) for the time series of the fringe phases of the two sources. Here, the integration time T is set to 200 s. The remarkably linear relationship between the lag τ maximizing the coherence factor and the separation angle of the two sources is evident from all the drawings except for those of the 13-th baseline. The linear trend is demonstrated in the present experiments much more clearly than in PAM1 probably owing to the much better weather condition. The results undoubtedly show the general validity of the hypotheses of the phase screen and frozen flow [see, for example, *Dravskikh and Finkelstein*, 1979]. The lag data for the range of separation angle between −10° and +10° were fitted to the linear function of time:

$$\tau_c(t) = u(t - t_0), \tag{21}$$

ignoring 3 σ outliers. The results are summarized in Table 3.4 and shown in Figure

3.14. Since the two sources are separated along the almost east–west direction on the phase screen parallel to the ground, we can estimate the east–west component of the wind velocity assuming the height of the phase screen. In Table 3.4, we list values of the rate u' of the change of τ_c per separation angle in radian. The velocity component is expressed by an equation $h \times \sec(\text{elevation angle})/u'$. Assuming 1500 m for the height of the phase screen, we obtained –17.9±1.2 m/s and –10.8±1.0 m/s for exp0128 and exp0129, respectively, which are in a reasonable range of values for the geostrophic wind in the upper troposphere.

3.3.6 Phase Compensation with Account of the Hypothesis of the Simple Frozen Screen

It is interesting to examine how well the degree of phase compensation is improved if we explicitly take into account the time lag between the two fringe-phase time series which maximizes the coherence factor. For this purpose, we generated new time series of the CS fringe phase in terms of shifting the original CS time series by the time lag determined in the least squares fitting as described in the previous section. The difference between the time series of the 3C 279 fringe phases and the new time series of the CS fringe phase are shown in Figure 3.11, and the standard deviations of the difference are shown in Figure 3.12 with open circles. It is evident that both the degree and the effective area of the phase compensation are remarkably improved. This again shows the appropriateness of the structural model of the phase screen and frozen flow in the present experiments.

3.3.7 The Scaling Factor for Conversion of the Lower Frequency Phase to the Higher Frequency Phase

Although the effectiveness of the PAM phase compensation using different observing frequencies for the target and reference sources is well demonstrated in the above results, the following important question is not yet to be answered: is the refractivity of the water vapor in the troposphere strictly non-dispersive?

In order to answer to the question, we calculated the standard deviation of the differential fringe phase at each baseline for 1000 s interval centered at the moment of the zero time lag varying the scaling factor for conversion of the 19.45 GHz phase to the 146.81 GHz phase. The minimum standard deviation was always obtained when the scaling factor is around the non-dispersive value (146.81 / 19.45). However, the scatter is rather large: from 0.80 to 1.12 in terms of the scaling factor normalized by the non-dispersive value. Apparently, the effects of the residual phase fluctuations and the thermal noise are too large to make the sensitive determination of the optimal scaling factor. The only conclusion we can draw at this moment is that the non-dispersive scaling factor is good enough to realize the effective phase compensation with the PAM using mm- and cm-waves for observing the target and reference sources, respectively.

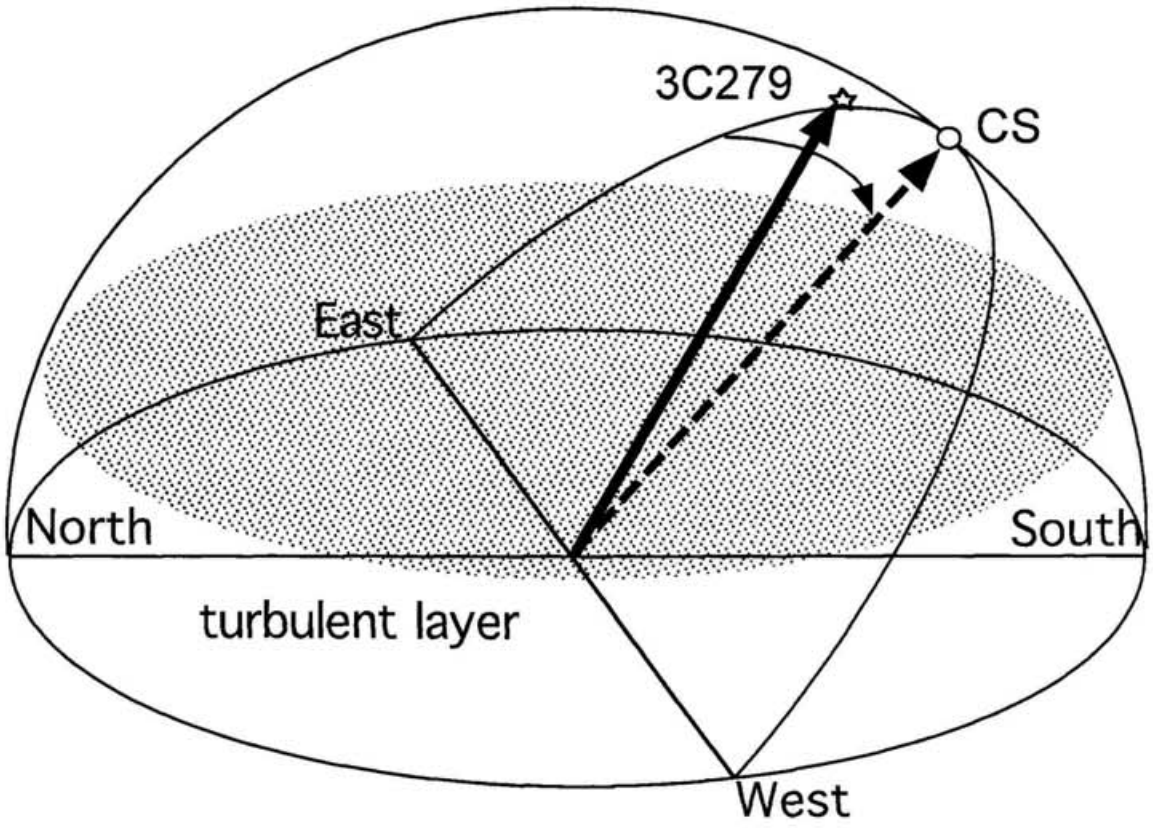

Figure 3.1: The overview of the phase compensation experiments using the Nobeyama Millimeter Array and the Nobeyama Radio Seeing Monitor.

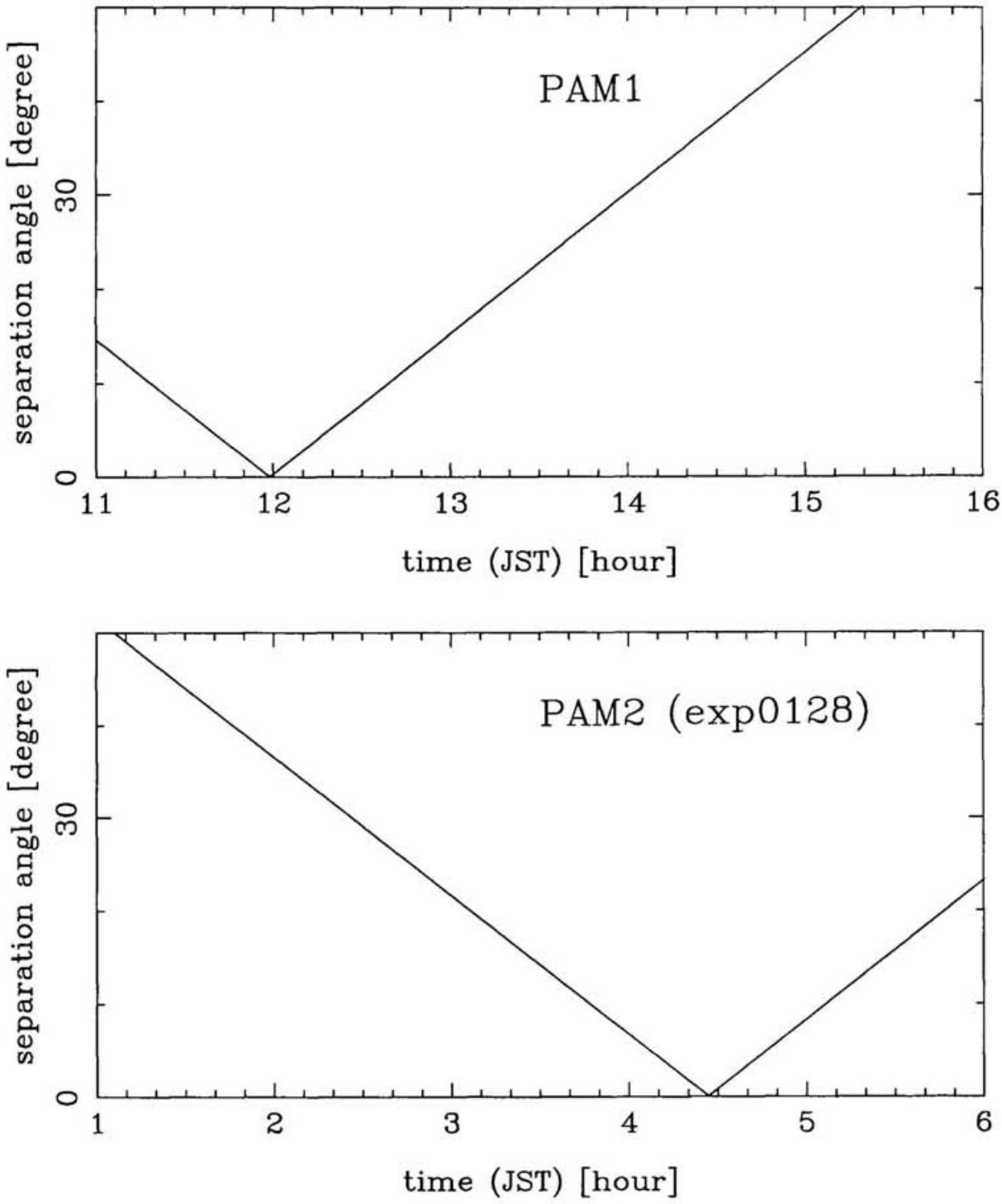

Figure 3.2: The separation angle between 3C 279 and Japanese Communication Satellite. Top drawing is during PAM1 (October 5, 1994), and bottom one is during exp0128 of PAM2 (January 28, 1995). The time when the separation angle reached its minimum was 11:59 JST and 4:27 JST for PAM1 and PAM2, respectively.

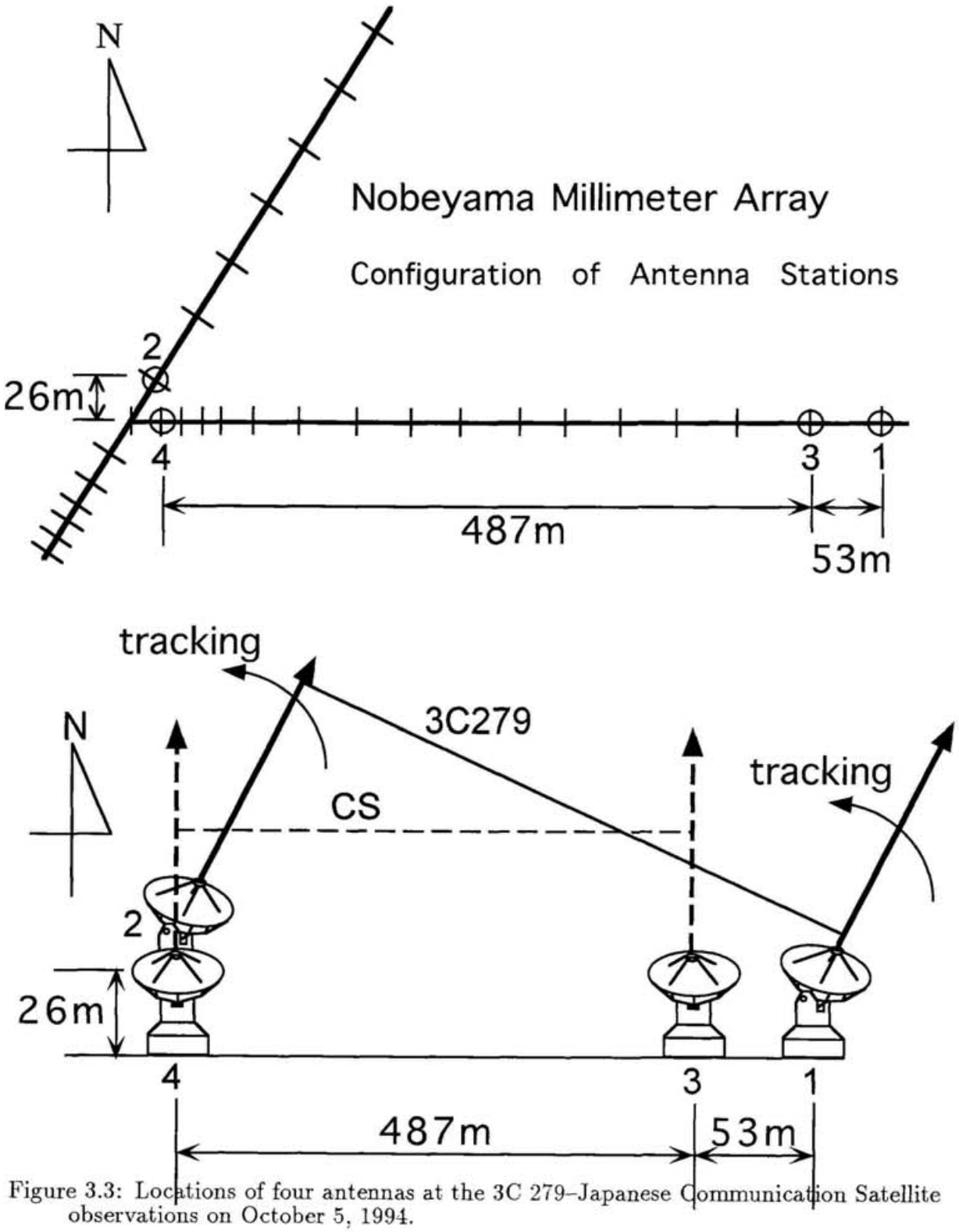

Figure 3.3: Locations of four antennas at the 3C 279–Japanese Communication Satellite observations on October 5, 1994.

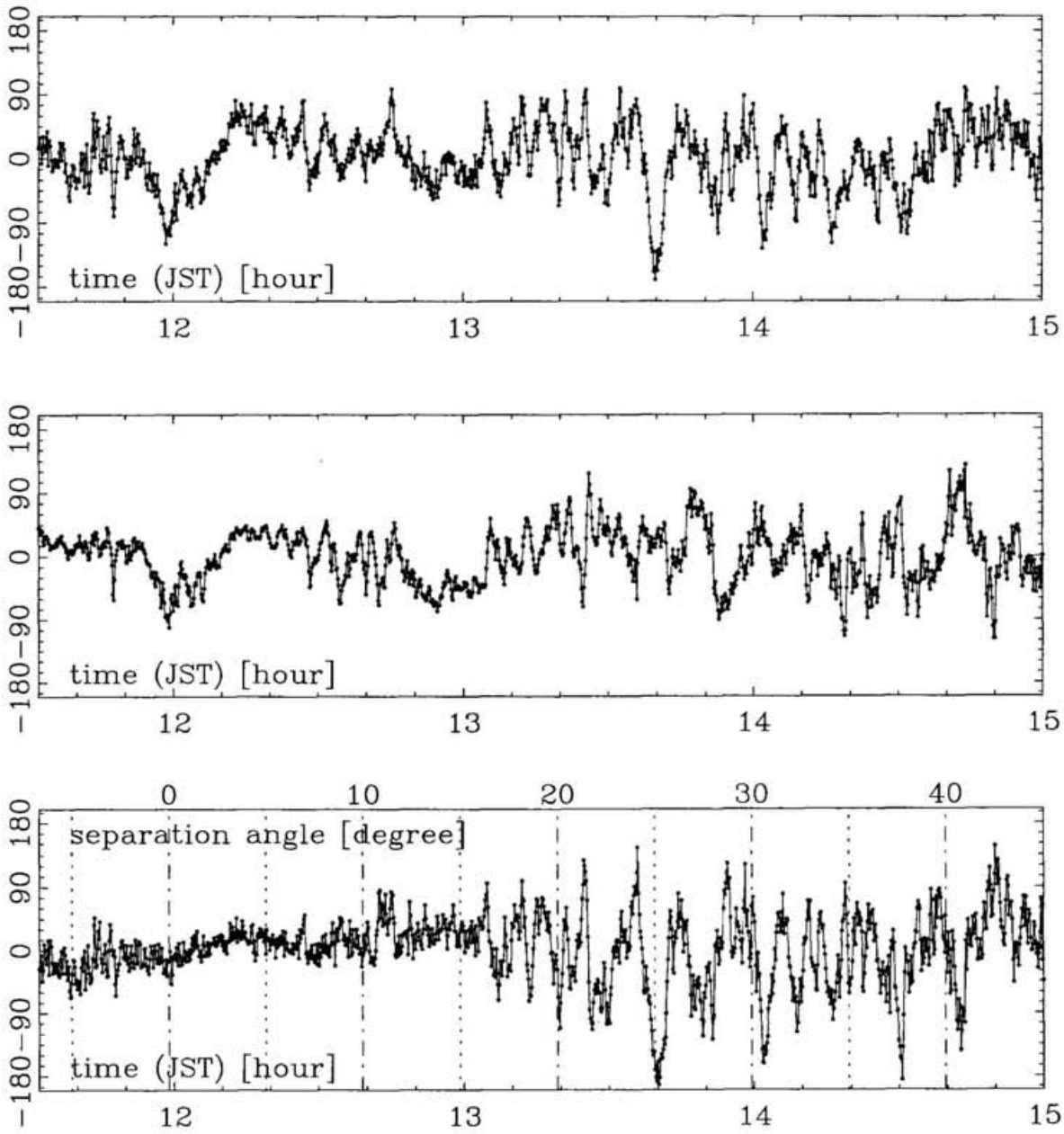

Figure 3.4: Fringe phases of 3C 279 (top), Japanese Communication Satellite (middle), and their difference (bottom). The abscissa is JST (Japan Standard Time) in hour, and the ordinate is fringe phase in degree at frequency of 19.45 GHz. One data-point corresponds to 10-s averaged value. It is evident that the fluctuation in the fringe phase difference becomes smaller with decreasing angular separation between the sources.

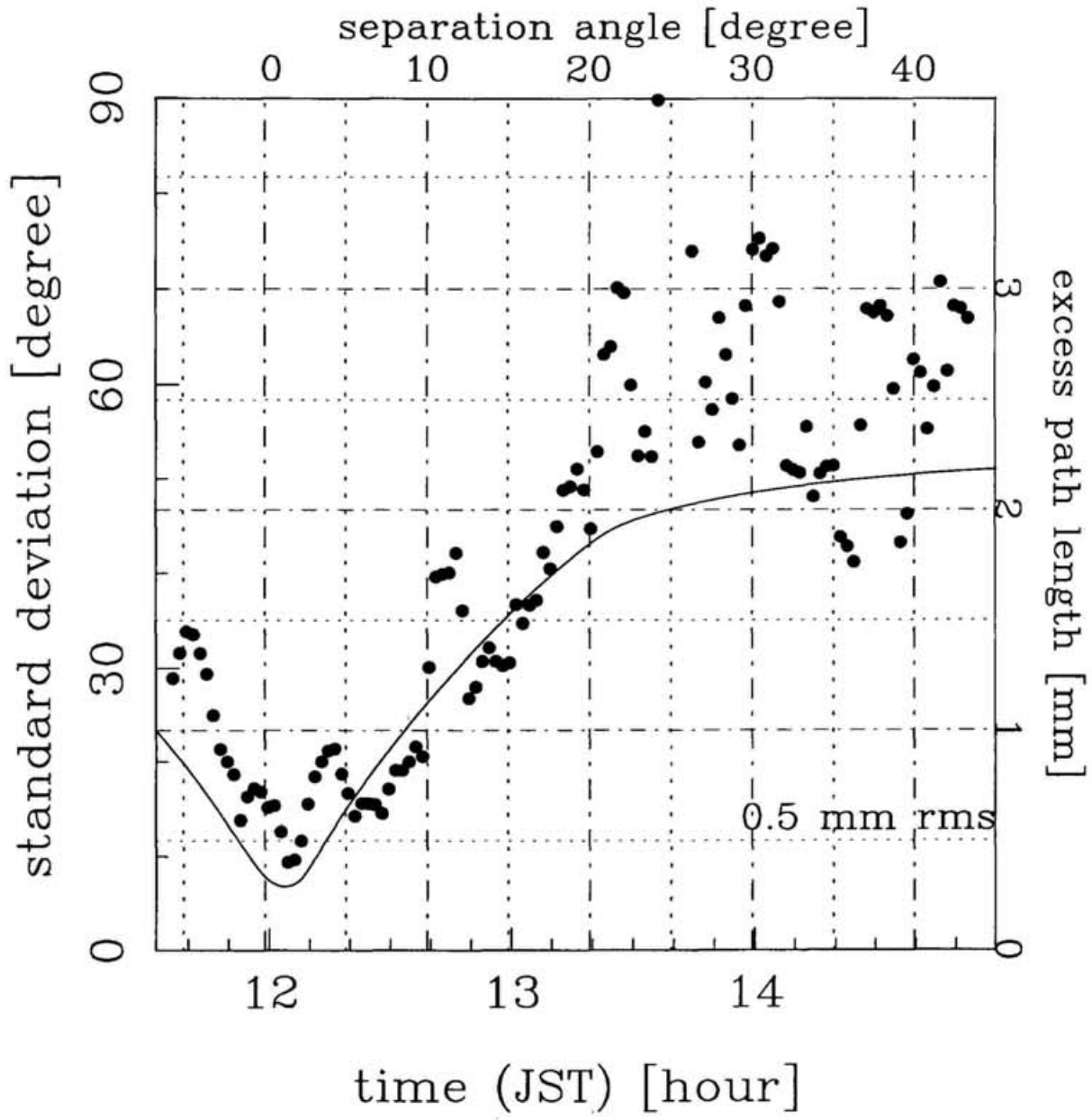

Figure 3.5: The standard deviation of the fringe phase difference calculated with the integration time of 500 s. Note that the right ordinate is excess path length in mm. The gradual increase of the standard deviation with the growing separation angle is saturated at 13:20 JST when the separation angle reaches 20°. The solid line shows the result of a simulation based on a statistical model, which is treated in Chapter 4.

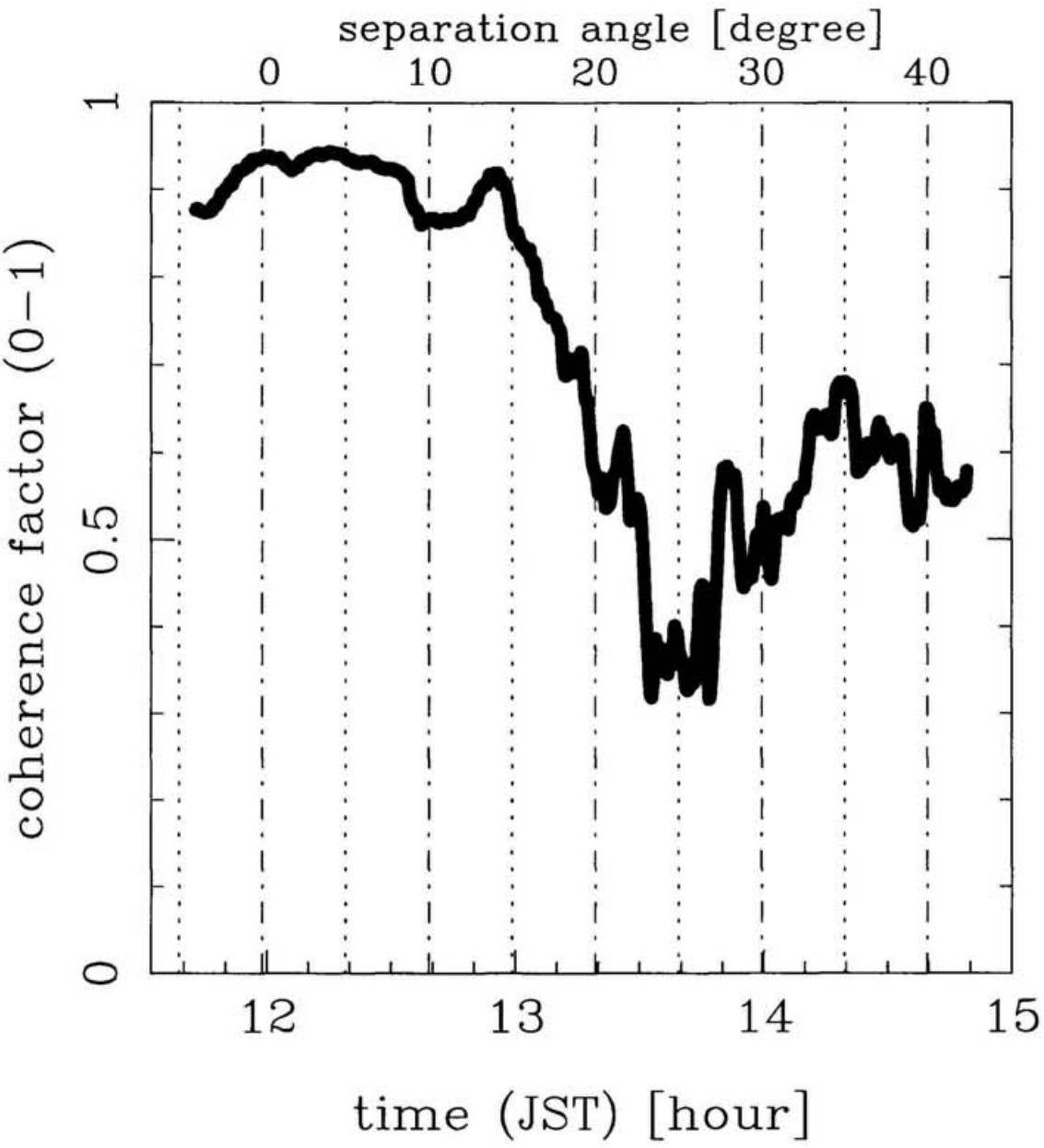

Figure 3.6: The coherence factor of the fringe phase difference with zero time lag.

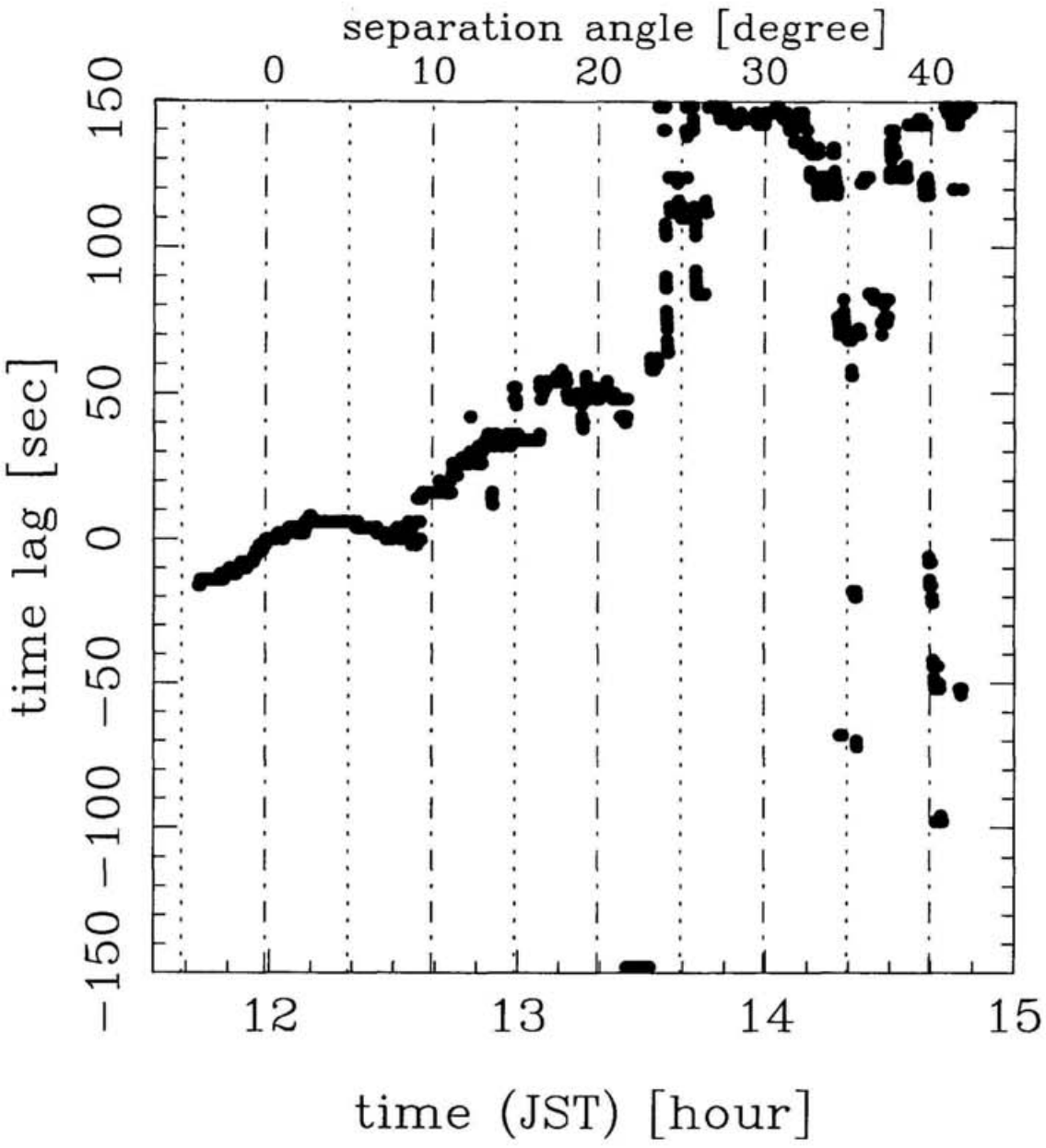

Figure 3.7: The time lag maximizing the coherence factor of the fringe phase difference. The lag is almost 0 s at the minimum separation angle and increases monotonically with time.

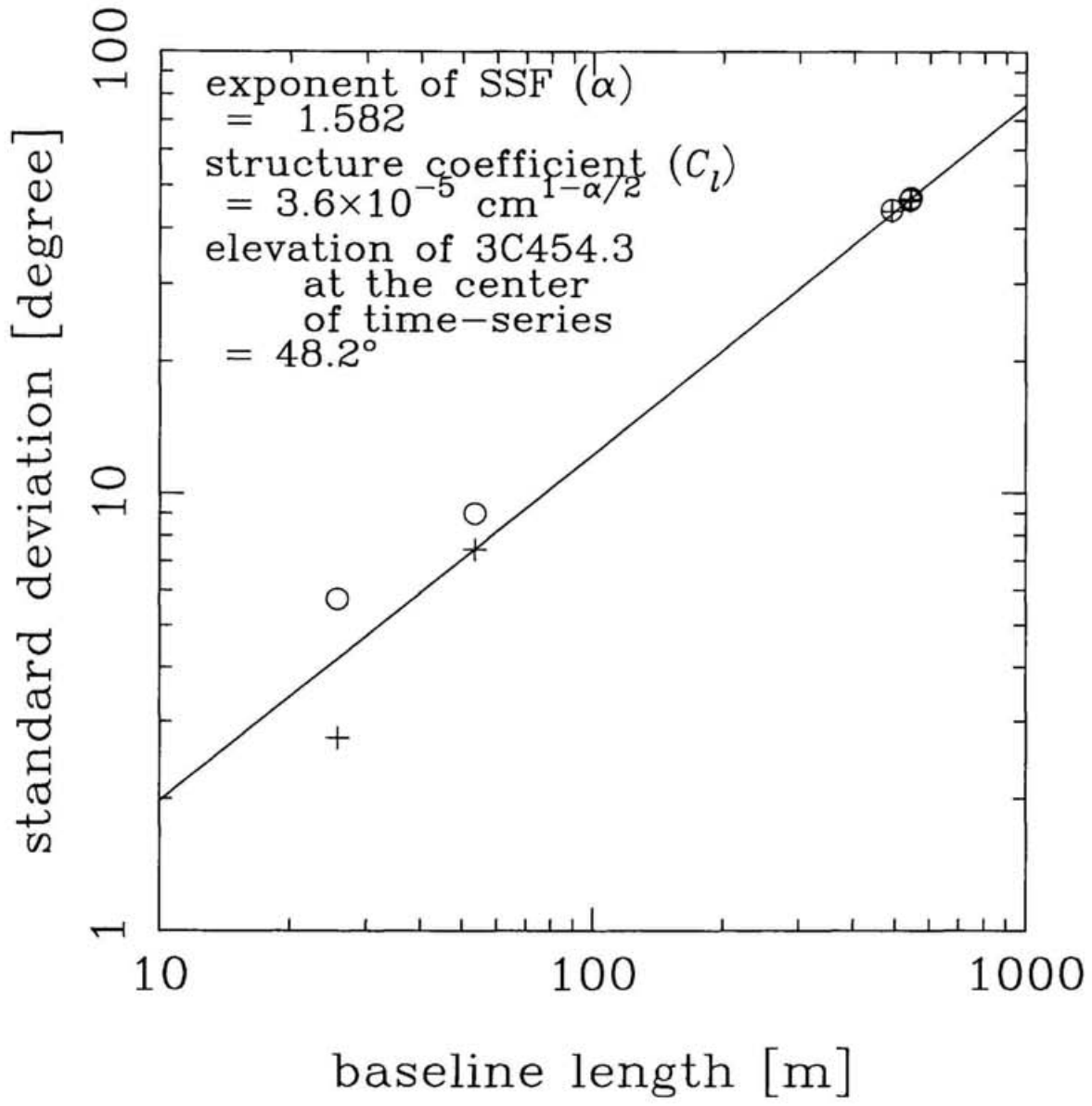

Figure 3.8: Power law fitting of the spatial structure function derived from the data of 3C 454.3 observations. Circles show standard deviations of the fringe phases obtained for five baselines, and crosses show the standard deviations after subtraction of estimated thermal noise contributions. Note that right two points are overlapped because their baselines are nearly equal. The parameters of the SSF are derived by the least squares fitting (solid line) to the corrected rms phase except for the minimum baseline data, which should be affected by the averaging effect.

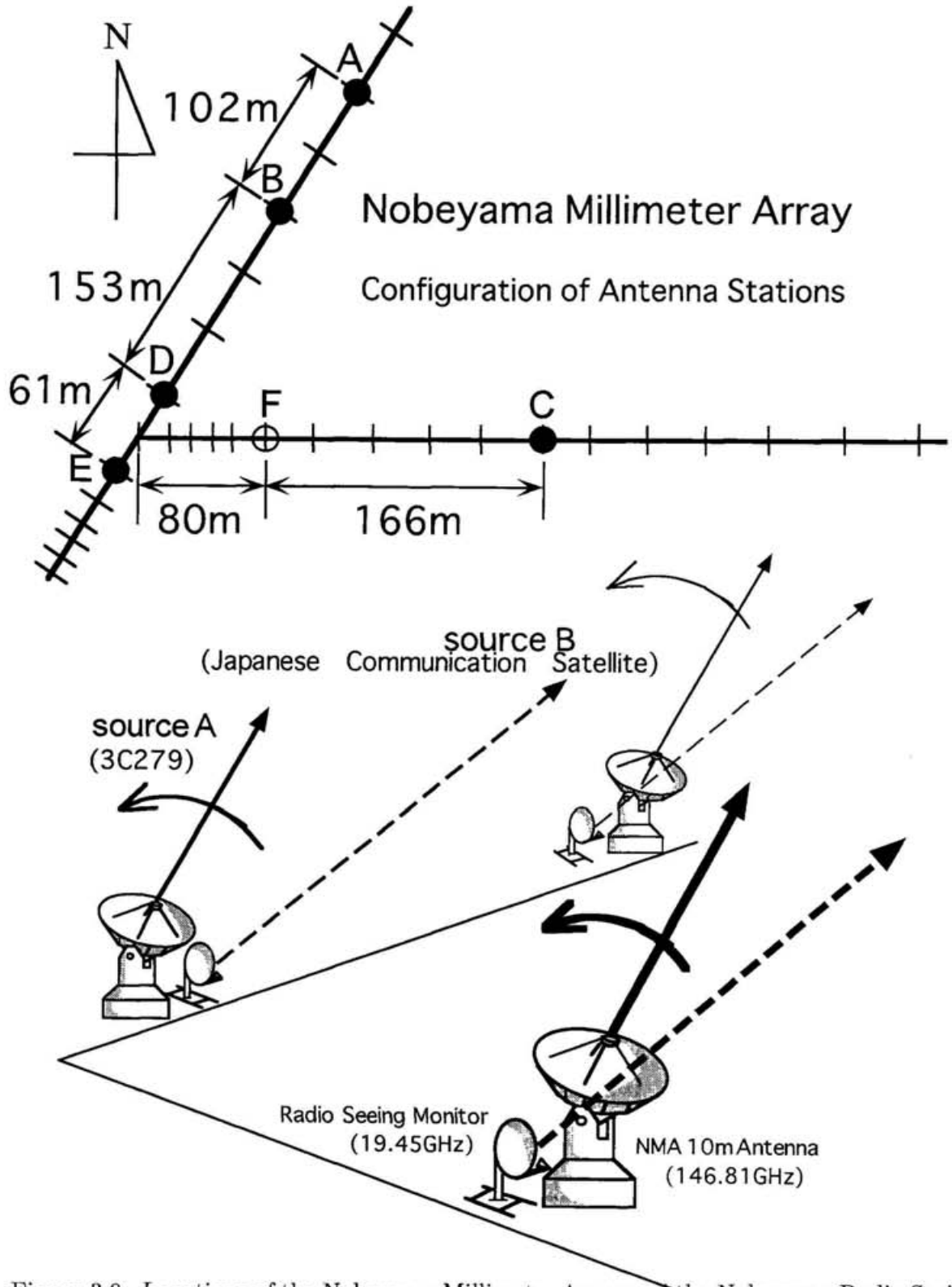

Figure 3.9: Locations of the Nobeyama Millimeter Array and the Nobeyama Radio Seeing Monitor at the 3C 279–Japanese Communication Satellite observations. All the circles in top drawing represent the stations where the NMA antenna was set, and five closed ones represent the stations where the NRSM antennas were installed.

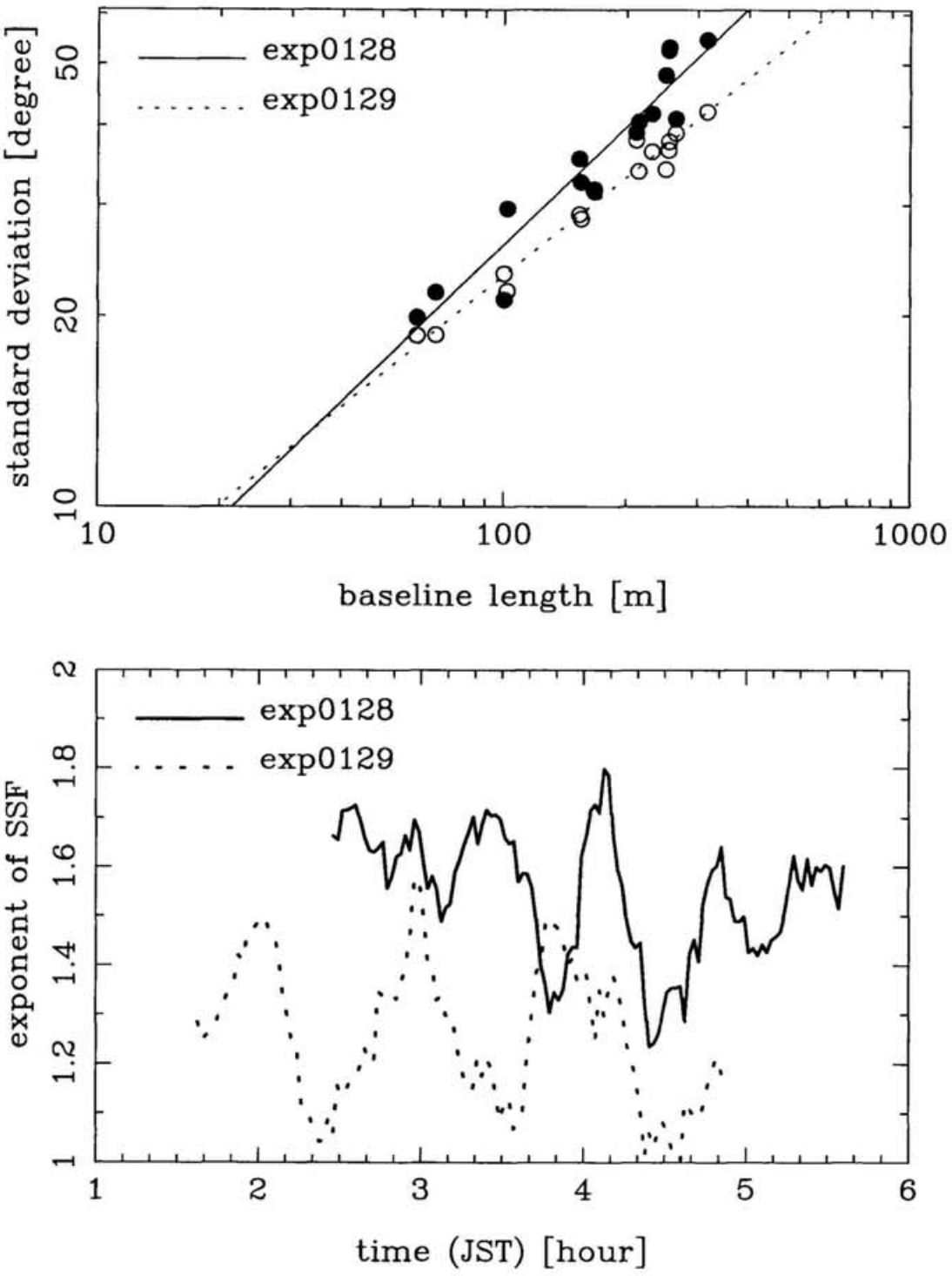

Figure 3.10: Estimation of the spatial structure function of the PAM2 experiments. Top drawing is the power law fitting of the rms phases estimated from the 3C 279 fringe-phase time series with integration time of 1000 s centered on the time when the separation angle was minimum, and bottom one is time variation of the structure exponent of the SSF. In top drawing, there are open and closed circles representing the 3C 279 rms phases for exp0128 and exp0129, respectively.

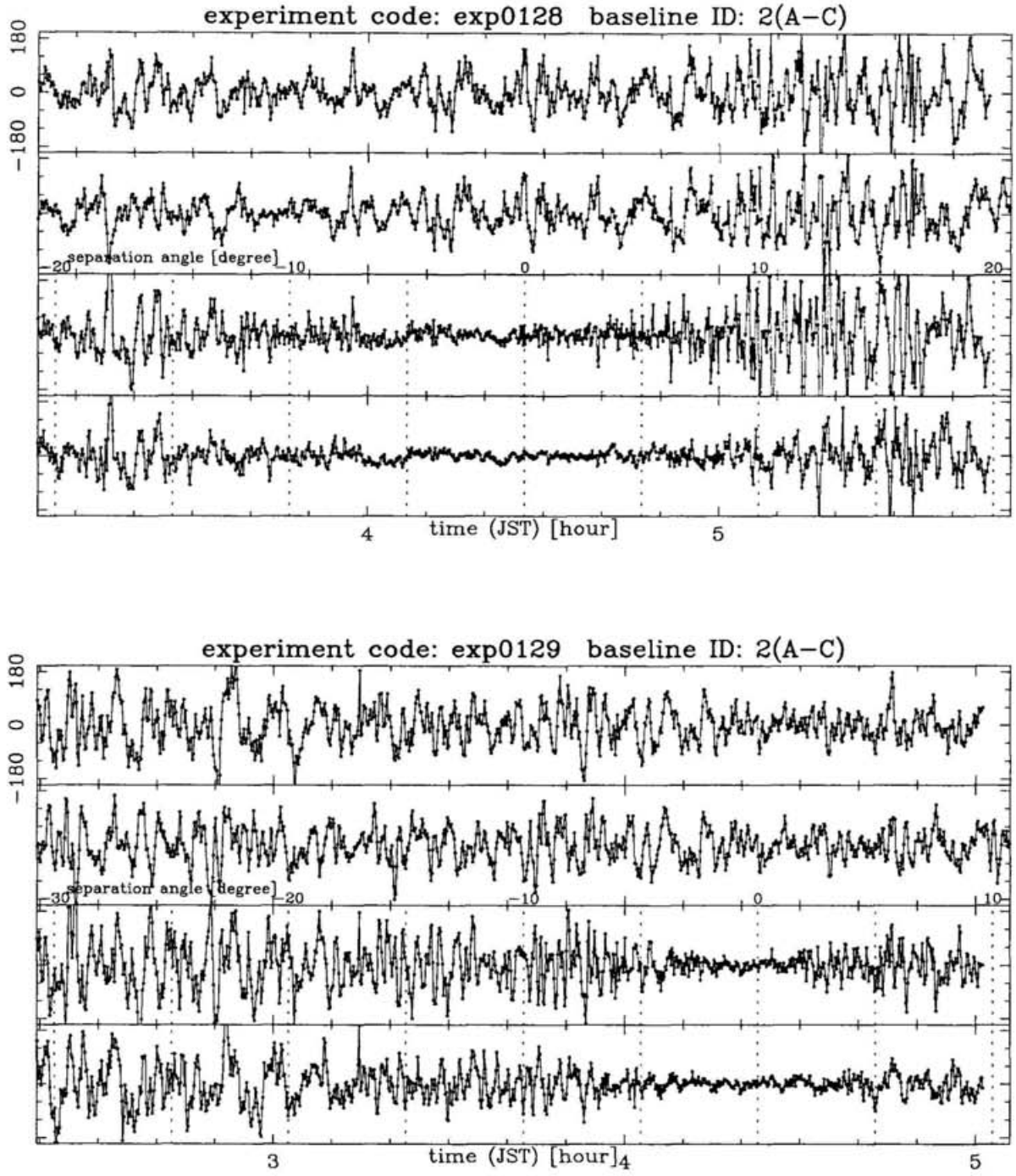

Figure 3.11 (a): Fringe phases of PAM2, baseline 2 (A–C) of exp0128 and exp0129 in first and bottom four drawings, respectively. Each set including four time series shows the fringe phases of 3C 279, Japanese Communication Satellite, their difference at same time comparison, and the difference with considering time-lag-inserted phase correction. The abscissa is JST (Japan Standard Time) in hour and the ordinate is fringe phase in degree at frequency of 146.81 GHz. One data-point corresponds to 10-s averaged value. It is evident that the fluctuations in the fringe phase difference becomes smaller with decreasing angular separation between the sources.

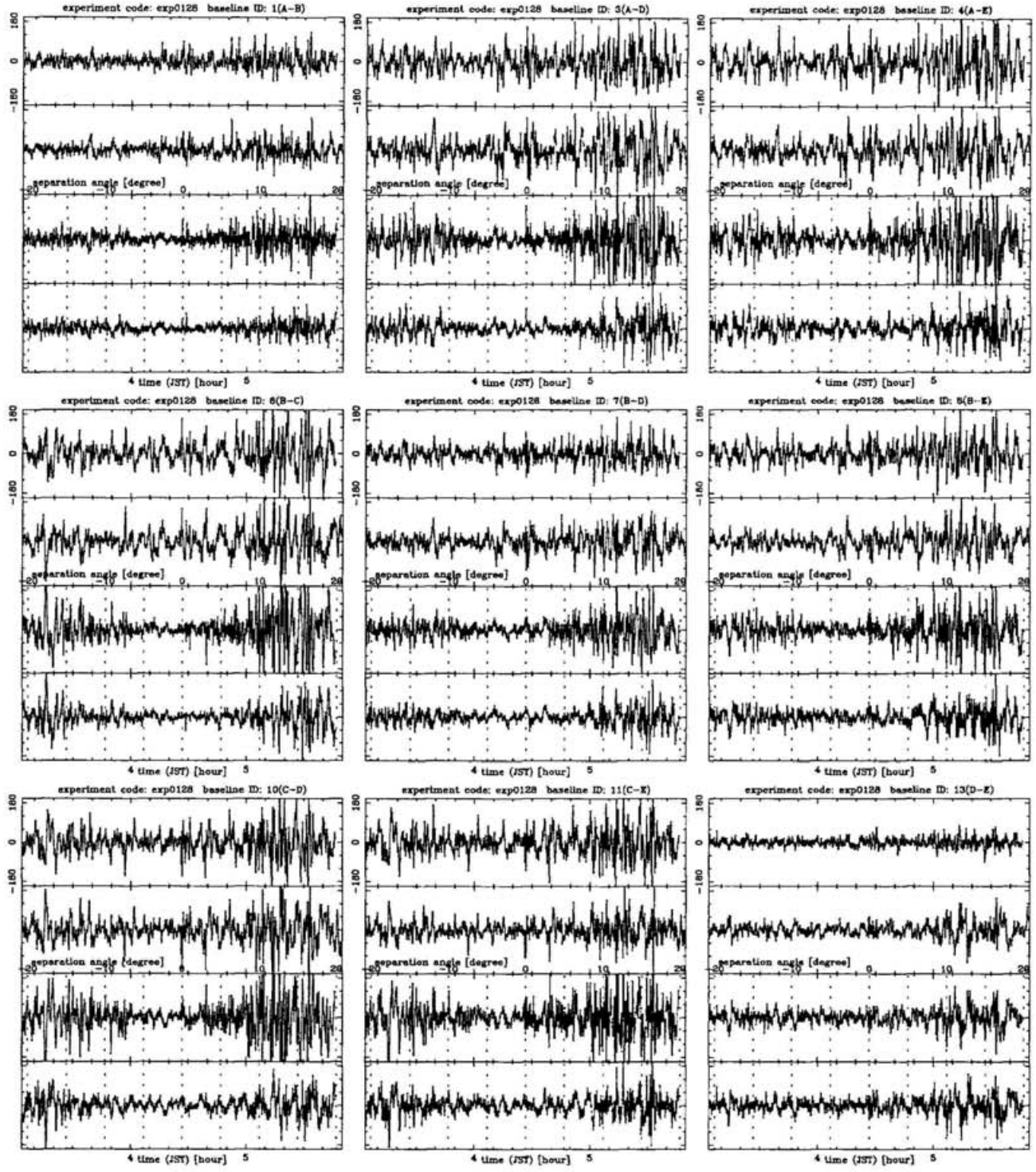

Figure 3.11 (b): Fringe phases of 3C 279 and CS, and their differences of exp0128 of PAM2.

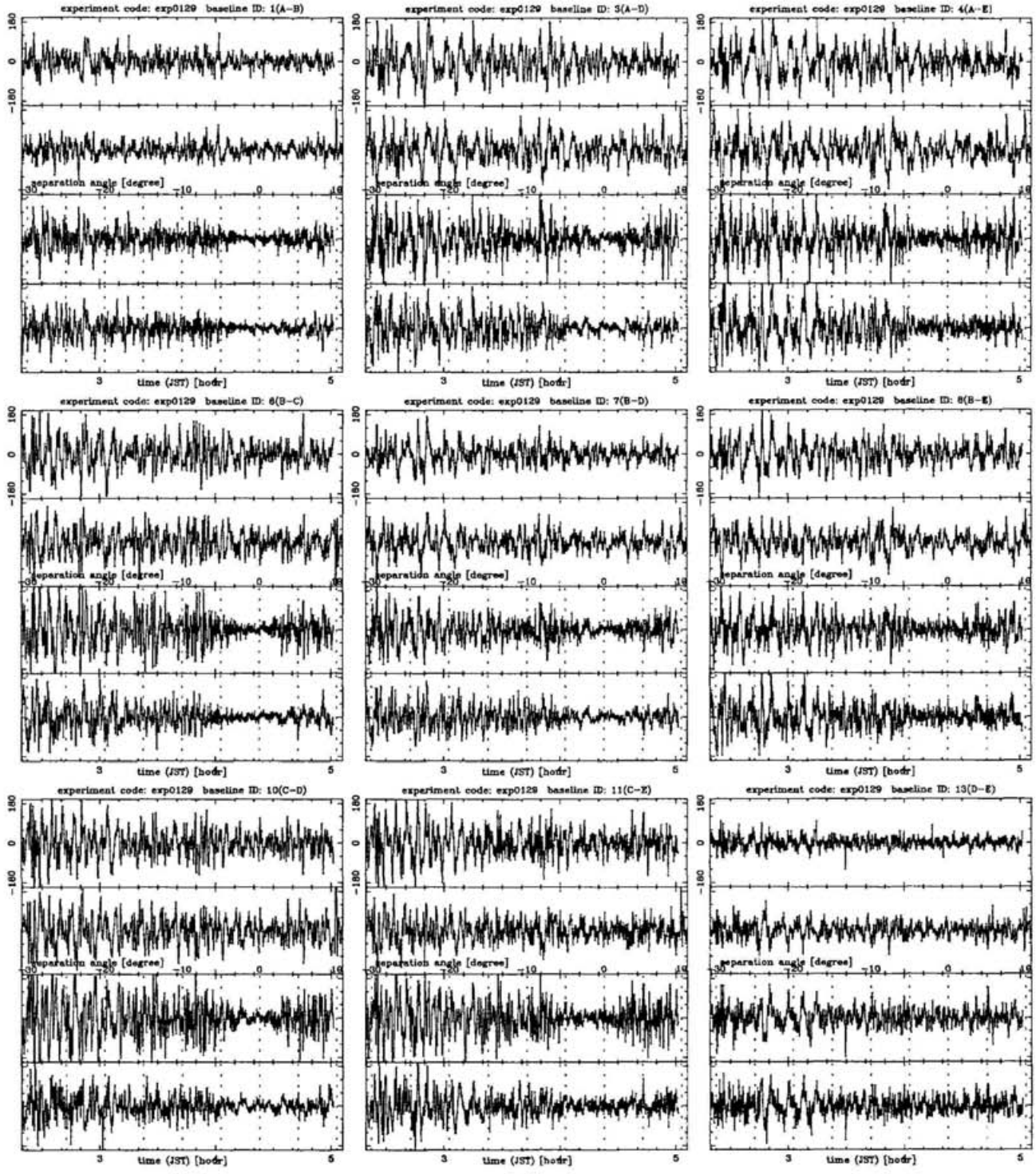

Figure 3.11 (c): Fringe phases of 3C 279 and CS, and their differences of exp0129 of PAM2.

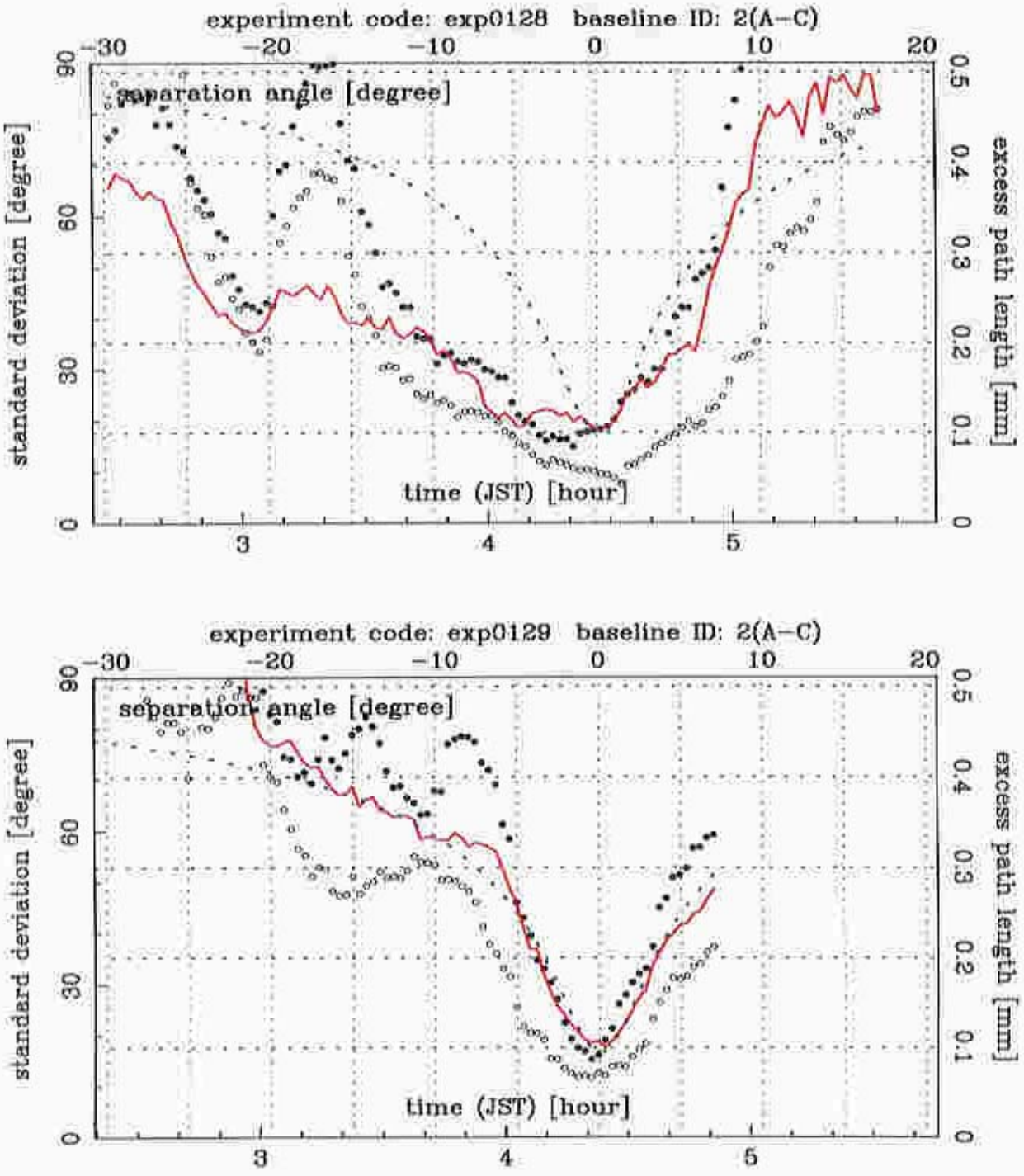

Figure 3.12 (a): The standard deviations of the fringe phase difference calculated with the integration interval of 1000 s of PAM2, baseline 2 (A–C) of exp0128 and exp0129 in top and bottom drawing, respectively. Closed and open circles represent the rms values of time-synchronized and time-lag inserted phase correction, respectively. It can be seen that the gradual increase of the standard deviations with the growing separation angle. The solid and dashed lines show computer simulation results based on a statistical model, which is treated in Chapter 4.

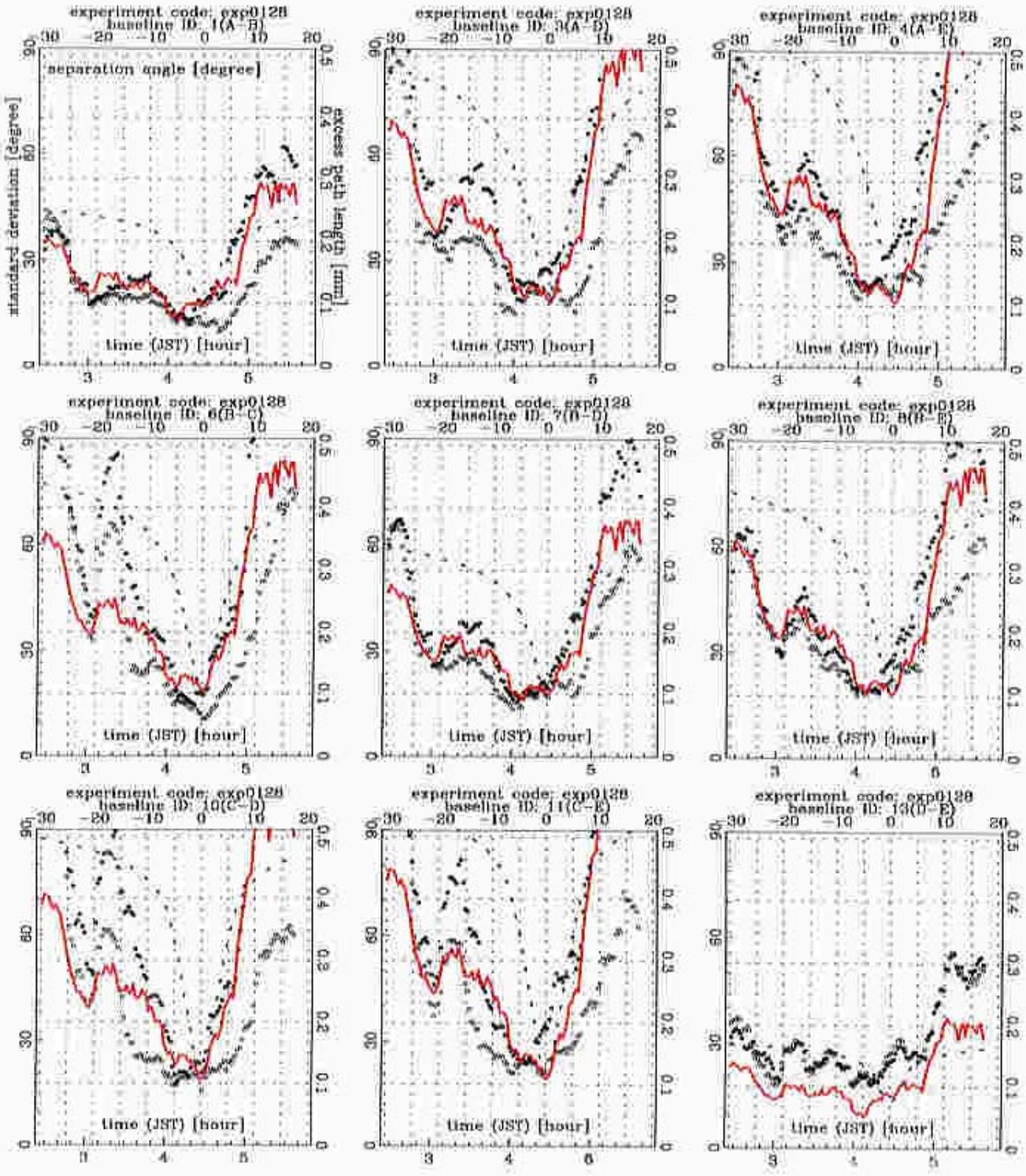

Figure 3.12 (b): The standard deviations of the fringe phase differences calculated with the integration interval of 1000 s of exp0128 of PAM2.

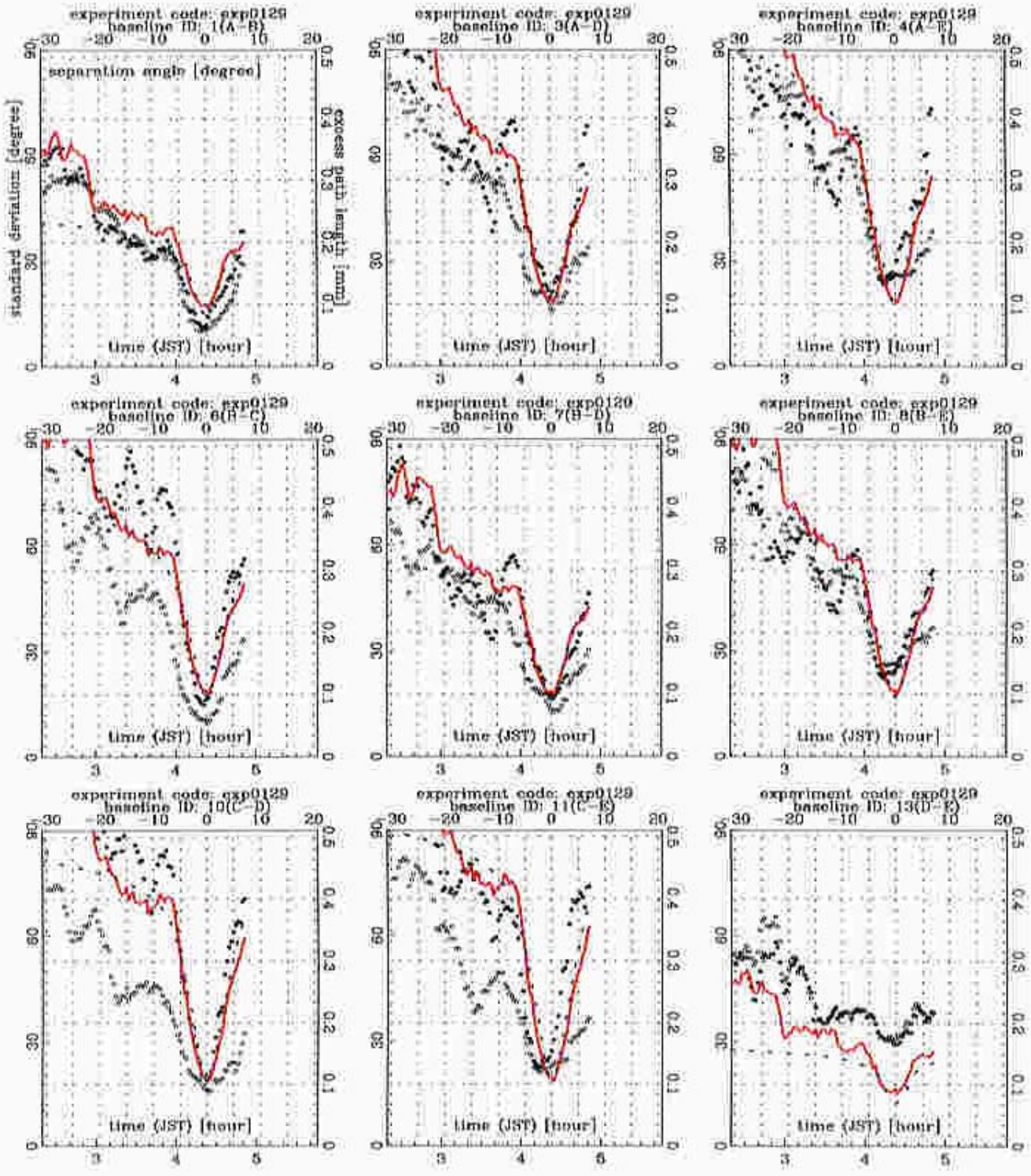

Figure 3.12 (c): The standard deviations of the fringe phase differences calculated with the integration time of 1000 s of exp0129 of PAM2.

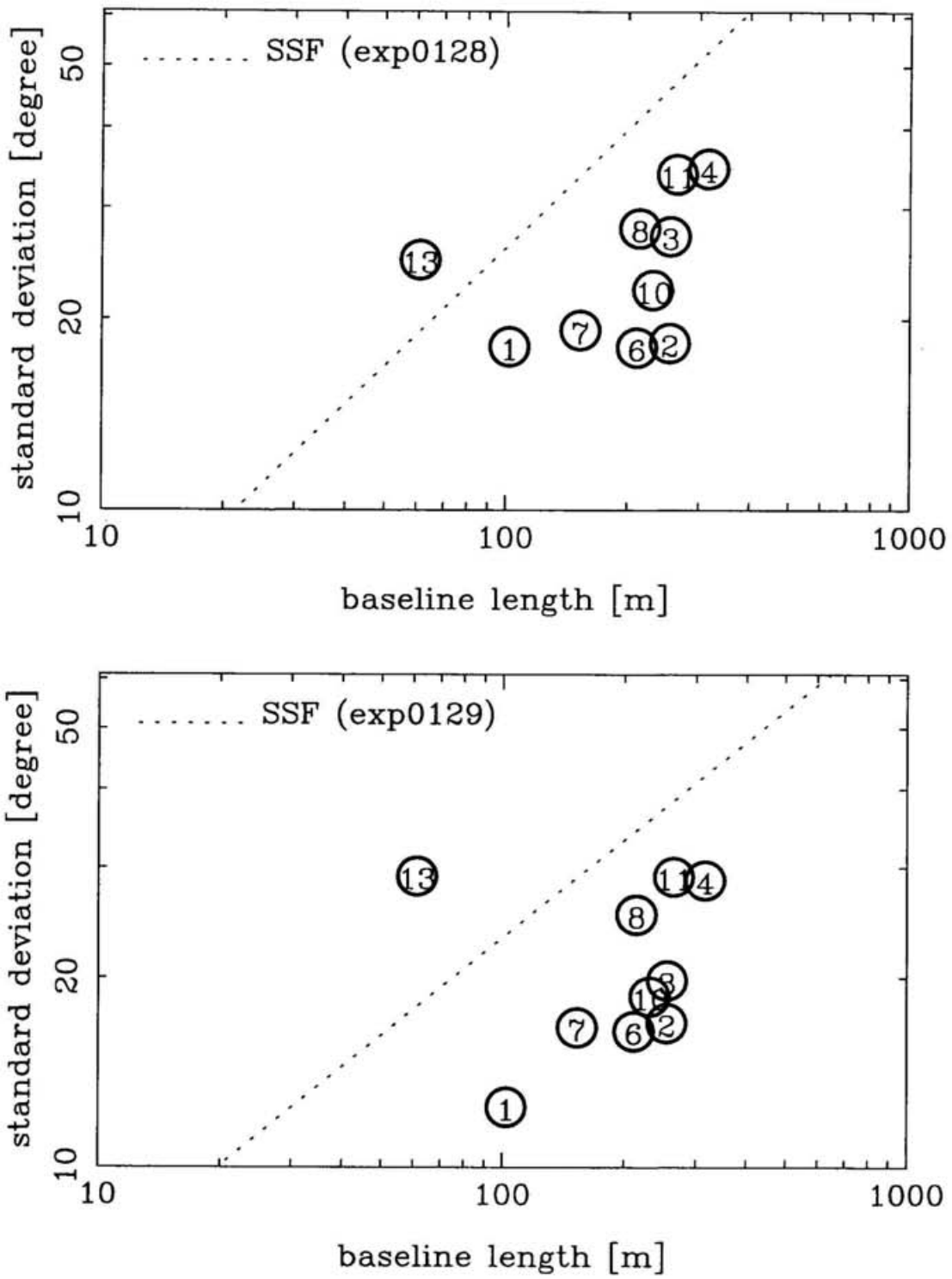

Figure 3.13: Standard deviations of the fringe phase difference with the integration time of 1000 s, compared with the SSF of PAM2. The top and bottom drawing is at exp0128 and exp0129, respectively, centered on the time when the separation angle was minimum. The open circles are rms phases of the phase difference with the baseline ID listed in Table 3.3. The dashed lines represent the SSF shown in Figure 3.10.

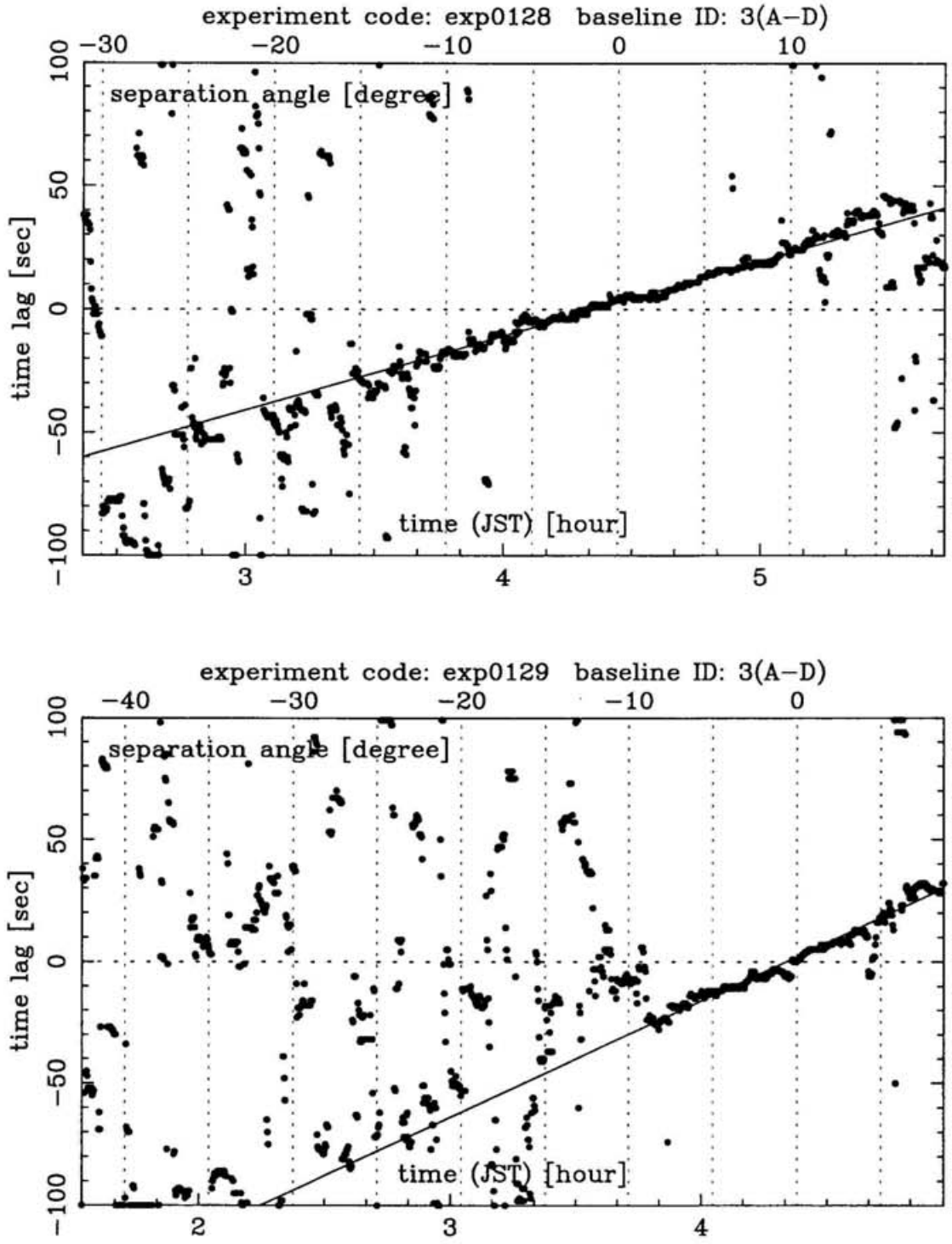

Figure 3.14 (a): The time lag maximizing the coherence factor of the fringe phase difference of PAM2, baseline 2 (A–C) of exp0128 and exp0129 in top and bottom drawing, respectively. The lag is almost 0 s at the minimum separation angle and increases with increasing time. The solid lines represent the results of least squares fitting the data of the separation angle between $-10°$ and $+10°$ ignoring 3 σ outliers. Where the separation angle is large, the lag must be proportional to tan(separation angle), which can be negligible where the separation is small.

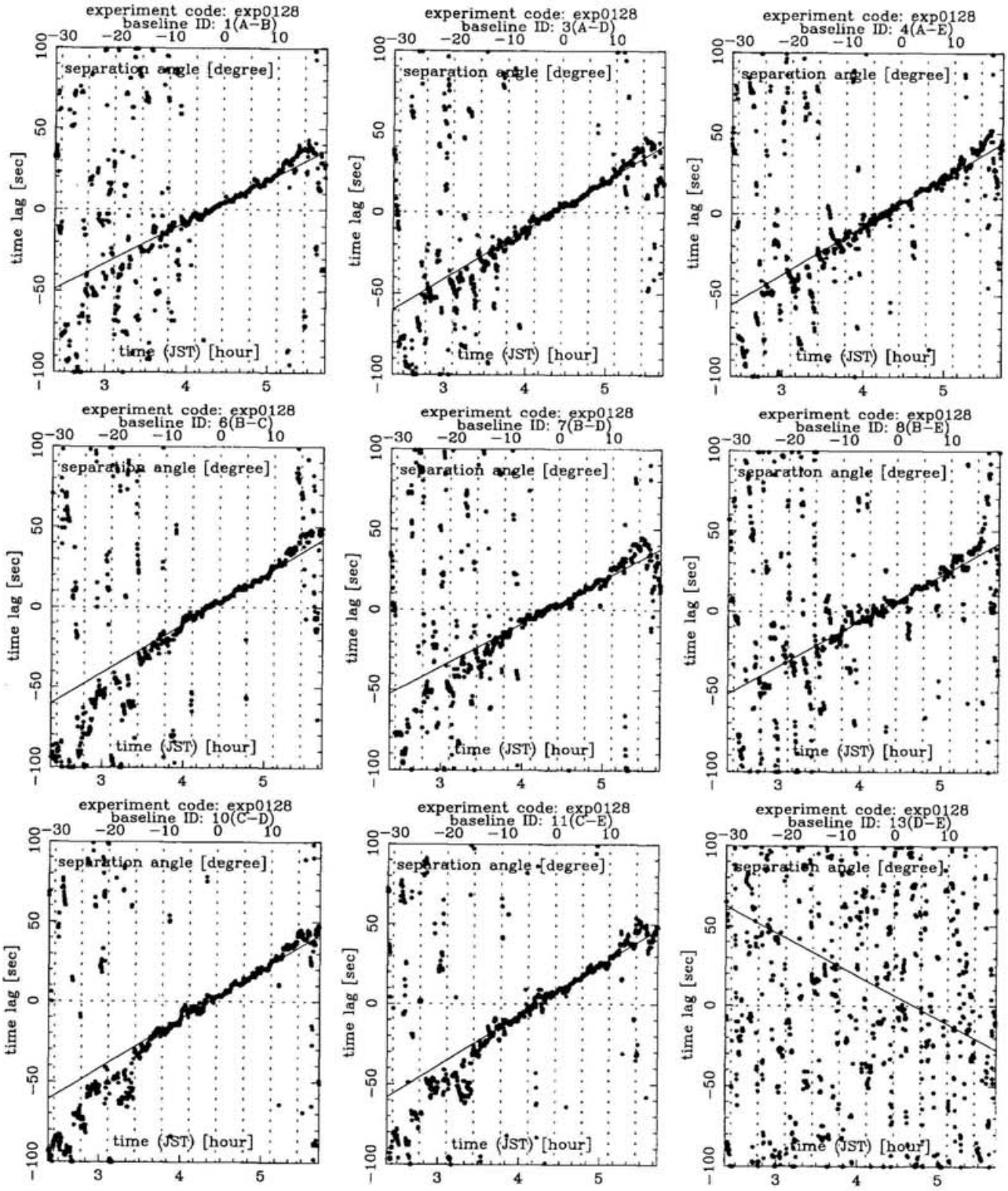

Figure 3.14 (b): The time lag maximizing the coherence factor of the fringe phase difference of exp0128 of PAM2.

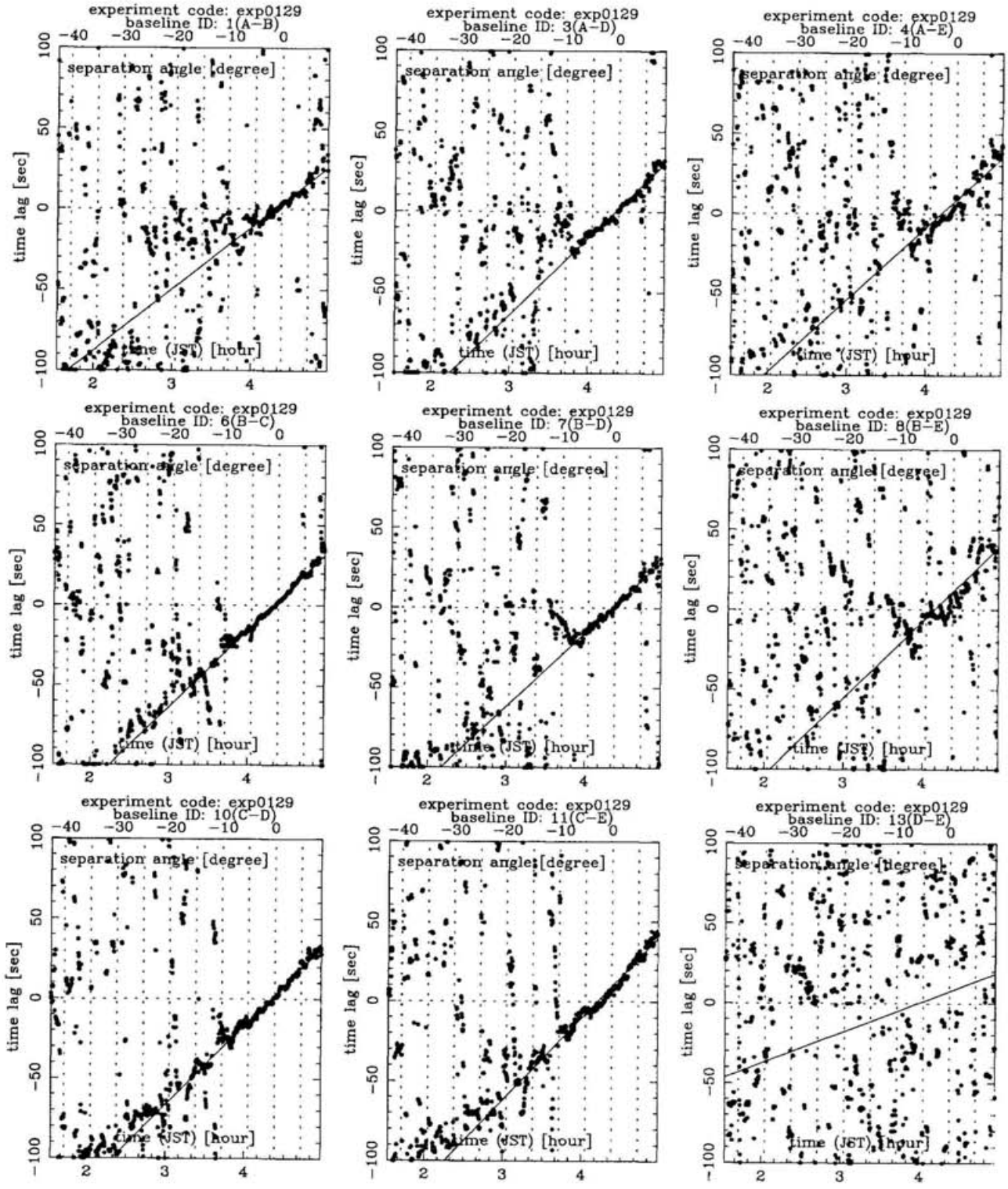

Figure 3.14 (c): The time lag maximizing the coherence factor of the fringe phase difference of exp0129 of PAM2.

source	right ascension (J2000)	declination (J2000)	azimuth	elevation
3C 279	$12^h56^m11.2^s$	$-5°47'22''$	–	–
3C 454.3	$22^h51^m29.5^s$	$15°52'54''$	–	–
Communication Satellite	–	–	184.16°	48.27°

Table 3.1: Source positions. Japanese Communication Satellite is almost stationary, and 3C 279 passed very close to Japanese Communication Satellite. Quasar 3C 454.3 was only observed in PAM1 for measuring the spatial structure function.

clusterID	east		west	
antenna code	1	2	3	4
system noise temperature	2.2×10^3 K	2.0×10^3 K	2.0×10^3 K	2.2×10^3 K
received radio source	3C 279	CS	3C 279	CS
(observing time)	(11:30-16:00 JST Oct 5, 1995)			
received radio source	3C 454.3			
(observing time)	(17:30-00:30 JST Oct 5, 1995)			

Table 3.2: System temperature, in SSB receiving system, of the Nobeyama Millimeter Array antennas in the PAM1 experiments. The system temperature was unusually high because we used uncooled 19-GHz low-noise amplifiers which were not standard in the NMA.

		exp0128 2:15–5:50 JST January 28, 1995			exp0129 1:25–5:5 JST January 29, 1995		
baseline ID	baseline length [m]	σ_{3C279} [deg]	σ_{CS} [deg]	$\sigma_{3C279-CS}$ [deg]	σ_{3C279} [deg]	σ_{CS} [deg]	$\sigma_{3C279-CS}$ [deg]
1 (A–B)	102.0	29.6	29.7	18.1	21.9	22.4	12.5
2 (A–C)	254.3	52.6	49.9	18.4	36.6	39.1	16.9
3 (A–D)	255.0	53.2	52.8	27.1	37.8	40.4	19.8
4 (A–E)	316.2	54.7	49.2	34.6	42.1	36.7	28.6
5 (A–F)	250.5	48.1	–	–	34.2	–	–
6 (B–C)	211.2	39.1	37.4	18.0	38.0	38.8	16.4
7 (B–D)	153.0	35.5	39.2	19.2	29.0	31.2	16.7
8 (B–E)	214.2	40.6	33.7	27.9	34.0	29.3	25.2
9 (B–F)	154.6	32.6	–	–	28.5	–	–
10 (C–D)	231.2	41.8	41.4	22.3	36.5	39.3	18.7
11 (C–E)	264.8	41.0	31.0	33.9	38.9	32.5	29.0
12 (C–F)	166.7	31.8	–	–	31.5	–	–
13 (D–E)	61.2	19.9	21.8	24.8	18.6	23.1	29.0
14 (D–F)	68.1	21.8	–	–	18.7	–	–
15 (E–F)	100.2	21.2	–	–	23.3	–	–

Table 3.3: Observing time, baseline lengths of the Nobeyama Millimeter Array configuration in the PAM2 experiments, and the rms phases of the 3C 279, Japanese Communication Satellite, and differential fringe phase with the integration time of 1000 s centered on the time when the separation angle was minimum. The power law fittings of the 3C 279 values are shown in bottom drawing of Figure 3.10.

	exp0128			exp0129		
baseline ID	u [sec/hour]	u' [sec/rad]	t_0 (JST)	u [sec/hour]	u' [sec/rad]	t_0 (JST)
1 (A–B)	25.5	97.5	4:17:11	38.2	146.3	4:17:50
2 (A–C)	30.2	115.6	4:20:51	47.9	183.6	4:19:21
3 (A–D)	30.2	115.7	4:21:10	47.8	182.9	4:20:19
4 (A–E)	29.8	114.2	4:14:57	44.8	171.5	4:11:14
6 (B–C)	30.5	116.8	4:20:20	48.3	185.1	4:19:18
7 (B–D)	27.0	103.3	4:19: 5	46.1	176.5	4:20:50
8 (B–E)	28.1	107.6	4:12:32	48.1	184.3	4: 9: 5
10 (C–D)	30.8	118.0	4:21: 5	49.8	190.8	4:19:47
11 (C–E)	31.4	120.2	4:13:34	51.5	197.1	4:11:57
13 (D–E)	-26.9	-102.9	4:41:29	18.9	72.6	3:58:53

Table 3.4: Results of the least squares fitting of the lag maximizing the coherence factors.

4 Estimation of Residual RMS Phase of Corrected Fringe Phase with the PAM

I will derive in this chapter a statistical model of the tropospheric phase fluctuations on the basis of the simple structural model of the upper troposphere. The model will be used to estimate the residual phase error left in the PAM observations. The validity of the model will be demonstrated by comparing the calculated results with the observed results. I will then discuss the feasibility of the future radio arrays using the statistical model.

4.1 Hypotheses of the Atmospheric Structure

In order to compare the results of our experments with the statistical theory on the propagation of radio waves in the turbulent troposphere, I use the simple statistical model based on the hypotheses of the Kolmogorov turbulence, phase screen, and frozen flow as described earlier [*Dravskikh and Finkelstein*, 1979]. Specifically, we assume that

1. the tropospheric turbulence is confined within an infinitely thin horizontal layer (phase screen) at a certain height h above the surface of the Earth,
2. the tropospheric excess path fluctuation can be well described by the SSF (spatial structure function) with the simple power law dependence on the spatial scale as predicted from the Kolmogorov turbulence theory, and
3. the spatial patterns of the fluctuation are moved horizontally by the wind of constant velocity $\boldsymbol{v}$ (frozen flow).

I will use this model to generate simulated series of the standard deviation of the differential fringe phase in PAM observations and compare them with those derived from our experiments.

4.2 Statistical Model for Standard Deviation of Differential Fringe Phase

4.2.1 Statistical Model for PAM Observations

Let us consider the contribution of the tropospheric phase noise in PAM observations as shown in Figure 2.2. The tropospheric fluctuations in the fringe phase difference $\Delta\Phi$ can be expressed as follows:

$$\Delta\Phi(t) = \Phi_A(t) - \Phi_B(t) = 2\pi\nu\{\tau_{air}(\boldsymbol{r}_2, t) - \tau_{air}(\boldsymbol{r}_1, t) - \tau_{air}(\boldsymbol{r}_4, t) + \tau_{air}(\boldsymbol{r}_3, t)\}, \quad (22)$$

where Φ_A and Φ_B are fringe phase fluctuations due to the tropospheric turbulence and

$\boldsymbol{r}_n$ is a position vector of the point at which the beam of n-th antenna crosses the phase screen. According to equation (7), the variance $\sigma^2_{\Delta\Phi}$ of the fringe phase difference is described as

$$\sigma^2_{\Delta\Phi} = \frac{1}{T^2}\int_0^T (T-t)\bar{D}_{\Delta\Phi}(t)dt, \tag{23}$$

where $\bar{D}_{\Delta\Phi}(t)$ is the TSF of the fringe phase difference:

$$\bar{D}_{\Delta\Phi}(t) = \langle\{\Delta\Phi(t'+t) - \Delta\Phi(t')\}^2\rangle. \tag{24}$$

From equation (22), we have

$$\begin{aligned}\bar{D}_{\Delta\Phi}(t) &= \bar{D}_\Phi(\boldsymbol{r}_3-\boldsymbol{r}_1,t) + \bar{D}_\Phi(\boldsymbol{r}_4-\boldsymbol{r}_2,t) + \bar{D}_\Phi(\boldsymbol{r}_2-\boldsymbol{r}_1,t) \\ &\quad +\bar{D}_\Phi(\boldsymbol{r}_4-\boldsymbol{r}_3,t) - \bar{D}_\Phi(\boldsymbol{r}_3-\boldsymbol{r}_2,t) - \bar{D}_\Phi(\boldsymbol{r}_4-\boldsymbol{r}_1,t).\end{aligned} \tag{25}$$

4.3 Computer Simulations of the PAM Observations Based on the Statistical Model

The simulated standard deviation $\sigma_{\Delta\Phi}$ based on equations (5), (10), (23), and (25) is compared with that derived from the PAM experiments.

4.3.1 PAM1

The parameters used in the simulation of PAM1 are listed in Table 4.1. The results of the simulation are given in Figure 3.5. The figure clearly shows general agreement between the theory and the experiments. The results demonstrate that the effective phase correction observed in our PAM experiments is reasonable from the theoretical point of view and that the validity of the PAM can be estimated by means of the theoretical model. This simulation also shows that the critical angular separation discussed in §3.2.3 is mostly affected by the height of the phase screen.

Of course, the agreement is not perfect, probably because

1. the elimination of the thermal noise contribution to the phase fluctuation in the estimation of the SSF and in the simulation is far from complete and tends to bias both α and C_l;

2. the real structure of the tropospheric turbulence must be more complicated than that assumed in the simplified phase screen model; and
3. the SSF was obtained from the nighttime observation of 3C 454.3 while the 3C 279–CS observation was carried out during daytime. Since it is well known that the height of the turbulent boundary layer is different between day and night, we might have adopted unsuitable parameters based on the nighttime SSF to the simulation of the daytime PAM experiments.

4.3.2 PAM2

In the case of PAM2, unlike in PAM1, I used the time series of the SSF parameters (the structure coefficient and exponent) estimated from the PAM2 data themselves on the basis of the multi-baseline fringe phase data of 3C 279 obtained by the NMA antennas (see §3.3.3). As mentioned in the discussion of the critical separation angle in Chapter 3, the time series of the standard deviation of the phase difference is sensitive to the horizontal distance between the beams of the paired antennas in the moist air, which means that in our statistical model the time series is sensitive to the distance between the crossing points of the beams on the phase screen. Therefore, they strongly depend on the height of the screen. Consequently, the height can be estimated by comparing the whole shape of the simulated time series with those obtained in the experiments. If the height is assumed too high/low, the shape of the simulated standard deviation becomes narrower/wider than the experimental results. As a result, I made a decision on the height of 1500 m.

The parameters used in the simulation are listed in Table 4.2, and the results of the computer simulation are drawn as the solid lines in Figure 3.12 along with the experimental results. The results of the computer simulation for PAM2 which adopts constant SSF parameters are also shown as dashed lines in Figure 3.12, which is useful to estimate the critical separation angle. The peaks at the time of the zero separation angle are not very sharp in the curves of the calculated standard deviations due to the time variation of the separation angle within the averaging time.

Figure 3.12 shows that the simulation results trace the experimental results much more finely than in PAM1, especially when the separation angle is smaller than several degrees. Note that the 146.81 GHz phase in PAM2 is almost one order of magnitude more sensitive to the excess path fluctuation than the 19.45 GHz phase in PAM1. The results clearly demonstrate that the hypotheses on the atmospheric structure are good enough at least for the spatial scale of the NMA and precise estimation for the rms phase error could be made by carefully choosing the suitable SSF parameters.

4.3.3 Effective Separation Angle in Millimeter- and Submillimeter-wave Interferometry

How well does the PAM work at millimeter or shorter wavelengths? Using the above statistical model, we can estimate an "effective separation" defined as the separation angle below which the standard deviation of the fringe phase difference is less than 1 rad. Let us consider a simple one-dimensional array configuration along the wind direction where $\boldsymbol{r}_3 - \boldsymbol{r}_1 = \boldsymbol{r}_4 - \boldsymbol{r}_2$ and $\boldsymbol{r}_3 - \boldsymbol{r}_1 \parallel \boldsymbol{r}_2 - \boldsymbol{r}_1 \parallel \boldsymbol{v}$. In this simplified case, equation (25) is reduced to

$$\bar{D}_{\Delta\Phi}(t) = 2\bar{D}_{\Phi}(d,t) - \bar{D}_{\Phi}(B+d,t) - \bar{D}_{\Phi}(B-d,t) + 2\bar{D}_{\Phi}(B,t), \tag{26}$$

where $B = \mid \boldsymbol{r}_2 - \boldsymbol{r}_1 \mid$ and $d = \mid \boldsymbol{r}_3 - \boldsymbol{r}_1 \mid$. If we assume that $B \gg d$ and $T \gg B/v$, equations (5), (11), (23), and (26) yield

$$\begin{aligned}
\sigma^2_{\Delta\Phi} &= \frac{1}{T^2}\int_0^T (T-t)\{2\bar{D}_{\Phi}(d,t) - \bar{D}_{\Phi}(B+d,t) - \bar{D}_{\Phi}(B-d,t) + 2\bar{D}_{\Phi}(B,t)\}dt \\
&\cong 2D(d) - D(B+d) - D(B-d) + 2D(B) \\
&\cong \frac{8\pi^2}{\lambda^2} C_l^2 \left\{ d^{\alpha} - \frac{\alpha(\alpha-1)}{3!} B^{\alpha-2} d^2 \right\}.
\end{aligned} \tag{27}$$

Since the second term in the right-hand side of equation (27) is much smaller than the first one by the assumption $B \gg d$ and $\alpha < 2$, we can simply neglect it. Assuming that the target and the reference sources are placed at elevation ϕ_{el} with azimuthal direction of their midpoint perpendicular to the baseline direction and that the separation angle θ is within a few degrees, we obtain

$$\sigma_{\Delta\Phi} \simeq \frac{2\sqrt{2}\pi}{\lambda} C_l \left(d_0 + \frac{h\theta}{\sin\phi_{el}} \right)^{\alpha/2}, \tag{28}$$

or

$$\sigma_{\Delta\Phi} \simeq qR_{\sigma} \left(d_0 + \frac{h\theta}{\sin\phi_{el}} \right)^{\alpha/2}, \tag{29}$$

where d_0 is the separation length between the close antennas, R_{σ} is a standard deviation

of the excess path length difference for 100-m baseline normalized by wavelength (e.g., $R_\sigma = 0.1$ when the differential excess path fluctuation for 100-m baseline is 0.1 mm and λ is 1 mm) and $q = 2\sqrt{2}\pi \times (100\text{m})^{-\alpha/2}$.

Let us assume tropospheric parameters of $v = 10$ m/s, $h = 1000$ m, $\alpha = 5/3$, and $C_l = 4.642 \times 10^{-6}$ cm$^{1/6}$ corresponding to the differential excess path fluctuation of 0.1 mm for 100-m baseline. These tropospheric values are typical for potential sites for future millimeter- and submillimeter-wave radio interferometric arrays (e.g., Mouna Kea in Hawaii [*Masson*, 1994]).

The effective correction for a case of $\phi_{el} = 50°$ and $d_0 = 20$ m is shown in Figure 4.1 as a function of baseline length and separation angle. This figure shows that the median of the effective separation curves is slightly offset from zero angular separation. The offset corresponds to the angle between two lines from each of the paired antennas crossing at the same point in the phase screen. Therefore the offset is equal to $d_0 \sin \phi_{el}/h$ from equation (29).

Figure 4.1 shows that the PAM is a promising technique to compensate the tropospheric phase errors. Where wavelength is greater than 0.38 mm (frequency of 800 GHz or less), the PAM work well where there is an adjacent reference source within the separation angle less than 2° as shown in Figure 4.1. *Foster* [1994] showed in his Monte Carlo simulations based on 90-GHz source counts [*Holdaway et al.*, 1994] that there would be a reference source with a flux density of at least 0.1×10^{-26} Wm^{-2}Hz^{-1} at millimeter-wave within 2° of a random point on the sky. Even in the submillimeter range, the PAM will work if observing sites have good enough conditions with the differential excess path fluctuation for 100-m baseline of 0.1 mm or better and if there are strong enough reference sources within a few degrees of a target source.

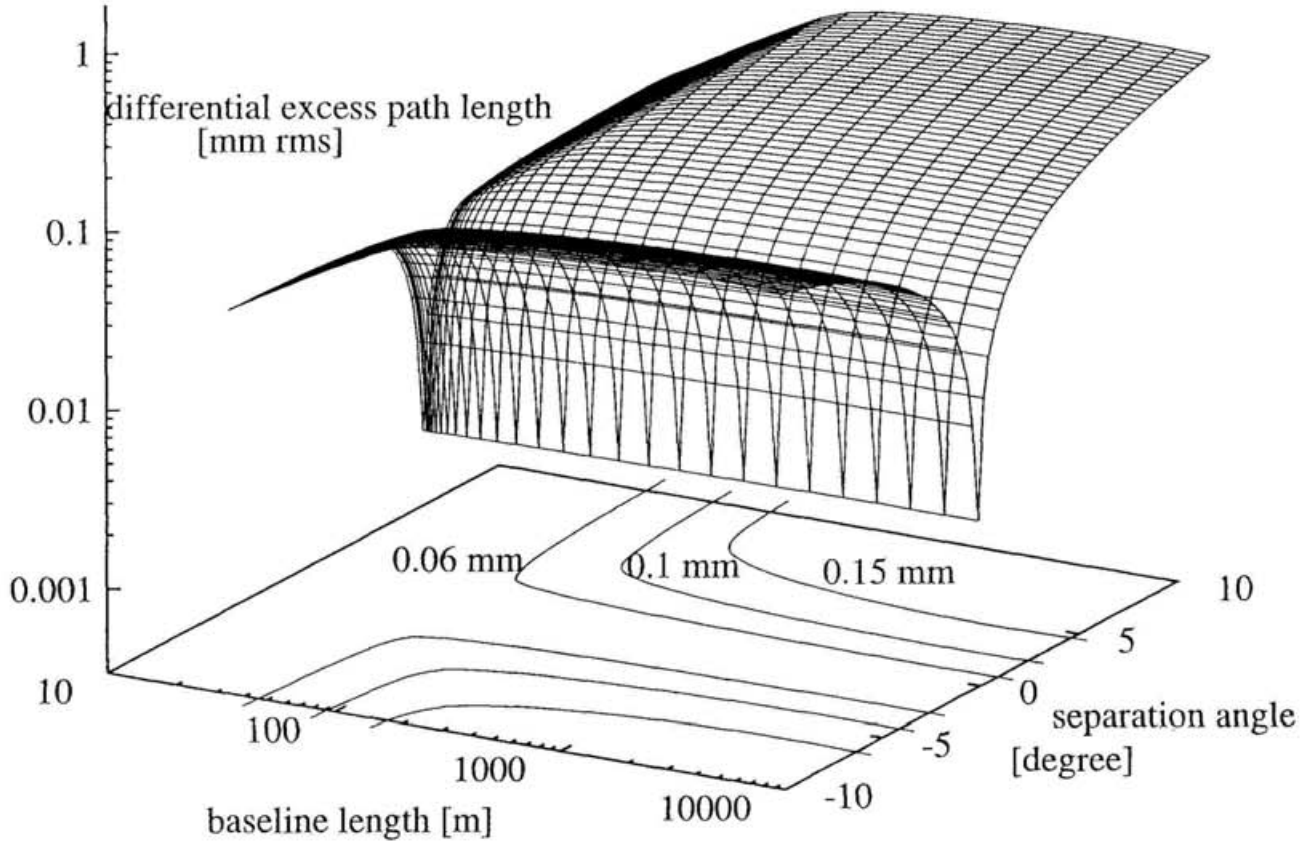

Figure 4.1: Result of the simulation at potential sites for future millimeter- or submillimeter-wave radio arrays with the PAM. Each of the contour levels on the base represents the degree of phase compensation of 0.06, 0.1, and 0.15 mm rms in excess path length.

scale height	1000 m
integration duration	500 sec
wind velocity	9 m/s
wind direction	west to east
C_l (SSF)	3.90×10^{-5} cm$^{1-\alpha/2}$
α (SSF)	1.564
$D^{\frac{1}{2}}_{100m}$	0.52 mm

Table 4.1: Parameters adopted in the simulation based on our model of PAM1.

	exp0128	exp0129
scale height	1500 m	1500 m
integration duration	1000 sec	1000 sec
wind velocity	18 m/s	11 m/s
wind direction	west to east	west to east
C_l (for constant SSF)	0.665×10^{-5} cm$^{1-\alpha/2}$	0.574×10^{-5} cm$^{1-\alpha/2}$
α (for constant SSF)	1.667	1.667
$D^{\frac{1}{2}}_{100m}$ (for constant SSF)	0.175 mm	0.151 mm

Table 4.2: Parameters adopted in the simulation based on our model of PAM2. The SSF values in the list are averaged ones.

scale height	1000 m
integration duration	1000 sec
C_l (SSF)	4.642×10^{-6} cm$^{1/6}$
α (SSF)	1.667
$D^{\frac{1}{2}}_{100m}$	0.1 mm
wind velocity	10 m/s
wind direction	west to east

Table 4.3: Parameters adopted in the simulation based on our model for future millimeter- or submillimeter-wave radio arrays.

5 Phase Compensation with the Antenna-Switching Method

The antenna-switching method is similar to the PAM in the sense that the switching method also uses reference sources in the vicinity of a target source. The VLBI experiments using this method have been conducted between quasars [e.g., *Shapiro* et al., 1979] or a quasar and a galactic source [e.g., *Gwinn* et al., 1986] with a typical period of the switching cycle of several minutes and successfully measured the angular distances between the radio sources with a typical accuracy of a few hundreds of micro arcsec.

Although the phase compensation experiments adopting the antenna-switching method have not been carried out with the NMA and the NRSM, the atmospheric model discussed in Chapter 4 can be applied to examine the performance of the phase compensation methods other than the PAM. Here, I consider the antenna-switching method which might be a simple and possibly inexpensive way to achieve the phase compensation comparable with the one obtained with the PAM.

5.1 Statistical Model for the Antenna-Switching Method

First, I will derive the statistical model of the antenna-switching method on the basis of the hypotheses on the upper troposphere as discussed in Chapter 4. Let us consider difference between fringe phases of a target source A and that of the reference source B at time t. In actuality, only one source (the target A, say) is observed at the time t in the switching observations. For the fringe phase Φ_B of the reference source at t, we use a simple interpolation of the fringe phase $\{\Phi_B(t+T_{cyc}/2)+\Phi_B(t-T_{cyc}/2)\}/2$, where T_{cyc} stands for the period of a switching cycle including the antenna slewing and the observations. Then, the tropospheric phase fluctuations $\Delta\Phi_S$ left after the phase compensation is expressed using the frozen flow hypothesis as shown in Figure 5.1:

$$\begin{aligned}
\Delta\Phi_S(t) &= \Phi_A(t) - \frac{1}{2}\{\Phi_B(t+T_{cyc}/2)+\Phi_B(t-T_{cyc}/2)\} \\
&= 2\pi\nu[\tau_{air}(\boldsymbol{r}_2,t)-\tau_{air}(\boldsymbol{r}_1,t) \\
&\quad -\frac{1}{2}\{\tau_{air}(\boldsymbol{r}_2+\boldsymbol{\delta},t+T_{cyc}/2)-\tau_{air}(\boldsymbol{r}_1+\boldsymbol{\delta},t+T_{cyc}/2) \\
&\quad +\tau_{air}(\boldsymbol{r}_2+\boldsymbol{\delta},t-T_{cyc}/2)-\tau_{air}(\boldsymbol{r}_1+\boldsymbol{\delta},t-T_{cyc}/2)\}], \qquad (30)
\end{aligned}$$

where $\boldsymbol{\delta}$ is the difference between the position vectors on the target and reference sources on the phase screen as shown in Figure 5.1. $\bar{D}_{\Delta\Phi_S}(t)$ in the above expression stands for

the TSF of the fringe phase difference:

$$\bar{D}_{\Delta\Phi_S}(t) = \langle[\Phi_A(t'+t) - \frac{1}{2}\{\Phi_B(t'+t+T_{cyc}/2) + \Phi_B(t'+t-T_{cyc}/2)\}$$

$$-\Phi_A(t') + \frac{1}{2}\{\Phi_B(t'+T_{cyc}/2) + \Phi_B(t'-T_{cyc}/2)\}]^2\rangle. \quad (31)$$

We can derive the following equation from equation (31):

$$\bar{D}_{\Delta\Phi_S}(t) = \frac{1}{4}[6\bar{D}_{\Delta\Phi}(\boldsymbol{B},t) + \bar{D}_{\Delta\Phi}(\boldsymbol{B}+\boldsymbol{v}T_{cyc}/2,t) + \bar{D}_{\Delta\Phi}(\boldsymbol{B}-\boldsymbol{v}T_{cyc}/2,t)$$

$$+4\bar{D}_{\Delta\Phi}(\boldsymbol{\delta}+\boldsymbol{v}T_{cyc}/2,t) + 4\bar{D}_{\Delta\Phi}(\boldsymbol{\delta}-\boldsymbol{v}T_{cyc}/2,t)$$

$$-2\bar{D}_{\Delta\Phi}(\boldsymbol{B}+\boldsymbol{\delta}+\boldsymbol{v}T_{cyc}/2,t) - 2\bar{D}_{\Delta\Phi}(\boldsymbol{B}-\boldsymbol{\delta}+\boldsymbol{v}T_{cyc}/2,t)$$

$$-2\bar{D}_{\Delta\Phi}(\boldsymbol{B}+\boldsymbol{\delta}-\boldsymbol{v}T_{cyc}/2,t) - 2\bar{D}_{\Delta\Phi}(\boldsymbol{B}-\boldsymbol{\delta}-\boldsymbol{v}T_{cyc}/2,t)$$

$$-2\bar{D}_{\Delta\Phi}(\boldsymbol{v}T_{cyc},t)]. \quad (32)$$

Hence, the variance $\sigma^2_{\Delta\Phi_S}$ of the fringe phase difference is described as

$$\sigma^2_{\Delta\Phi_S} = \frac{1}{T^2}\int_0^T (T-t)\bar{D}_{\Delta\Phi_S}(t)dt, \quad (33)$$

where we used equations (7) and (32). Equation (33) shows the rms value of the fluctuations left in the phase difference where the target source is continuously observed for whole observing time together with the reference source. Note that, where $T_{cyc} = 0$, equation (33) is reduced to the equation of the PAM observations with no separation between paired antennas (such a system could be made by using a kind of multi-beam antennas).

In the antenna-switching observations as shown in Figure 5.1, the integration time for a source is limited because of the mutual observations between the target and reference sources. In such a case, the rms phase of the calibrated phase $\sigma^2_{\Delta\Phi_S}$ is expressed from equation (7) by

$$\sigma^2_{\Delta\Phi_S} = \langle\frac{1}{NT_o}\int_0^T [\Delta\Phi_S(t)u(t) - \frac{1}{NT_o}\int_0^T \Delta\Phi_S(t')u(t')dt']^2 dt\rangle, \quad (34)$$

where $N = T/T_{cyc}$, $u(t)$ is a step function which is 1 when $nT_{cyc} < t < nT_{cyc} + T_o$ $(n = 0, 1, 2, ..., N-1)$ and 0 otherwise, and T_o is a period of the observation of the target source within one switching cycle and referred to as ON source time. The above equation is then expressed, with the TSF $\bar{D}_{\Delta\Phi}$, by

$$\sigma^2_{\Delta\Phi_S} = \frac{1}{2(NT_o)^2} \sum_{n=0}^{N-1} \sum_{m=0}^{N-1} \int_{t=nT_s}^{t=nT_s+T_o} \int_{\tau=t-mT_s-T_o}^{\tau=t-mT_s} \bar{D}_{\Delta\Phi}(\tau) d\tau dt. \quad (35)$$

Finally, we can obtain the following equation for the antenna-switching phase calibration:

$$\sigma^2_{\Delta\Phi_S} = \frac{1}{(NT_o)^2} \int_0^{T_o} (T-\tau) \{ \sum_{n=0}^{N-1} (N-n) [\bar{D}_{\Delta\Phi_S}(nT_{cyc}-\tau) + \bar{D}_{\Delta\Phi_S}(nT_{cyc}+\tau)] - N\bar{D}_{\Delta\Phi_S}(\tau) \} d\tau. \quad (36)$$

For large enough T, the results of the numerical calculation with equation (36) turn out to be almost the same as those with equation (33). The fact implies that the rms phase of the calibrated phase by the antenna-switching method is almost independent of the ratio of the observing time to the switching cycle time.

5.2 Computer Simulations of Antenna-Switching Observations Based on the Statistical Model with the PAM2 Data

The performance of the antenna-switching method is studied based on the demonstrated data produced from the PAM2 data. I examined a particular case of the switching with 10-s slew, 10-s observation of the target (3C 279), 10-s slew again and 10-s observation of the reference (CS). The switching cycle time T_{cyc} is therefore 40 s. The time series thus produced from the fringe phases of the two sources are shown in Figure 5.2 along with their difference. The parameters adopted for the statistical calculation are the same as those used for the calculation of the PAM2 experiments and are listed in Table 4.2. The simulation results are also shown in Figure 5.2. The solid lines show the simulation results with the time-variable SSF parameters estimated in the course of the experiments, while the dashed lines show the simulation results with the fixed mean SSF parameters. Figure 5.2 shows fairly good agreement between the results obtained from the produced time series and the results of the computer simulation (solid lines). This implies that the statistical model for the antenna-switching observations is a good approximation of the reality.

It is interesting to note that the time when the rms differential phase error takes the minimum in both calculated and simulated time series does not match the time of the

minimum separation angle. It must be noted also that all the dashed lines in Figure 5.2 exhibit an interesting shape with double minimum peaks at the separation angle around $\pm 10°$. This can be easily understood in terms of the frozen flow hypothesis. In fact, spatial pattern of the fluctuation must move by a certain distance $\mid \boldsymbol{\delta} \mid$ for the switching time $T_{cyc}/2$ from the reference source to the target source. Therefore, if the separation of the two sources on the phase screen is equal to the above distance, the switching antenna sees the same block of the wet troposphere before and after the switching and gets the maximum effect of the compensation, provided, of course, the wind direction happens to coincide with the direction of the separation of the two sources as in the PAM2 experiments. As a matter of fact, $\mid \boldsymbol{\delta} \mid = h/\sin\phi_{el} \times \tan\theta$ is 355 m for the height of the phase screen of 1500 m, which does match the displacement of the spatial pattern $v \times T_{cyc}/2$ of 358 m, if we assume that $\boldsymbol{\delta}$ is parallel to $\boldsymbol{v}$.

Compared with the results of the PAM in Figure 3.12, the 40-s antenna-switching phase compensation cannot achieve the level of 0.06 mm rms which is the required goal of the phase compensation for the future submillimeter interferometer arrays. It is expected that the shorter the switching cycle period the better the effectiveness of the phase compensation will be. On the other hand, when the switching cycle time becomes shorter, the observing time will be more severely limited because the antenna slew and setting time will require a large part of the observing time. In order to evaluate the feasibility of the phase compensation with the antenna-switching method, it is necessary to investigate these specific parameters.

5.3 Switching Cycle Time and ON Source Time Ratio of the Antenna-Switching Method

The switching cycle time and a ratio of the ON source time to the switching cycle time (ON source time ratio) are important parameters in the antenna-switching method. Relations between the parameters and the rms phase difference are investigated using the CS fringe phase data obtained in the PAM2. The CS data is divided into two time series to demonstrate switching observations of a pair of sources with 0° separation. Fringe phases of the 'target' and 'reference' data are averaged for each ON source time, and phase difference is made by subtracting the reference fringe phase, which is the interpolated value of the reference phases of the observations sandwiching a target observation, from a target fringe phase. The rms phase of the phase difference is calculated with the integration time of 1000 s centered on the reference time.

5.3.1 Switching Cycle Time

In the following demonstration, the antenna slew time is set to be equal to the ON source time, so that the ON source time ratio is 0.25. The demonstration results are shown in Figure 5.3(a) and (b) for exp0128, and (c) and (d) for exp0129 with the

simulation results calculated with equation (36) adopting the SSF determined in § 3.3.3. The simulation results are in good agreement with the rms phase from the demonstrated time series. The standard deviations gradually increase with the increasing switching cycle until a certain switching cycle time. This switching cycle time is considered as a critical value beyond which the antenna-switching method does not meaningfully improve the degree of phase compensation. The critical switching cycle time is roughly determined by $2B/v$, where B is the baseline under the assumption of the frozen flow.

5.3.2 ON Source Time Ratio

The rms phase difference is shown as functions of the ON source time ratio in Figure 5.4(a) and (b) for exp0128, and (c) and (d) for exp0129. The rms phase in all the drawings of Figure 5.4 is almost independent of the ratio, which proves the prediction in § 5.1. This allows us to determine the ON source time ratio arbitrarily for the purpose of the compensation of the atmospheric phase fluctuations. For example, one can choose a large ON source time ratio in order to get larger signal-to-noise ratio for a relatively weak source.

5.4 Estimation of Residual RMS Phase of Corrected Fringe Phase with the Antenna-Switching Method

The effectiveness of the phase compensation with the antenna-switching method was calculated assuming the same parameters as those described in §4.3.3. The rms differential phase is shown in Figure 5.5 as a function of the baseline length and the source separation angle. The switching cycle time is set to 20 s. The double minimum peaks of the standard deviation again appear at the separation angle of $\pm 8.5°$ at which $\mid \boldsymbol{\delta} \mid \simeq \mid \boldsymbol{v} \times T_{cyc}/2 \mid \simeq$ 200 m. The figure shows that it is difficult to achieve the 0.06 mm rms level phase compensation required for the future submillimeter interferometry by means of the 20-s antenna-switching for a baseline longer than 200 m even in the condition of the best available sites in the world with the SSF parameter of 0.1 mm rms per 100 m.

The performance of the antenna-switching method is improved if we can switch the antennas with faster speed. Figure 5.6 shows the relation between the degree of phase compensation and the switching cycle time for the condition above and baseline length of 1000 m for the various separation angle. This figure also shows the degree of phase compensation with the PAM, whose configuration is almost the same with the one discussed in §4.3.3 but the direction between the close antennas is normal to the baseline so that the offset of the effective separation does not happen in this estimation. From this figure, we can see that the antenna-switching method will achieve the same or higher degree of phase compensation rather than the PAM with 20-m antenna separation in observing a pair of sources with 2°-separation, if the switching cycle time is shorter than 16 s. Observation of 4 s for each of the sources and 4-s slew could be an example. Such a fast switching is fully

achievable for millimeter-wave radio telescope antennas with diameter of a few tens of meters with well-designed digital servo-control systems [*K.M.Shibata* et al., 1994]. Therefore, the fast antenna-switching method is the very useful phase compensation technique to remove the atmospheric phase fluctuations.

5.5 Comparison between the PAM and the Antenna-Switching Method

It has been clarified in this chapter that the antenna-switching phase compensation has an ability comparable to the PAM if the antennas can be slewed fast enough. In addition, the antenna-switching method has the simplest configuration in the proposed phase compensation techniques. The PAM is constructed of multi antennas at each stations, which generates a dead angle to observe: closer the paired antennas are to remove the atmospheric phase fluctuations, wider the dead angle is. The way of more successful phase compensation in the antenna-switching method is to switch antennas as quickly as possible. Since radio telescope antennas can be built to satisfy the requirement of the switching cycle time of 20 s for a pair of sources separated by a few degrees, the antenna-switching method will be a very hopeful technique to compensate the atmospheric phase fluctuations.

On the other hand, an important merit of the PAM compared with the antenna-switching method is to observe a target source for whole observing time, which makes the sensitivity of interferometer higher because signal-to-noise ratio becomes higher according to square root of the total integration time without the serious coherence loss. Although the integration for a long time interval can be achieved in the antenna-switching method, the amount of the duration is limited because the slew time occupies the large fraction in the switching cycle period. The PAM will be the more vital tool for the phase compensation for very weak radio sources.

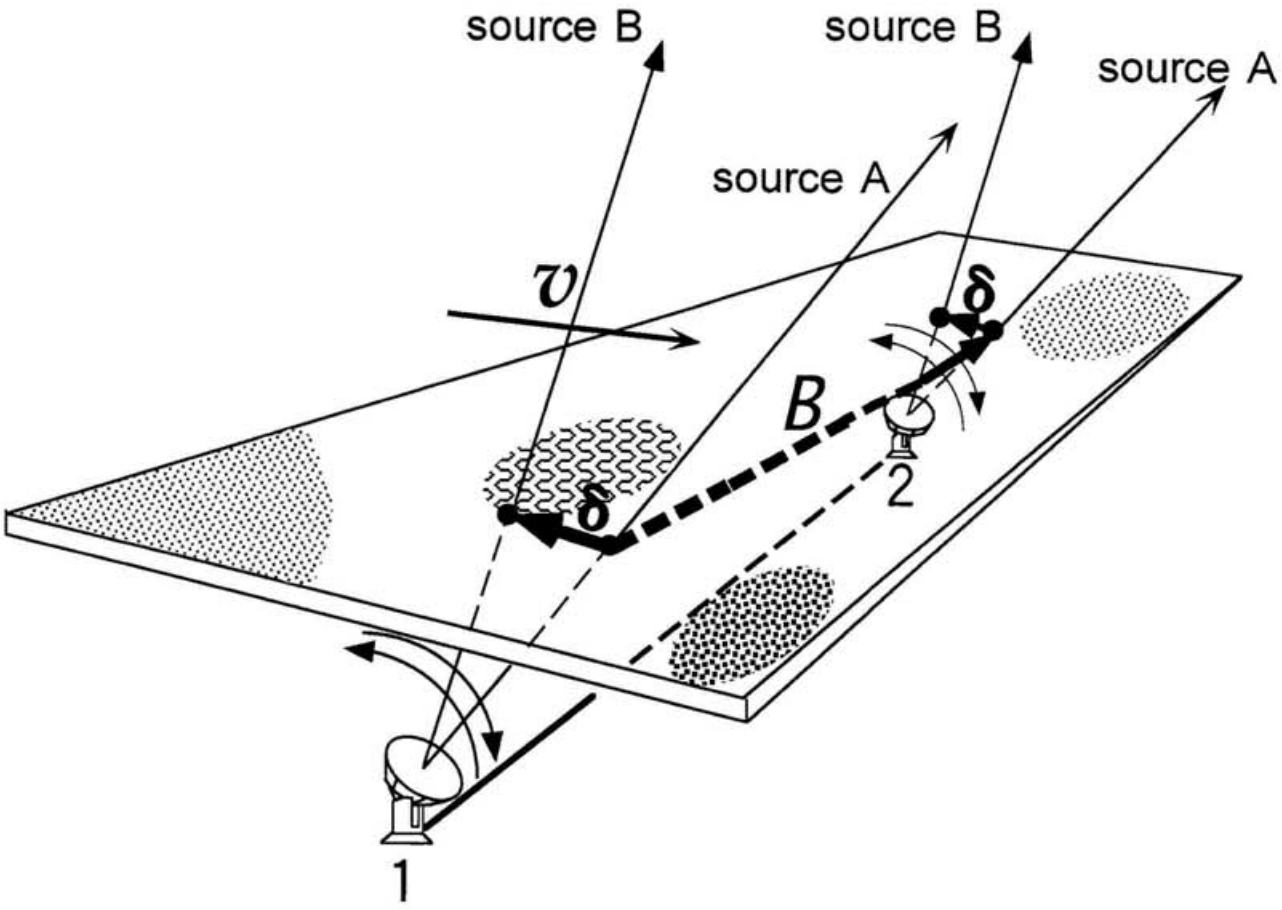

Figure 5.1: Configuration of phase-referencing observations with the antenna-switching method.

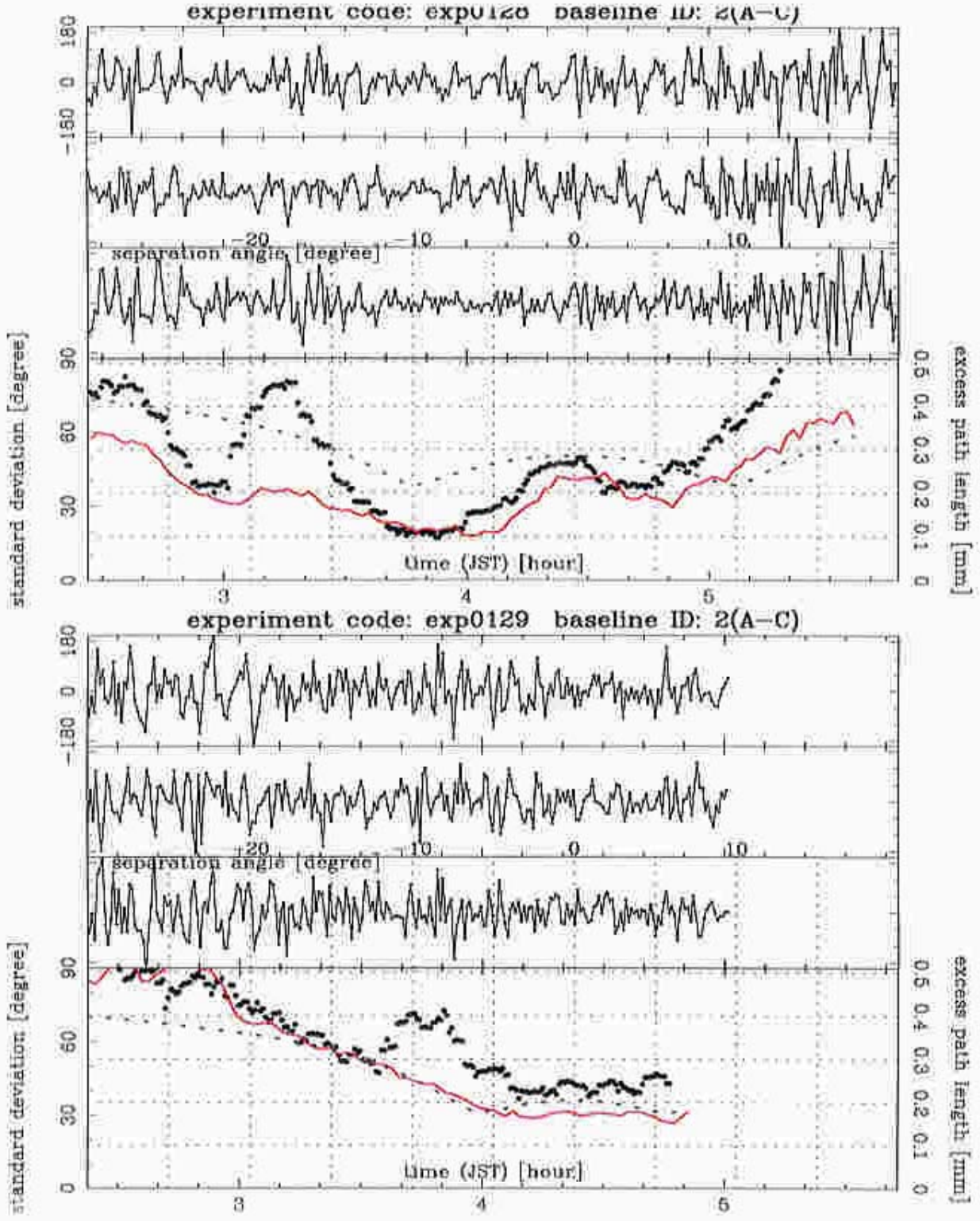

Figure 5.2 (a): Demonstrated time series of the antenna-switching method produced from the PAM2 data, baseline 2 (A–C) of exp0128 and exp0129 in the first and bottom four drawings, respectively, for the case of 10-s observations for both the target and reference sources and 10-s slew twice in one switching cycle. Each of the upper three drawings shows the time series of 3C 279, Japanese Communication Satellite, and their difference. The last drawing shows the standard deviations of the difference calculated with the integration interval of 1000 s (closed circles). The solid and dashed lines show the simulation results adopting the time-variable and constant spatial structure function, respectively.

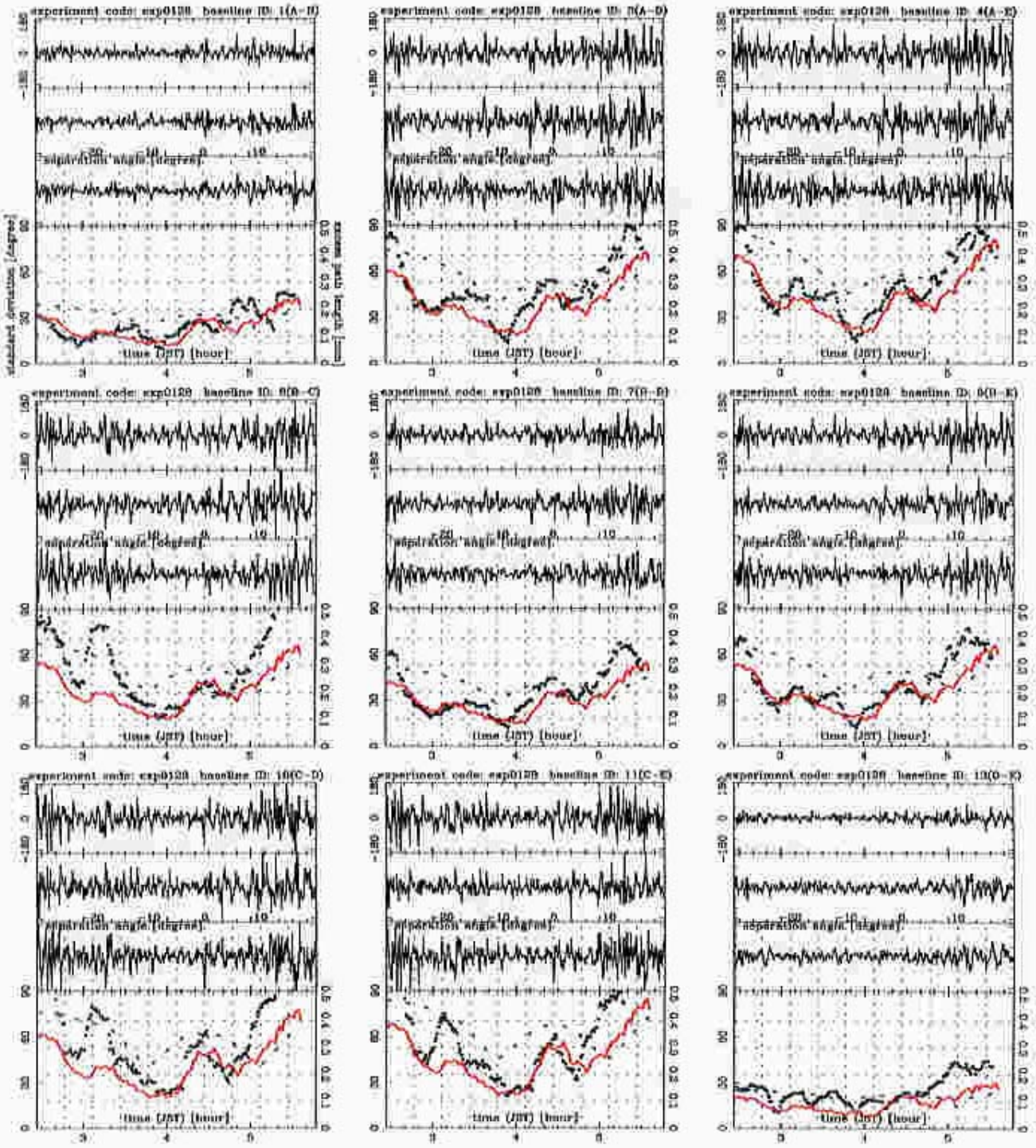

Figure 5.2 (b): Demonstrated time series of the antenna-switching method produced from the PAM2 data of exp0128.

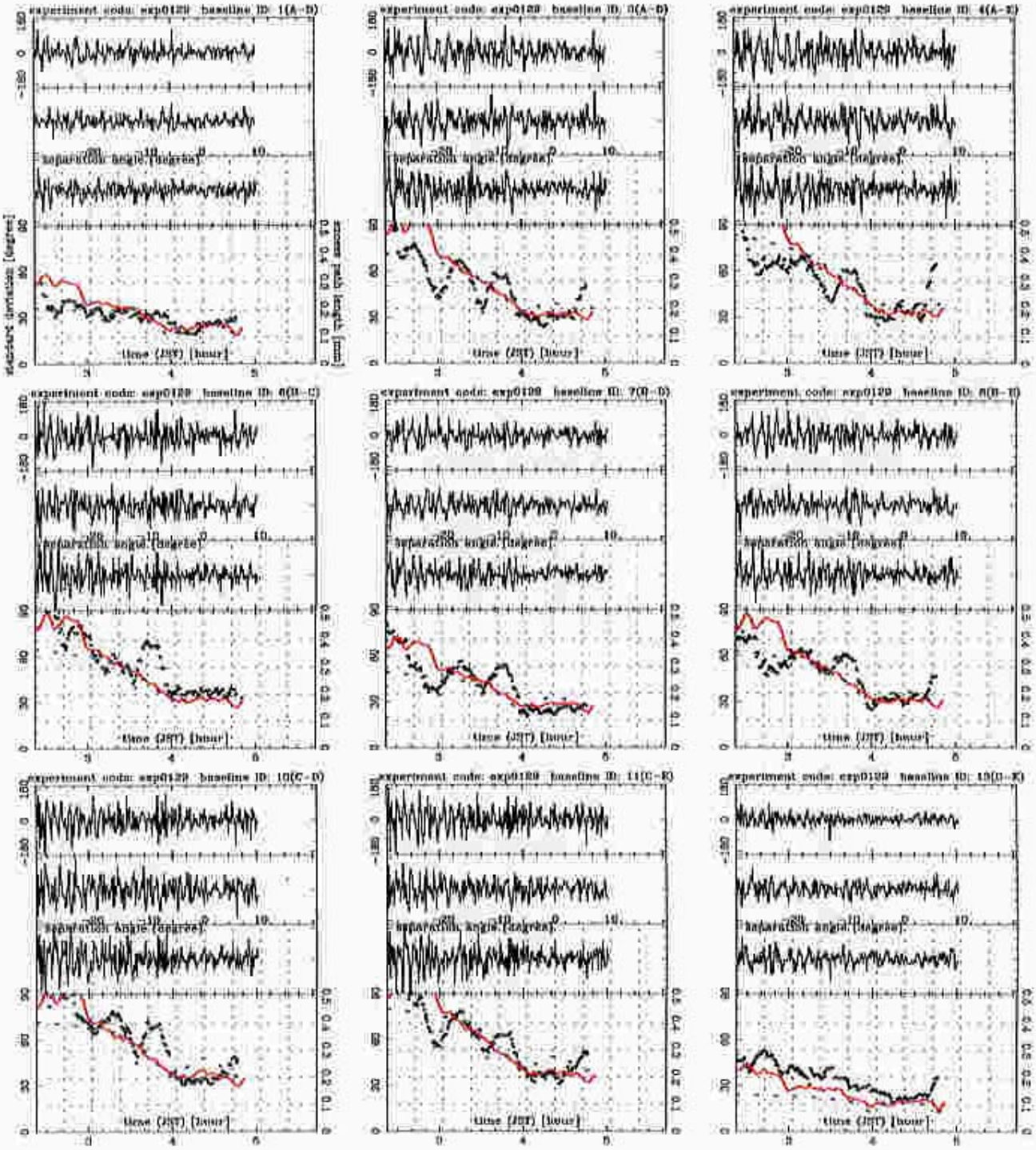

Figure 5.2 (c): Demonstrated time series of the antenna-switching method produced from the PAM2 data of exp0129.

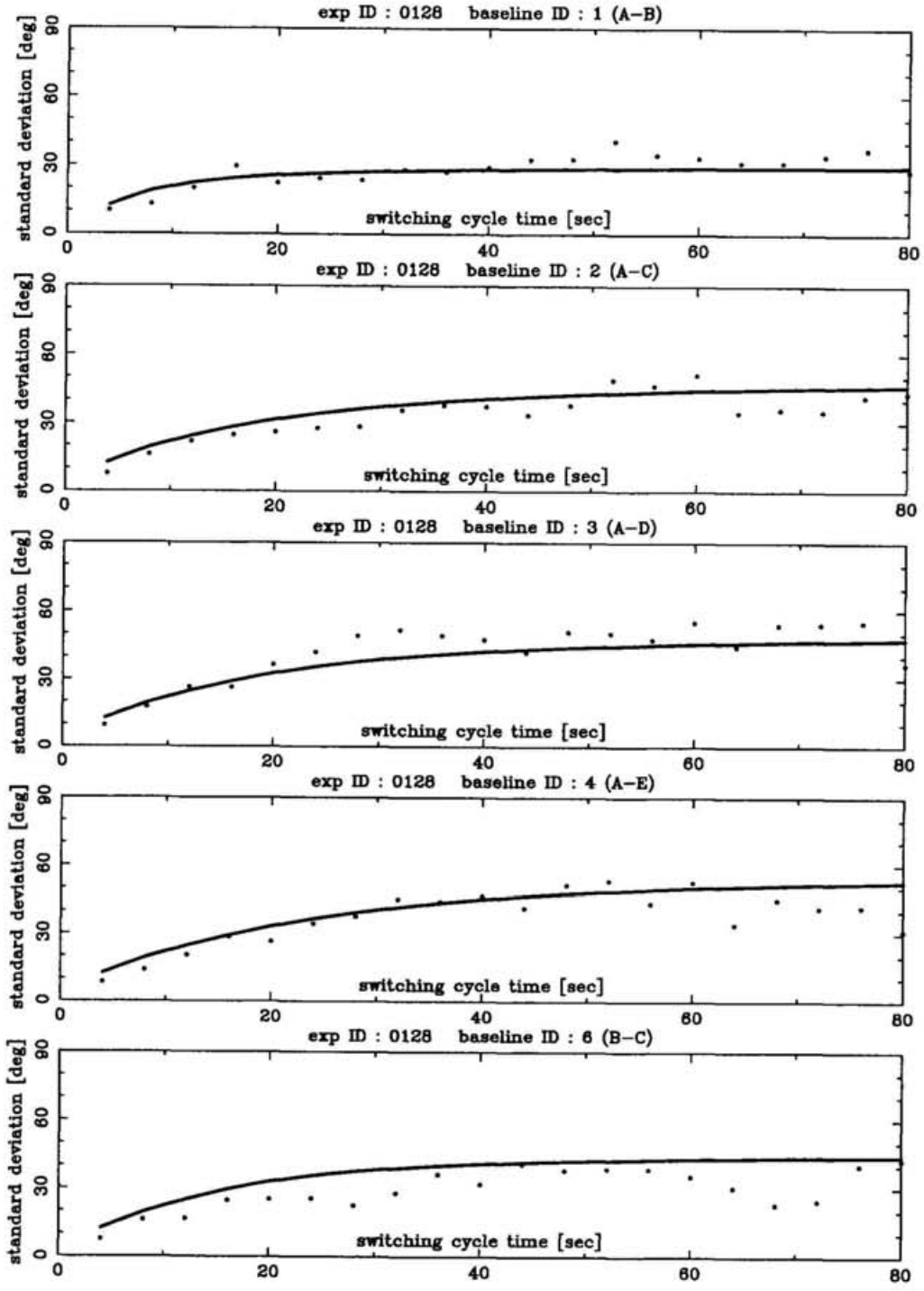

Figure 5.3 (a): Rms phases of the demonstrated phase difference related to the switching cycle time of the antenna-switching method. Closed circles show the standard deviations of the demonstrated phase difference with the integration time of 1000 s. Solid lines show the simulated results of the demonstration. Each drawing shows baseline 1 (A–B), baseline 2 (A–C), baseline 3 (A–D), baseline 4 (A–E), and baseline 6 (B–C) of exp0128.

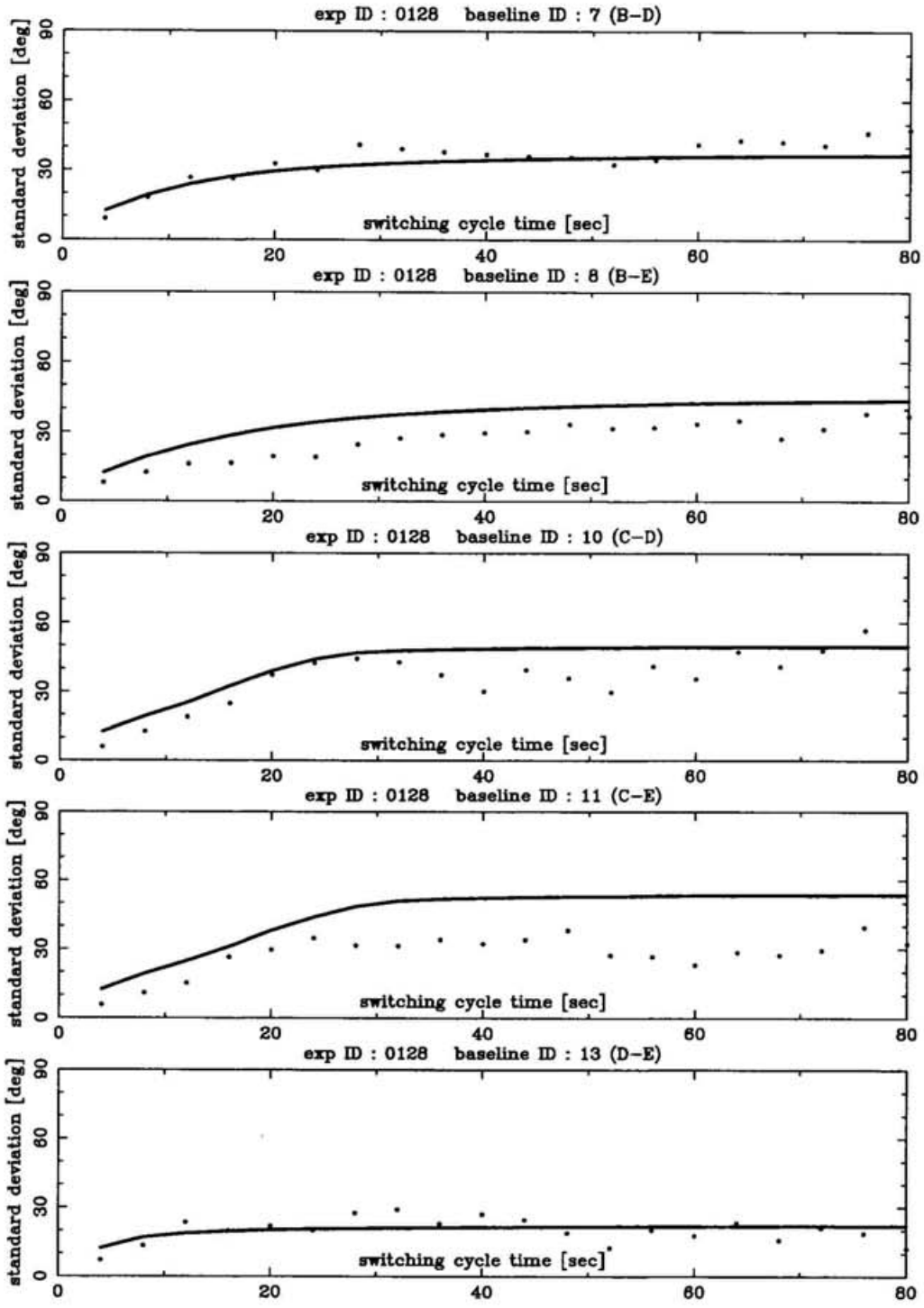

Figure 5.3 (b): Rms phases of the demonstrated phase difference related to the switching cycle time. Each drawing shows baseline 7 (B–D), baseline 8 (B–E), baseline 10 (C–D), baseline 11 (C–E), and baseline 13 (D–E) of exp0128.

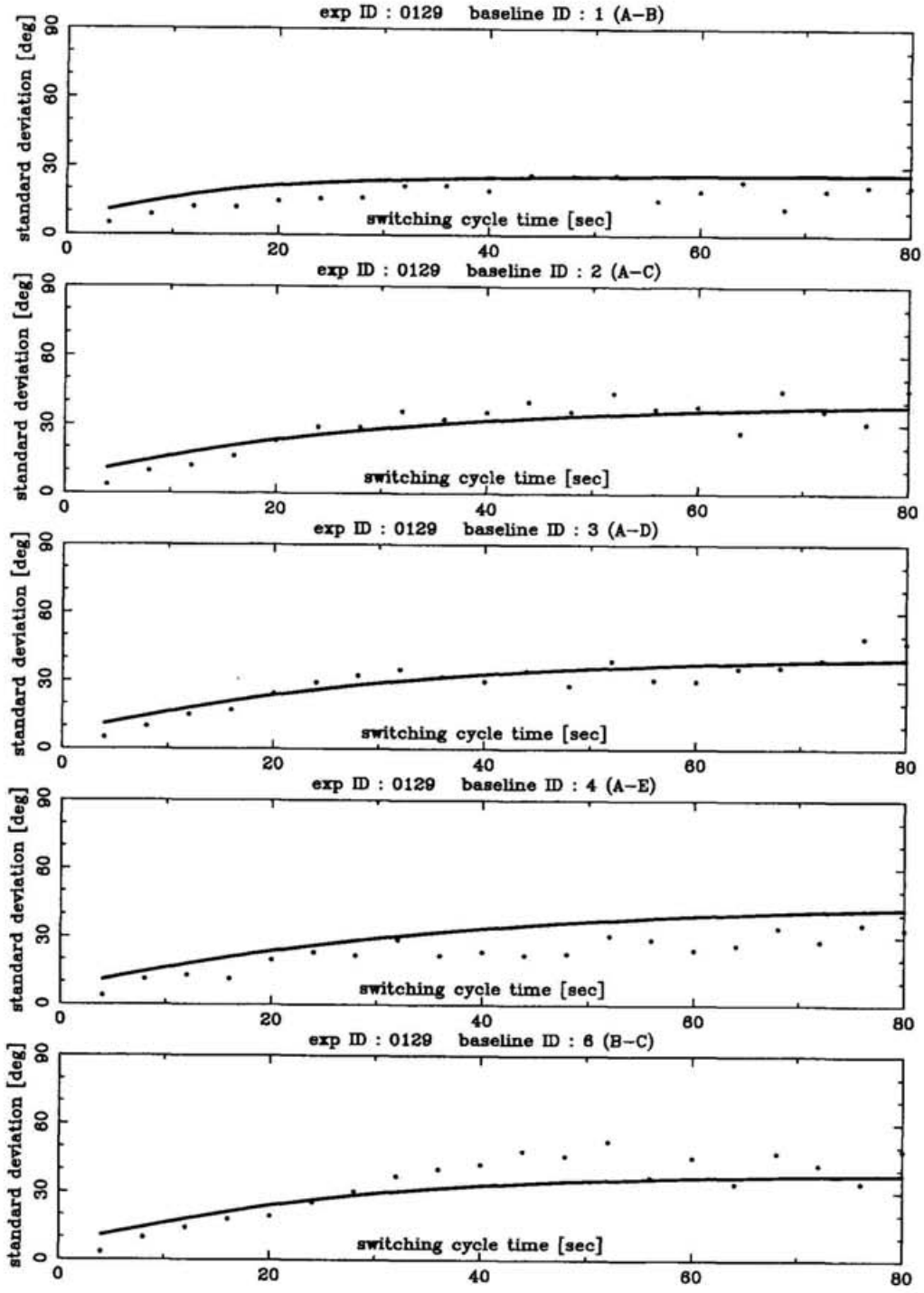

Figure 5.3 (c): Rms phases of the demonstrated phase difference related to the switching cycle time. Each drawing shows baseline 1 (A–B), baseline 2 (A–C), baseline 3 (A–D), baseline 4 (A–E), and baseline 6 (B–C) of exp0129.

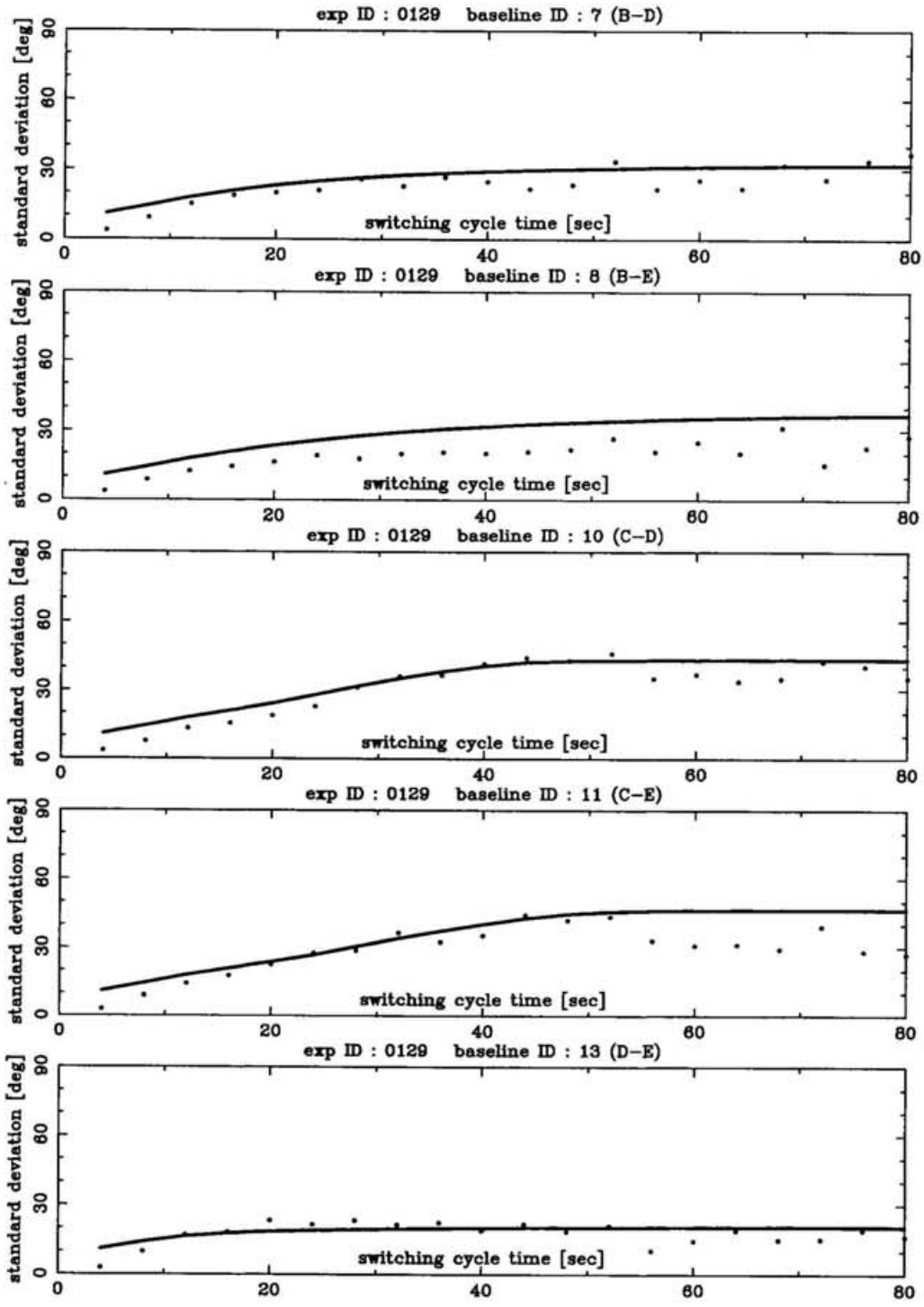

Figure 5.3 (d): Rms phases of the demonstrated phase difference related to the switching cycle time. Each drawing shows baseline 7 (B–D), baseline 8 (B–E), baseline 10 (C–D), baseline 11 (C–E), and baseline 13 (D–E) of exp0129.

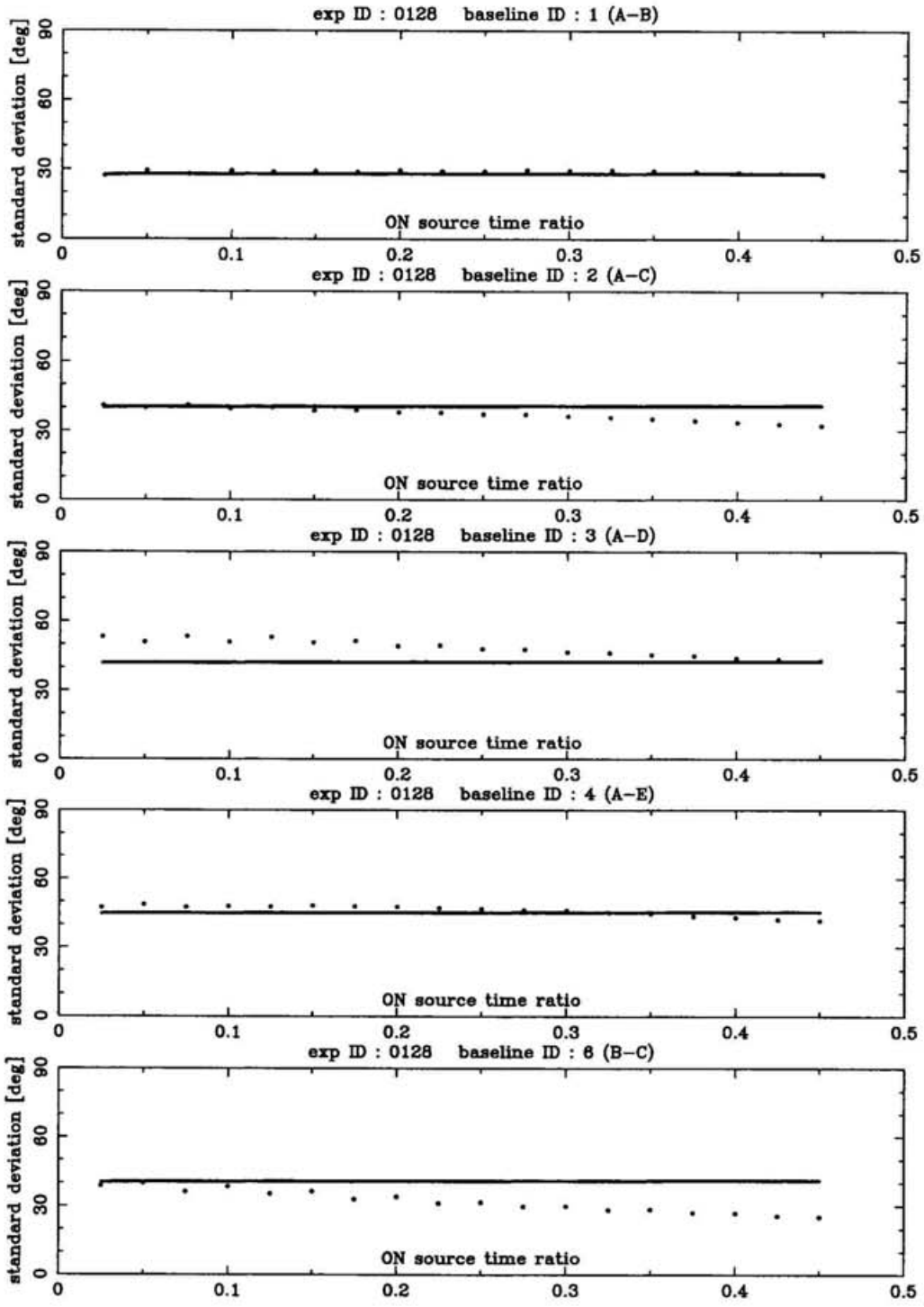

Figure 5.4 (a): Rms phases of the demonstrated phase difference related to the ON source time ratio of the antenna-switching method. Closed circles shows the standard deviations of the demonstrated phase differences with the integration interval of 1000 s. Each drawing shows baseline 1 (A–B), baseline 2 (A–C), baseline 3 (A–D), baseline 4 (A–E), and baseline 6 (B–C) of exp0128.

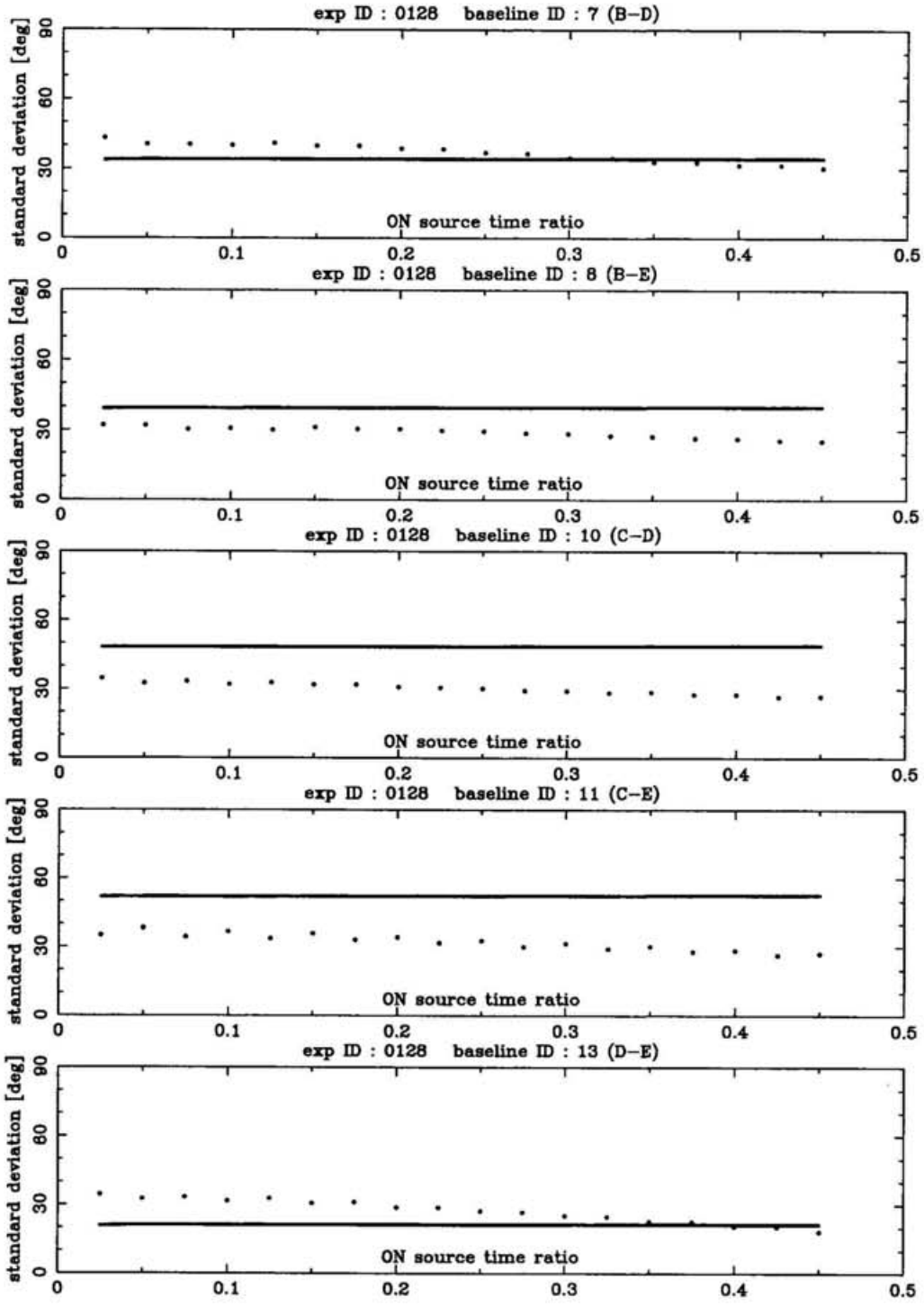

Figure 5.4 (b): Rms phases of the demonstrated phase difference related to the ON source time ratio of the antenna-switching method. Each drawing shows baseline 7 (B–D), baseline 8 (B–E), baseline 10 (C–D), baseline 11 (C–E), and baseline 13 (D–E) of exp0128.

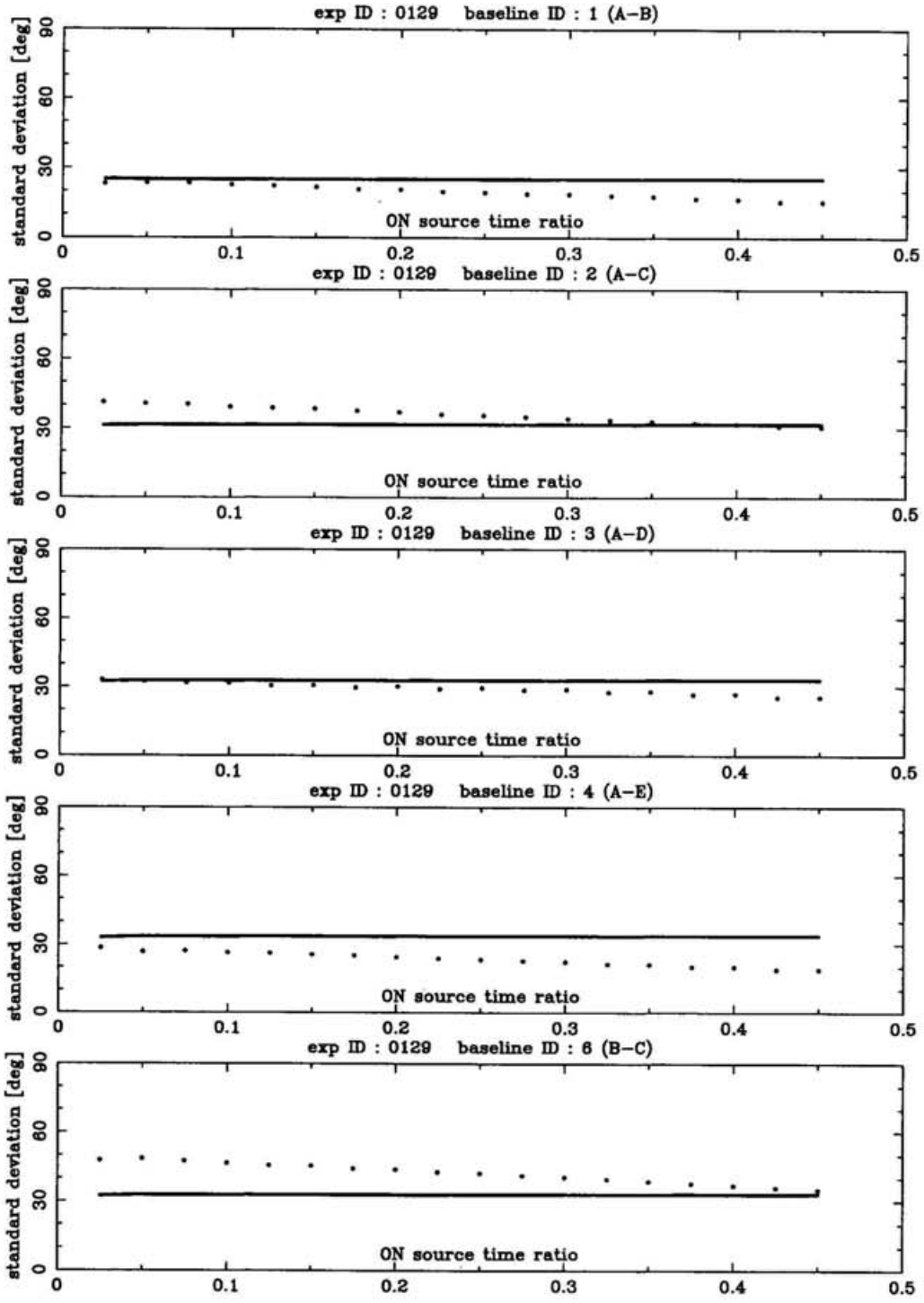

Figure 5.4 (c): Rms phases of the demonstrated phase difference related to the ON source time ratio of the antenna-switching method. Each drawing shows baseline 1 (A–B), baseline 2 (A–C), baseline 3 (A–D), baseline 4 (A–E), and baseline 6 (B–C) of exp0129.

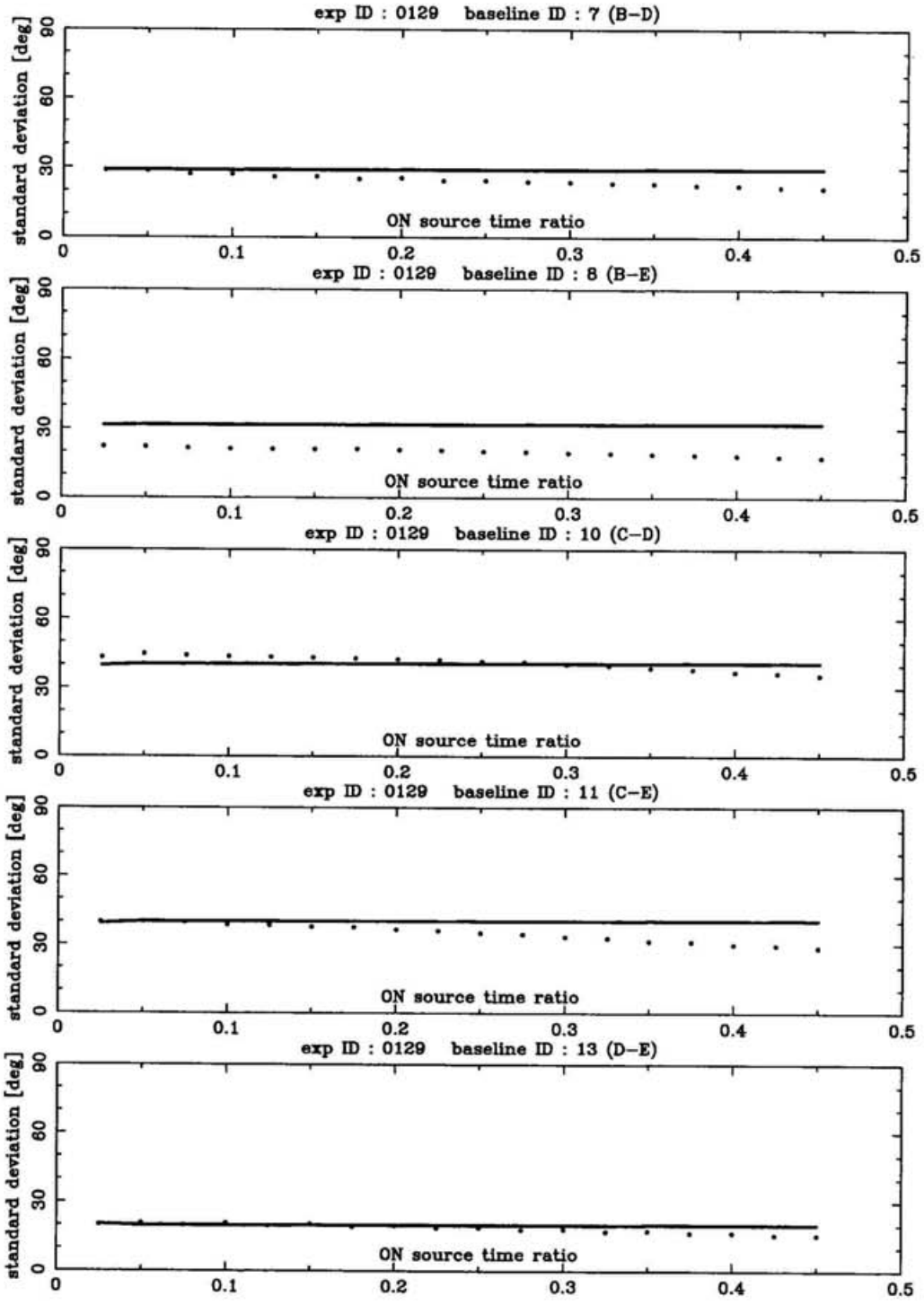

Figure 5.4 (d): Rms phases of the demonstrated phase difference related to the ON source time ratio of the antenna-switching method. Each drawing shows Baseline 7 (B–D), baseline 8 (B–E), baseline 10 (C–D), baseline 11 (C–E), and baseline 13 (D–E) of exp0129.

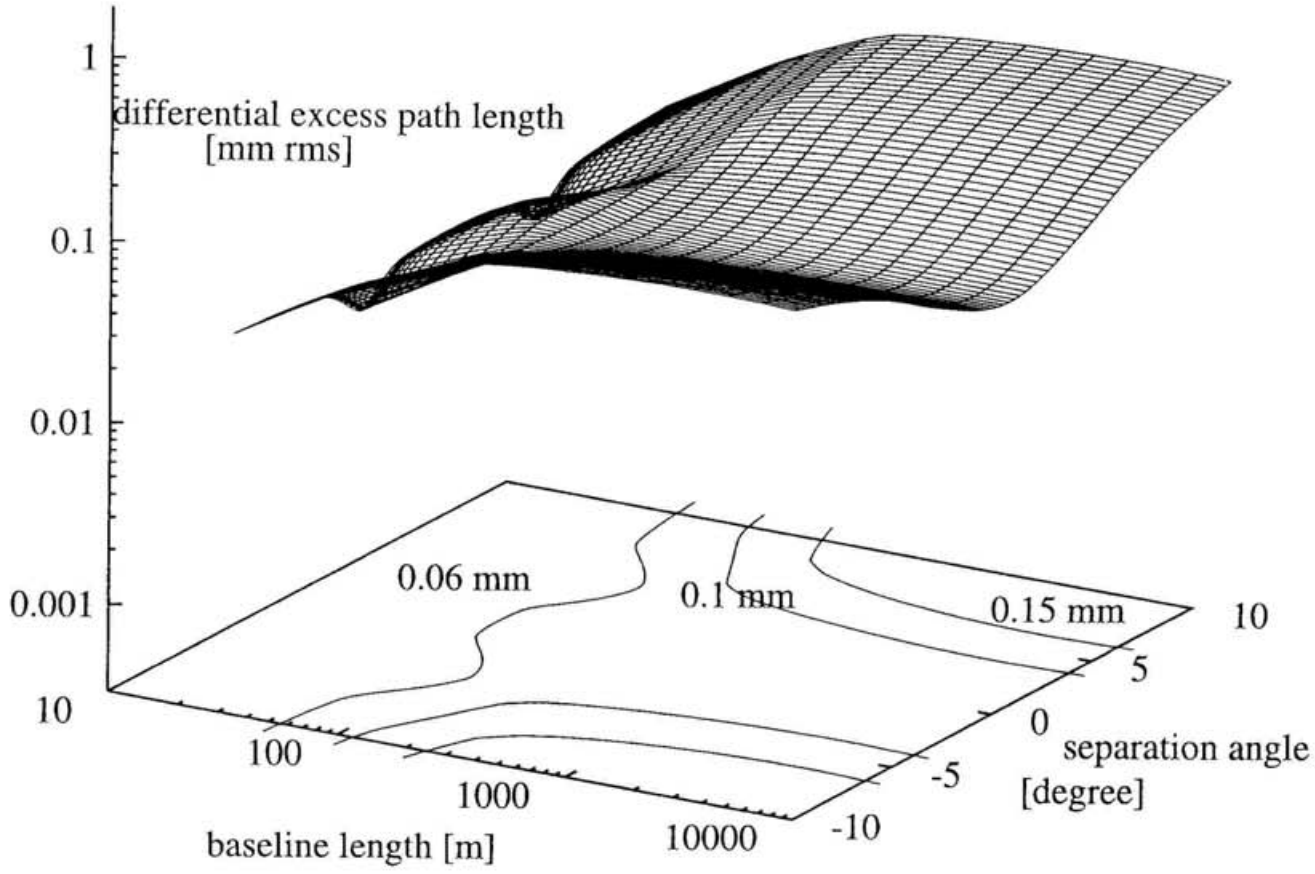

Figure 5.5: Result of the simulation at the potential sites for future millimeter- or submillimeter-wave radio arrays with the antenna-switching method. The switching cycle time is set to 20 s. Each of the contour levels on the base represents the degree of phase compensation of 0.06, 0.1, and 0.15 mm rms in excess path length.

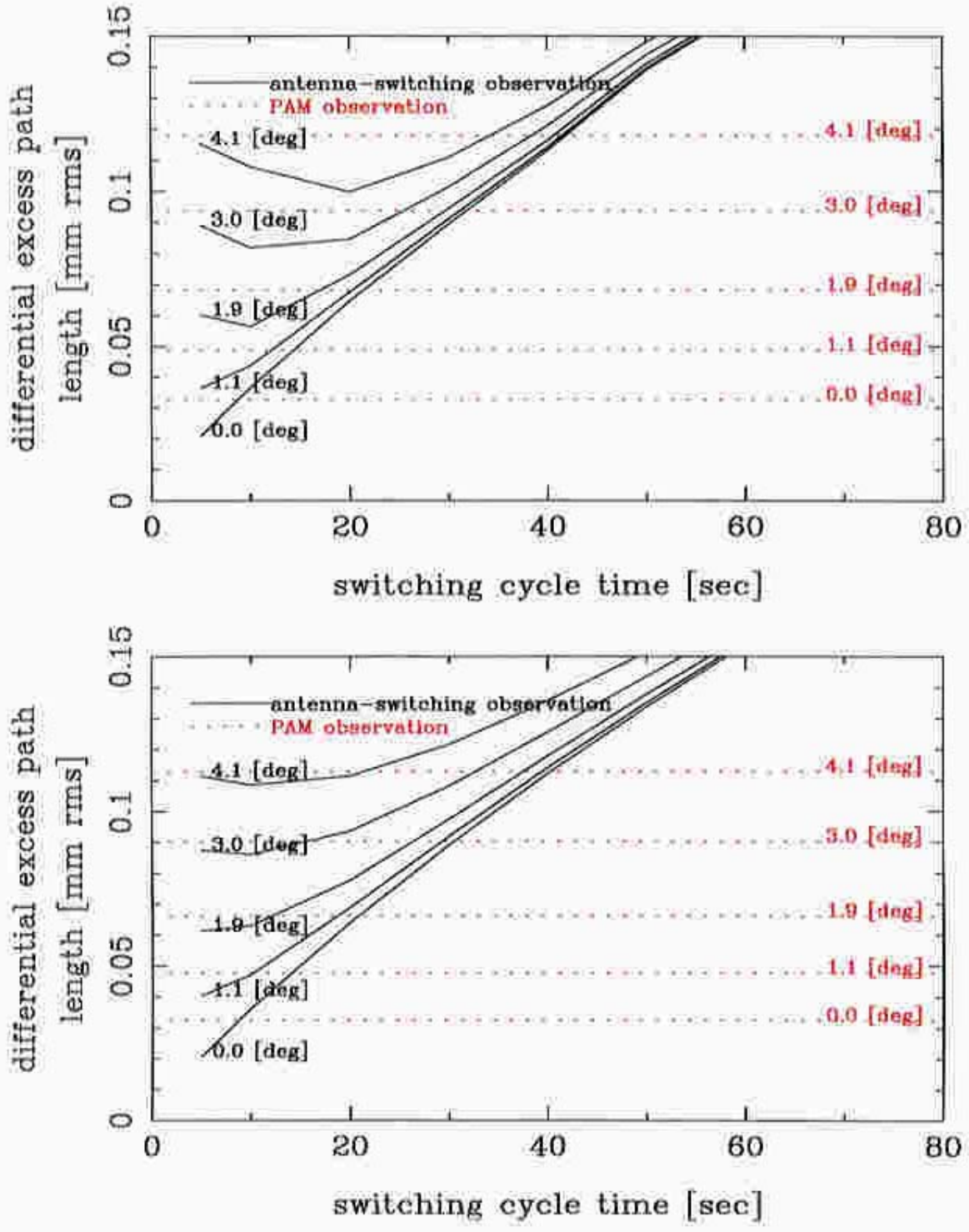

Figure 5.6: Degree of phase compensation with the antenna-switching method as a function of the switching cycle time for the condition discussed in §5.2 (solid lines), and with the PAM in which the array configuration discussed in §4.3.3 but the direction between the close antennas is normal to the baseline (dashed lines), for various angular separation and baseline length of 1000 m. Top drawing is calculated under the condition that the direction of the wind aloft is parallel to the baseline while bottom for the wind direction normal to the baseline.

6 Conclusions

In the present thesis, the compensation of the interferometer phase with the Paired Antennas Method (PAM) has been investigated by means of the special experiments using the NMA and the NRSM. It was explicitly demonstrated in the experiments that the PAM is very successful when the separation angle between the target and reference sources is smaller than a few degrees. Indeed, the degree of the correction reached the rms level of 0.1 mm or higher in excess path length in the PAM2 experiments under the good weather condition. These results indicate that the PAM will be a promising phase compensation method for future large submillimeter-wave arrays to be constructed at the dry high-altitude sites.

The present thesis clarified not only the technical approach to the effective phase compensation, but also the appropriateness of the upper tropospheric model constructed with the hypotheses of the Kolmogorov turbulence, frozen flow, and phase screen. This makes us to understand the mechanism of the phase compensation in terms of the PAM or similar methods. In particular, several characteristic features observed in the experiments, like the angular-separation dependence of the degree of phase compensation, the remarkably linear relationship between the angular separation and the time lag maximizing the coherence factor of the two fringe phase time series, and the existence of the critical angular separation for the effective operation of the PAM, are well interpreted by the above model.

Using the atmospheric structure model, I developed a statistical model for estimating the the residual atmospheric phase fluctuations left in the PAM. The computer simulations based on the statistical model showed good agreement with the results of the experiments within the critical separation angle. This indicates that the statistical model is good enough to use for general assessment of the effectiveness of the PAM in the future radio interferometric arrays, given the suitable SSF parameters at their sites. The simulation for the submillimeter-wave radio arrays at the best sites in the world showed that the phase compensation to the level of 0.06 mm rms in excess path length is attainable in terms of the PAM, provided that a reference calibrator is found within 2° from a target source.

The separation-angle dependence of the antenna-switching method is investigated from the demonstrated data series, whose switching cycle period is 40 s to be produced from the PAM2 data. The analyses showed that the 40-s antenna-switching method is inferior to the PAM, which requires the shorter switching cycle period for the appropriate phase compensation even under good weather conditions. Using the statistical model developed in the present thesis, I also investigated the relation between the degree of phase compensation and the switching cycle time and compared the residual atmospheric phase fluctuations in the antenna-switching method with those in the PAM. The computer simulations showed that the antenna-switching method is achievable in the phase-compensation to

the rms level of 0.06 mm if radio telescope antennas are able to slew fast enough, such as the switching cycle time is less than 10 s for paired sources with the separation angle within 2°. In this investigation it was thus confirmed that the fast antenna-switching method is an effective way to realize the precise phase compensation with the simpler system than the PAM's. It is also noted that the PAM has an important merit in the long time integration to obtain the higher signal-to-noise ratio while observing weak radio sources by means of the continuous observations of each source.

It is very important for the PAM or similar phase-referencing observations that a bright enough calibrator is found in the vicinity of a target source. In other words, the number density of the reference calibrators per steradian is a key issue for the successful phase-referencing observations. This point is especially important for the millimeter- or submillimeter-wave observations since it is generally believed that the number of bright quasars, the reference candidates, decreases as the observing frequency increases.

Holdaway et al. [1994] carried out a survey of calibrator candidates at 90 GHz for millimeter-wave phase-referencing, and *Foster* [1994] showed in his Monte Carlo simulations based on the above survey that there would be a reference source with flux density of at least 0.1×10^{-26} $Wm^{-2}Hz^{-1}$ at millimeter-wave within 2° of an arbitrary point of the sky.

Though the report is encouraging, we may still have a serious difficulty at the submillimeter-wave range since the brightness of the quasar cores reaches the highest value at millimeter or the longer wavelength and decreases rapidly with increasing frequency.

The present thesis proposes a useful solution to the problem, that is, to observe the reference sources at lower frequency in the millimeter- or centimeter-wave range, where the larger number of bright quasars are expected. This multi-frequency phase calibration technique with observing frequencies of 146.81 GHz and 19.45 GHz was examined in the PAM2 experiments and came out very successful. Although the success was in a sense predictable because the refractivity of the water vapor is highly non-dispersive in the radio wave, the present thesis experimentally proved for the first time that the phase compensation in this way is really effective at least below $\cong$150 GHz.

Acknowledgements.

I am deeply indebted to all staffs and students of Mizusawa Astrogeodynamics Observatory, Nobeyama Radio Observatory, and those who belong to the Japanese VLBI group who made it possible to advance my study. I express special thanks to Professor R.Kawabe (National Astronomical Observatory, Japan (NAO)), Professor K-I.Morita (NAO), Professor M.Ishiguro (NAO), Dr.K-M.Shibata (NAO), Mr.M.Saito (University of Tokyo), Mr.K.Kono (University of Tokyo), Mr.H.Imai (University of Tohoku), Mr.T.Jike (The Graduated University for Advanced Studies), Mr.T.Takahashi (NAO), Mr.D-K.Roh (University of Tokyo), Mr.T.Matsushita (University of Tohoku) for valuable discussions and helps in setting up the instruments for the various experiments. I express my hearty gratitude to Professor T.Sasao (NAO) and Professor N.Kawano (NAO) for continuous encouragements and helpful suggestions and discussions.

References

Armstrong,J.W., and R.A.Sramek, Observations of tropospheric phase scintillations at 5GHz on vertical paths, *Radio Sci., 17*, 1579-1586, 1982.

Asaki,Y., M.Saito, R.Kawabe, K-I.Morita, and T.Sasao, Phase compensation experiments with the paired antennas method, *Radio Sci., 31*, 1615-1625, 1996.

Bartel,N., T.A.Herring, M.I.Ratner, I.I.Shapiro, and E.Corey, VLBI limits on the proper motion of the 'core' of the superluminal quasar 3C345, *NATURE, 319*, 733-738, 1986.

Beasley,A., and J.Conway, VLBI Phase-Referencing, in *Very Long Baseline Interferometry and the VLBA, ASP conference series, 82*, 327-343, 1995.

Bremer,M., S.Guilloteau, and R.Lucas, Phase correction with the dual frequency receivers, *IRAM Newsletter, 21*, 5-6, 1995.

Bremer,M., The phase project: observations on quasars, *IRAM Working Report, N°238*, Nov 22, 1995.

Chikada,Y., M.Ishiguro, H.Hirabayashi, M.Morimoto, K-I.Morita, T.Kanzawa, H.Iwashita, K.Nakazima, S-I.Ishikawa, T.Takahashi, K.Handa, T.Kasuga, S.Okumura, T.Miyazawa, T.Nakazuru, K-I.Miura, and S.Nagasawa, A 6 × 320-MHz 1024-channel FFT cross-spectrum analyzer for radio astronomy, *Proc.IEEE,75*, 1203-1210, 1987.

Counselman,III,C.C., S.M.Kent, C.A.Knight, I.I.Shapiro, T.A.Clark, H.F.Hinteregger, A.E.E.Rogers, and A.R.Whitney, Solar gravitational deflection of radio waves measured by very-long-baseline interferometry, *Phy.Rev.Lett., 33*, 1621-1623, 1974.

Dickey,J.O., Atmospheric excitation of the Earth's rotation: progress and prospects via space geodesy, *Contributions of Space Geodesy to Geodynamics: Earth Dynamics*, American Geophysical Union, Washington,D.C.,55-70, 1993.

Dravskikh,A.F., and A.M.Finkelstein, Tropospheric limitations in phase and frequency coordinate measurements in astronomy, *Astrophy.Space Sci., 60*, 251-265, 1979.

Foster,S.M, Distances to MMA calibrators based on 90 GHz source counts, *MMA Memo 124*, 1994.

Guirado,J.C., J.M.Marcaide, P.Elósegui, M.I.Ratner, I.I.Shapiro, A.Eckart, A.Quirrenbach, C.J.Schalinski, and A.Witzel, VLBI differential astrometry of the radio sources 1928+738 and 2007+777 at 5 GHz, *Astron.Astrophys., 293*, 613-625, 1995.

Gwinn,C.R., J.H.Taylor, J.M.Weisberg, and L.A.Rawley, Measurement of pulsar parallaxes by VLBI, *Astron.J., 91*, 338-342, 1986.

Holdaway,M.A., F.N.Owen, and M.P.Rupen, Source counts at 90 GHz, *MMA Memo 123*, 1994.

Holdaway,M.A., and F.N.Owen, A test of fast switching phase calibration with the VLA at 22 GHz, *MMA Memo 126*, 1995.

Imai,H., T.Sasao, O.Kameya, M.Miyoshi, K.M.Shibata, Y.Asaki, T.Omodaka, M.Morimoto, N.Mochizuki, T.Suzuyama, S.Iguchi, S.Kameno, T.Jike, K.Iwadate, S.Sakai, T.Miyaji, N.Kawaguchi, and K.Miyazawa, Detection of compact water maser spots around late-type stars, *Astron.Astrophys., 317*, L67-L70, 1997.

Ishiguro,M., T.Kanzawa, and T.Kasuga, Monitoring of atmospheric phase fluctuations using geostationary satellite signals, in *Proceedings of URSI/IAU Symposium on Radio Astronomical Seeing, held in Beijing, China*, 60-63, 1990.

Lara,L., J.M.Marcaide, A.Alberdi, and J.C.Guirado, VLBI differential astrometry at large angular separation: 3C395–3C382, *Astron.Astrophys., 314*, 672-678, 1996.

Lestrade,J.-F., A.E.E.Rogers, A.R.Whitney, A.E.Niell, R.B.Phillips, and R.Preston, Phase-referenced VLBI observations of weak radio sources. Milliarcsecond position of Algol, *Astron.J., 99*, 1663-1673, 1990.

Linfield,R.P., S.J.Keihm, L.P.Teitelbaum, S.J.Walter, M.J.Mahoney, R.N.Treuhaft, and L.J.Skjerve, A test of water vapor radiometer-based troposphere calibration using very long baseline interferometry observations on a 21-km baseline, *Radio Sci., 31*, 129-146, 1996.

Marcaide,J.M., and I.I.Shapiro, High precision astrometry via very-long-baseline radio interferometry: estimate of the angular separation between the quasars 1038+528 A and B, *Astron.J., 88*, 1133-1137, 1983.

Marcaide,J.M., and I.I.Shapiro, VLBI study of 1038+528 A and B: discovery of wave-

length dependence of peak brightness location, *ApJ., 276*, 56-59, 1984.

Marcaide,J.M., I.I.Shapiro, B.E.Corey, W.D.Cotton, M.V.Gorenstein, A.E.E.Rogers, J.D.Romney, R.E.Schild, L.Bàáth, N.Bartel, N.L.Cohen, T.A.Clark, R.A.Preston, M.I.Ratner, and A.R.Whitney, The quasars 1038+528 A and B, *Astron.Astrophys., 142*, 71-84, 1985.

Marcaide,J.M., P.Elósegui, and I.I.Shapiro, On the relative proper motion of quasars 1038+528 A,B, *Astron.J., 108*, 368-373, 1994.

Masson,C.R., Atmospheric effects and calibrations, in *Astronomy with Millimeter and Submillimeter Wave Interferometry, ASP Conference Series, 59*, 87-95, 1994.

Morita,K.-I., The Nobeyama millimeter array, in *Astronomy with Millimeter and Submillimeter Wave Interferometry, ASP Conference Series, 59*, 18-26, 1994.

Rogers,A.E.E., H.F.Hinteregger, A.R.Whitney, C.C.Counselman, I.I.Shapiro, J.J.Wittels, W.K.Klemperer, W.W.Warnock, T.A.Clark, L.K.Hutton, G.E.Marandino, B.O.Ronnang, O.E.H.Rydbeck, and A.E.Niell, The structure of radio sources 3C 273B and 3C 84 deduced from the "closure" phases and visibility amplitudes observed with three–element interferometers, *ApJ., 193*, 293-301, 1974.

Sasao,T., and M.Morimoto, Antennacluster-antennacluster VLBI for geodesy and astrometry, in *Proceedings of the AGU Chapman Conference on Geodetic VLBI: Monitoring Global Change, NOAA Technical Report NOS 137 NGS 49*, 48-62, 1991.

Shapiro,I.I., J.J.Wittels, C.C.Counselman III, D.S.Robertson, A.R.Whitney, H.F.Hinteregger, C.A.Knight, A.E.E.Rogers, T.A.Clark, L.K.Hutton, and A.E.Niell, Submilliarcsecond astrometry via VLBI. I. relative position of the radio sources 3C 345 and NRAO 512, *Astron.J., 84*, 1459-1469, 1979.

Shibata,K.M., Y.Asaki, I.Asari, Y.Fukuzaki, T.Hara, K.Horiai, K.Iwadate, O.Kameya, N.Kawano, S.Kuji, S.Manabe, S.Sakai, T.Sasao, K.Sato, Y.Tamura, and S.Tsuruta, The Mizusawa 10-m antenna and its VLBI observation system, in *Proceedings of the international symposium on VLBI technology, held at Kyoto international conference hall, Japan*, 185-190, 1994.

Stein,S., Space geodesy and plate motions, *Contributions of Space Geodesy to Geodynamics: Crustal Dynamics*, American Geophysical Union, Washington,D.C.,5-20, 1993.

Stevens,J.A., S.J.Litchfield, E.I.Robson, D.H.Hughes, W.K.Gear, H.Terasranta, E.Valtaoja, and M.Tornikoski, Multifrequency observations of blazars. V. Long-term millimeter, submillimeter, and infrared monitoring, *ApJ., 437*, 91-107, 1994.

Tatarskii,V.I., *Wave Propagation in a Turbulent Medium*, Dover, New York, 1961.

Thompson,A., J.Moran and G.Swenson, *Interferometry and Synthesis in Radio Astronomy*, A wiley-interscience publication, New York, 1986.

Treuhaft,R.N., and G.E.Lanyi, The effect of the dynamic wet troposphere on radio interferometric measurements, *Radio Sci., 22*, 251-265, 1987.

Treuhaft,R.N., and S.T.Lowe, A measurement of planetary relativistic deflection, *Astron.J., 102*, 1879-1888, 1991.

Welch,W.J., The Berkeley-Illinois-Maryland-Association millimeter array, in *Astronomy with Millimeter and Submillimeter Wave Interferometry, ASP Conference Series, 59*, 1-9, 1994.